

Bauhaus-Universität Weimar

Simulation methods for functional and microstructured composite materials

(Simulationsmethoden für funktionalisierte und
mikrostrukturierte Verbundwerkstoffe)

Masterarbeit

zur Erlangung des akademischen Grades
Master of Science (M.Sc.)

an der Fakultät Bauingenieurwesen
der Bauhaus-Universität Weimar

vorgelegt von

Meisam Ansari

Matrikel-Nr. 120146

NHRE / 2020 / 15

Betreuung:

Prof. Dr.-Ing. habil. Carsten Könke

M.Sc. Fabiola Tartaglione

Weimar, 01. September 2020

„Eine neue Art von Denken ist notwendig,
wenn die Menschheit weiterleben will.“

Albert Einstein (1879 – 1955)



Master Thesis

Nr. NHRE / 2020 / 15

Name: ANSARI, Meisam
Matrikel-Nr. 120146

Topic: Simulation methods for functional and
microstructured composite materials

First Examiner Prof. Dr.-Ing. habil. C. Könke

Second Examiner: M. Sc. F. Tartaglione

Start of Work: Mai 01, 2020

End of the Work: September 01, 2020

May 4, 2020



Prof. Dr. Guido Morgenthal
Chairman of examination committee



Aufgabenstellung Masterarbeit

Theme:

Structures made of modern composite materials such as concrete are designed to fulfill multi-purpose requirements with regard to mechanical, thermal and humidity behavior. These different requirements can be either be obtained via specifically designed material mixtures or alternatively via microstructuring of the materials taking advantage of new production methods, such as additive manufacturing. Efficient ways to design these new types of materials are based on numerical simulation methods, especially applying multiscale simulation techniques. The candidate should investigate hierarchical simulation methods which are capable to simulate the macro- and mesoscale behavior for functionalize composite materials. Especially methods to design new types of micro- and mesostructures and corresponding homogenization methods for corresponding constitutive laws on macroscale should be investigated. with regard to future application scenarios in traffic infrastructure the models should be investigated under cyclic or dynamic loading conditions. Criteria for the material behavior are life-time effects as well as damping and structural dynamic response. The master thesis should focus on hierarchical multiscale models, which are coupling scales in a sequential order.

Task description:

1. Literature review on hierarchical multiscale models (theory and simulation) for composite materials, especially concrete under the aspect of microstructure and functionalization. The candidate should investigate recent publications, starting with the given literature references to compile an in-depth literature review.
2. Generic modeling approaches for mesostructured concrete with either commercial FEM programs, such as ANSYS and ABAQUS or ISM software frame, such as mulgrido. The candidate should define micro- and mesostructured situations of cementitious composites which are modeled by FEM models either using commercial FEM packages or the ISM software code (mulgrido). Automatic generation concepts should be developed and investigated, with respect to parameter variation and also automated result evaluation concepts with respect to the stochastic nature of input parameters.
3. Simulation of cyclic and/or dynamic structural response of micro-/mesoscale models. For the generated micro- and mesoscale models cyclic and dynamic loads should be defined and the structural response under these two different loading conditions should be investigated. Fundamental differences in the material response with regard to non-structured cementitious materials should be investigated.
4. Homogenization methods for micro- and mesoscale models for macroscale constitutive models. The candidate should investigate numerical homogenization methods to obtain macroscale constitutive laws. Either theoretical homogenization methods from literature should be described and exemplary applied to the obtained micro- and mesoscale result.
5. Documentation. All models and result should be documented in the written thesis as well as in electronic format with figures and numerical models and attached to the paper thesis on DVD.

Literature:

- a. Stefan Häfner, Grid-based procedure for the mechanical analysis of heterogeneous solids, Ph.D. thesis, Institute of Structural Mechanics, Bauhaus-Universität Weimar, 2007
- b. Stefan Eckardt, Adaptive heterogeneous multiscale models for the nonlinear simulation of concrete, Ph.D. thesis, Institute of Structural Mechanics, Bauhaus-Universität Weimar, 2009
- c. Stefan Häfner, mulgrido code for multiscale material simulations, 2007

Declaration

I hereby declare that I worked on this master thesis independently and used only the specified sources and programs which are referred to.

Weimar, 01. September 2020

Meisam Ansari

Acknowledgment

I would like to express my deepest gratitude to my first supervisor, Prof. Dr.-Ing. habil. Carsten Könke, for introducing me to the topic and defining the scope of this work, for his constructive comments and remarks, for his excellent guideline and recommendations, for his understanding and trust in me.

I would also like to appreciate my second supervisor, M.Sc. Fabiola Tartaglione, for her supportive and informative advice, for her valuable comments, her generous time and availability.

I would also like to thank M.Sc. Christin Zacharias, my colleague at the ISM, for her kind assistance in providing me the remote access to the ISM server and setting up Abaqus.

The time frame of this thesis happened to fall in the difficult period of the broad closure for public health. I observed how this period multiplied the workload of the personnel at the Bauhaus-Universität Weimar and brought them new challenges to overcome. In this regard, I wish to recognize their outstanding endeavor and thank them heartfully.

Abstract

Traditional materials such as steel, wood, and masonry have been known to offer limited strength, durability, and stiffness. The modern construction requires materials that are light, and offer high resistant and durability in a corrosive environment, severe thermal change, and humidity. The application of composite materials in the construction industry aims to meet the demand for enhanced materials. Composite material has in particular a heterogeneous microstructure composed of several phases that are hierarchically organized. The numerical simulation has shown to be an efficient method in the design of a composite. However, the multi-phase microstructure of the composite should be modeled appropriately to be representative of the real material. Multiscale modeling resolves the material heterogeneity into different length scales. A smaller length scale with a higher degree of heterogeneity is adopted for the critical regions in the structure while the rest are modeled on a larger length scale. In this thesis, a generic model for the post-failure behavior of concrete in tension is proposed. A mesoscale model of concrete representing the heterogeneous nature of concrete is formulated. The mesoscale model is composed of three phases: aggregate, mortar matrix, and the Interfacial Transition Zone between them. Material nonlinearity is considered only for the mortar and the ITZ. Both local and non-local formulations of the damage are implemented and the results are compared. Three homogenization schemes from the literature are employed to obtain the homogenized constitutive relationship for the macroscale model. Three groups of numerical examples are provided. For a qualitative study of the developed model, simulation with the unit cell is carried out. For the application to a model with a more complicated structure, the simulation is repeated with the mesoscale model of concrete specimen. To demonstrate the unloading-reloading behavior of the developed model, the cyclic tension test of the unit cell is simulated.

Kurzfassung

Es ist bekannt, dass traditionelle Materialien wie Stahl, Holz und Mauerwerk eine begrenzte Festigkeit, Haltbarkeit und Steifheit bieten. Die modernen Bauwerke erfordern Materialien, die leicht sind und hohe Beständigkeit und Haltbarkeit in einer korrosiven Umgebung, rapiden Temperaturänderungen und Feuchtigkeit bieten. Die Anwendung der Verbundwerkstoffen in der Bauindustrie zielt darauf ab, die Nachfrage nach verbesserten Werkstoffen zu befriedigen. Verbundwerkstoff weist eine heterogene Mikrostruktur auf, welche aus hierarchisch organisierten Phasen besteht. Die numerische Simulationsmethode hat sich als effiziente Methode bei der Entwicklung des Verbundwerkstoffs erwiesen. Die mehrphasige Mikrostruktur des Verbundwerkstoffs benötigt jedoch entsprechende Modellierung, welche das reale Material repräsentieren kann. Die Mehrskalenmodellierung löst die Materialheterogenität in verschiedene Längenskalen auf. Nur die kritischen Bereiche des Bauteiles werden auf einer kleineren Längenskala mit höheren Heterogenitätsgrad aufgelöst, während die ungeschädigte Bereiche auf einer größeren Längenskala abgebildet werden. In dieser Arbeit wird ein generisches Modell für das nichtlineare Materialverhalten des Betons unter Spannung vorgeschlagen. Ein Mesoskalenmodell wird aufgebaut, welches die heterogene Materialstruktur des Betons darstellt. Das Mesoskalenmodell besteht aus drei Phasen: groben Zuschlägen, Mörtelmatrix und Übergangszone zwischen Zuschlag und Matrix. Das nichtlineare Materialverhalten wird nur in den Mörtel und die Übergangszone umgesetzt. Es werden sowohl die lokale als auch die nichtlokale Formulierung des Schädigungsgrades implementiert und die Ergebnisse verglichen. Drei Homogenisierungsmethoden aus der Literatur werden verwendet, um die homogenisierte konstitutive Beziehung für das Makroskalenmodell zu erhalten. Drei Gruppen von numerischen Beispielen werden angeführt. Anhand von der Simulation mit einer Elementarzelle wird die qualitative Untersuchung eingeleitet, welche das in diese Arbeit entwickelte Modell prüft. Die Simulation wird mit dem Mesoskalenmodell des Betons wiederholt, um die Anwendung des entwickelten Modells auf eine komplizierte Mikrostruktur vorzustellen. Um das Entlastungs- und Wiederbelastungsverhalten des entwickelten Modells zu demonstrieren, wird der zyklische Spannungstest mit der Elementarzelle simuliert.

Contents

Declaration	i
Acknowledgment	ii
Abstract	iii
Kurzfassung	iv
List of figures	vii
List of tables	ix
1 Introduction	1
1.1 motivation.....	1
1.2 Aims and scope of the work.....	2
1.3 Outline of the work.....	2
2 Literature Review	4
2.1 Introduction.....	4
2.2 The Scales of Observation.....	5
2.3 Generating a Micromodel.....	8
2.3.1 Take-and-place method.....	9
2.3.2 Divide and fill method.....	11
2.3.3 Random particle drop method.....	13
2.3.4 Stochastic-heuristic algorithm.....	13
2.3.5 The unique method of (Contrafatto, Cuomo, & Gazzo, 2016).....	14
2.4 Multiscale Modeling of Concrete.....	17
2.4.1 Class I: Sequential methods.....	19
2.4.2 Class II: Concurrent methods.....	26
2.4.3 Adaptive Heterogeneous Method by (Eckardt, 2009).....	29
2.4.4 The Macro-Micro Model of HCP by (Nguyen, Stroeven, & Sluys, 2012).....	30
2.4.5 A Macro-Meso model under cyclic load by (Sun, Guo, Guo, Wu, & Wang, 2020).....	32
3 Generic Model for Post-failure Behavior of Concrete	35
3.1 Introduction.....	35
3.2 Local formulation of the damage model.....	37

Problem statement: spurious mesh sensitivity	38
Hillerborg energy approach: a remedy for mesh sensitivity	40
Implementation in Abaqus	42
3.3 Non-local formulation of the damage model.....	46
Implementation in Abaqus	47
3.4 Modeling the ITZ	51
Implementation in Abaqus	53
3.5 Homogenization	56
Averaging over the entire volume.....	56
Averaging over the undamaged volume	56
Averaging over the damaged volume	56
4 Numerical Examples.....	60
4.1 Introduction	60
4.2 Mesoscale unit cell under uniaxial tension.....	63
The first assessment	64
Size effect.....	66
The impact of nonlinear ITZ.....	66
Comparison between the averaging techniques	69
Mesh sensitivity in the local damage model	74
Non-local damage versus local damage.....	75
4.3 Mesoscale cubic specimen under uniaxial tension.....	77
Generating a random distribution of particles.....	77
The mesoscale model	79
Assessment of the result.....	80
Investigation into the observed size sensitivity.....	85
4.4 Mesoscale unit cell under cyclic tension.....	86
5 Conclusions.....	90
References	92

List of figures

Figure 2.1 – Two common types of microstructures.....	9
Figure 2.2 – Two common methods for dividing material space.....	12
Figure 2.3 – Lattice element obtained from Delaunay triangulation by (Grassl & Jirásek, 2010).....	13
Figure 2.4 – Allocation procedure proposed by (Contrafatto, Cuomo, & Gazzo, 2016)	16
Figure 2.5 – Multiscale methods: a) hierarchical, b) concurrent.....	18
Figure 2.6 – <i>FE2</i> method developed by (Feyel, 2003).....	20
Figure 2.7 – Perception of the RVE by (Hashin, 1983)	21
Figure 2.8 – Comparison between the classical and <i>FE2</i> model, illustration by (Feyel, 2003).....	22
Figure 2.9 – Stress-strain curves of different volume fractions by (Gitman, Askes, & Sluys, 2007)	24
Figure 2.10 – a) Original unit cell at scale K, b) Perforated unit cell at scale K.....	25
Figure 2.11 – The active damaged domain Ω_d	26
Figure 2.12 – Zooming technique	27
Figure 2.13 – Multiscale model (b) suggested for the macroscopic model (a)	27
Figure 2.14 – Coupling of macro- and meso-domain, illustration by (Eckardt, 2009)	28
Figure 2.15 – Coupling methods, illustration by (Eckardt, 2009).....	29
Figure 2.16 – 3D micromodel and 2D slice of the HCP	31
Figure 2.17 – Crack transfer between mesoscopic and macroscopic models	34
Figure 3.1 – Progressive failure of bundled fibers in uniaxial tensile stress test (Jirásek, 2004).....	36
Figure 3.2 – Stress-strain diagram with two alternatives for softening branch.....	38
Figure 3.3 – Uniaxial tension test of a bar with material imperfection in the middle	39
Figure 3.4 – Proposed model for an opening crack by (Hillerborg, Modéer, & Peterson, 1976)	41
Figure 3.5 – Strain decomposition of mortar specimen under incremental tensile force	43
Figure 3.6 – Tabular inputs for modelling tensile behavior by the CDP in Abaqus Property module.....	45
Figure 3.7 – Weighted averaging scheme	46
Figure 3.8 – Exporting the output from Report Field Output window in Abaqus Visualization module ...	48
Figure 3.9 – Computation of non-local strain by matrix multiplication.....	49
Figure 3.10 – The cutting procedure for reducing the domain size.....	50
Figure 3.11 – Single-mode constitutive behavior for a cohesive interface	51
Figure 3.12 – Generating an offset layer of mesh in Abaqus Mesh module	53
Figure 3.13 – Modeling Contact Cohesive Behavior in Abaqus Interaction module.....	54
Figure 3.14 – Gap and overclosure between two surfaces in contact.....	55
Figure 3.15 – The contact initialization tool in Abaqus Interaction module	55
Figure 3.16 – The developed algorithm for homogenization	59

Figure 4.1 – The defined damage evolution in the mortar	60
Figure 4.2 – The defined stress-strain behavior of the mortar under uniaxial tension	61
Figure 4.3 – Illustration of the single and combined unit cell	63
Figure 4.4 – Creating strain-driven uniaxial tension test of the unit cell in Abaqus Load module	64
Figure 4.5 – Uniaxial tension test of single unit cell: output vs. input diagrams	65
Figure 4.6 – Uniaxial tension test of single unit cell: stress and damage distribution at mid-section.....	65
Figure 4.7 – Uniaxial tension test of combined unit cells: size effect.....	66
Figure 4.8 – Uniaxial tension test of single unit cell: with and without ITZ.....	67
Figure 4.9 – Uniaxial tension test of horizontally coupled unit cells: with and without ITZ.....	67
Figure 4.10 – Uniaxial tension test of vertically coupled unit cells: with and without ITZ.....	68
Figure 4.11 – Uniaxial tension test of 4 combined unit cells: with and without ITZ.....	68
Figure 4.12 – Comparison between averaging techniques: single unit cell without ITZ	70
Figure 4.13 – Comparison between averaging techniques: horizontally coupled unit cells without ITZ ...	71
Figure 4.14 – Comparison between averaging techniques: vertically coupled unit cells without ITZ	71
Figure 4.15 – Comparison between averaging techniques: 4 combined unit cells without ITZ	72
Figure 4.16 – Comparison between averaging techniques: single unit cell with ITZ	72
Figure 4.17 – Comparison between averaging techniques: horizontally coupled unit cells without ITZ ...	73
Figure 4.18 – Comparison between averaging techniques: vertically coupled unit cells without ITZ	73
Figure 4.19 – Comparison between averaging techniques: 4 combined unit cells without ITZ	74
Figure 4.20 – Uniaxial tension test of single unit cell: reduced mesh sensitivity in local damage model ..	75
Figure 4.21 – Uniaxial tension test of single unit cell: local vs. non-local damage model	76
Figure 4.22 – Generated particles by APG.....	79
Figure 4.23 – Comparison between different volume fractions for every model size	81
Figure 4.24 – Comparison between different model sizes for every volume fraction	82
Figure 4.25 – Simulation outcomes in (Gitman, Askes, & Sluys, 2007)	83
Figure 4.26 – Damage-distribution at 0.1% strain for every specimen (mid-section)	84
Figure 4.27 – Comparison between two model sizes without nonlinear ITZ.....	85
Figure 4.28 – Focal point model by (Yankelevsky, 1989).....	86
Figure 4.29 – Creating displacement-driven cyclic load in Abaqus Load module	87
Figure 4.30 – First simulation of cyclic tension with a single unit cell without ITZ	88
Figure 4.31 – Second simulation of cyclic tension with a single unit cell without ITZ.....	89
Figure 4.32 – Third simulation of cyclic tension with a single unit cell without ITZ.....	89

List of tables

Table 2.1 – Comparison between the observation scales in different studies	7
Table 3.1 – Required input parameters for the CDP in Abaqus	44
Table 3.2 – Assigning name to the output files	48
Table 3.3 – Computation time with and without the cutting procedure	50
Table 3.4 – Assigning name to the output files	58
Table 4.1 – Computation of the inputs for modeling mortar damage with the CDP	61
Table 4.2 – Material properties considered in the present study	62
Table 4.3 – Mechanical properties obtained from stress-strain diagrams	69
Table 4.4 – Variation in mesh size	74
Table 4.5 – Mechanical properties obtained from stress-strain diagram.....	76
Table 4.6 – Variation of the cubic specimens in the simulation.....	77
Table 4.7 – Aggregate set and diameters.....	78
Table 4.8 – Generated particles for cubic specimens	78
Table 4.9 – No. of elements in cubic specimen.....	80
Table 4.10 – Mechanical properties obtained from stress-strain diagram.....	81

1 Introduction

1.1 motivation

The abiding interest in going beyond the limits of building structures has been the motive for constructing taller, longer, or lighter structures. The growing number of tall buildings, long bridges, and light shells is the result of that interest. On the one hand, engineers face the challenge of designing these massive structures for immensely larger loads. On the other hand, they struggle to develop construction materials that can withstand greater loads or harsher environmental conditions faced by these buildings.

Traditional materials such as steel, wood, and masonry have been known to offer limited strength, durability, and stiffness. The modern construction requires materials that are light and high resistant. High durability in a corrosive environment, severe thermal change, and humidity are increasingly expected by today's standard. The application of composite materials in the construction industry aims to meet the demand for enhanced materials. Composite engineering has therefore become the imperative field of study and research among civil engineers.

Material design requires not only laboratory experiments, but also numerical simulations. Although experimenting with materials in a research laboratory is a well-known method for observing the material behavior in a real test setup, the real experiments are usually costly, time-consuming, and labor-demanding. In contrast, numerical simulations can be repeated numerous times with lower cost and effort. They produce no material waste, and they almost eliminate the danger of physical harm that might occur during a real experiment. Therefore, computational engineering and numerical simulation have been a growing trend in the field of composite material.

One drawback of numerical simulation is that their result needs to be verified and evaluated by real experimental data. This is usually done by comparing the simulation output with the experimental result. To obtain a successful result, the model of the material requires to be representative of the real material. Composite material has in particular a heterogeneous microstructure composed of several phases that are hierarchically organized. Numerical simulation of a composite is known to result in a realistic output only if the multi-phase microstructure of the composite is modeled appropriately. Modeling such a heterogeneous structure is a great challenge in the design of a composite.

Multiscale modeling resolves the material heterogeneity into different length scales. The microstructure of a composite is represented on different length scales with various degrees of heterogeneity. A smaller length scale is adopted for the critical regions in the structure while the rest are modeled on a larger length scale. This way, the numerical efficiency of the larger length scale is combined with the accuracy of the smaller length scale to optimize the simulation procedure for the computation time and power.

1.2 Aims and scope of the work

The main focus of this thesis is on hierarchical multiscale models of composite materials in particular concrete. Within this context, the following four objectives are to be met.

Firstly, an intensive literature review of hierarchical multiscale models is to be conducted. The principles and aspects of multiscale models should be studied. The recent publications in this field are to be reviewed and the latest achievements should be reported.

Secondly, a generic model of the cementitious composite, in particular concrete, is to be developed. The model should represent the heterogeneous microstructure of the composite. In this respect, the fracture theory and damage models for concrete must be studied. Among the commercial FEM programs, Abaqus may be used as a platform for modeling and solving the FEM problem. Automatic generation procedures should be developed and investigated, concerning the stochastic nature of the input, parameter variation, and result evaluation.

Thirdly, simulation of tests under monotonic and cyclic loads should be carried out and the response of the developed model should be investigated. Furthermore, the material response to these two loading scenarios is to be compared and discussed. Fundamental differences in the material response concerning non-structured cementitious materials should be investigated.

Lastly, numerical homogenization schemes for obtaining macroscale constitutive relationships are to be investigated. The available methods in the literature should be described. A comparative study of the obtained result should be conducted and reported.

The present study is an initiative for an extensive study on the functionalization of composite materials in transport infrastructure. The enhanced functionality should meet the criteria for life-time effects, structural damping, and dynamic response.

1.3 Outline of the work

Chapter 2 provides an in-depth review of the available heterogeneous models for concrete as found in the literature. The concept of observation scales is introduced and the most common scale lengths are compared. The various classical methods for generating a micromodel are described and the most recent improvement in their procedures is reported. Different multiscale modeling approaches are explained and examples of developed models are provided as reported in the literature.

Chapter 3 proposes a generic model for the post-failure behavior of concrete in tension. A mesoscale model of concrete representing the heterogeneous nature of the material is formulated. The mesoscale model is composed of three phases: aggregate, mortar matrix, and the ITZ. Material nonlinearity is considered only for the mortar and the ITZ. For a comparative study, both local and non-local formulations of the damage are implemented in the mortar domain. Modeling the ITZ in Abaqus with traction-separation law for

damage initiation and evolution is described. Three available homogenization schemes from the literature are programmed in Octave.

Chapter 4 provides numerical examples of the developed model to demonstrate its application and to investigate its capabilities and weaknesses. The mechanical properties used in the simulation are collected from the literature. The numerical examples are classified into three groups. (i) The simulation with the unit cell is conducted for a qualitative study of the damage model, the material inputs, and the overall formulations. (ii) The simulation is then extended to the mesoscale model of concrete specimens to evaluate the outcome of the developed procedures when applied to a model with a more complicated structure than the unit cell. By using the take-and-place method and with the help of two open-source codes, the aggregate particles are generated in Octave and imported in Abaqus. (iii) The cyclic tension test of the unit cell is simulated to demonstrate the unloading-reloading behavior of the developed model. A simple impulse and a cyclic load are used in the simulation.

Chapter 5 summarizes the main conclusions of this thesis. Furthermore, the observed imperfections in the proposed model are highlighted as the objectives for future studies.

2 Literature Review

2.1 Introduction

The first form of the composite material was perhaps straw and mud combined to form bricks for building construction by Egyptians (Emery, 2009). Composite material or shortened composite is a material made from two or more constituents with different material properties (physical, chemical, or mechanical). The constituents are combined to produce a material with different characteristics from the individual components. The main goal is to produce material with improved or desired properties.

The industrial era led the English cement manufacturer Joseph Aspdin to development of a method for production of Portland cement in 1824 (Herring, 2002). Reinforced concrete, in the form used today, is known to be invented in 1849 by Joseph Monier (Bellis, 2019). Some years later in 1853, Francois Coignet built the first steel-reinforced concrete house in the suburbs of Paris (Patowary, 2019). Nevertheless, the use of concrete as a construction material with different compositions goes back to centuries before the industrial era (Herring, 2002).

Along with the development of the concrete industry, the technical understanding of concrete behavior and its mechanical properties improved too. Consequently, engineers observed the necessity of taking the heterogeneous structure of concrete into account [(Schutter & Taerwe, 1993), (Bazant, Tabbara, Kazemi, & Cabot, 1990)]. Homogeneity and heterogeneity are terms frequently used in material science to describe the degree of uniformity in a substance or organism. While a homogeneous material is considered to be fairly uniform in composition, mechanical or physical properties, a heterogeneous material is distinctly nonuniform in one or more of these qualities. Concrete is a mixture of several components, and it is formed by a chemical reaction between them known as hydration. The hydration does not turn the components into one homogeneous substance; therefore, concrete is considered to be heterogeneous (Nguyen, Stroeven, & Sluys, 2012).

The main components (or constituents) of concrete are mostly the coarse aggregate, such as gravel, the fine aggregate, such as sand, and the cementitious paste made by mixing water and cement. Concrete is produced by mixing these components following a prescribed “mix-design” that describes the required portion of each component to achieve a desired characteristic or quality. However, in the design of concrete structures, one may assume that the concrete mixture is a relatively uniform material with effective mechanical properties determined through laboratory experiments; this assumption is commonly made today in the design codes for reinforced concrete structures. Nonetheless, when it comes to the formation and propagation of cracks, fractures, or nonlinear behavior of concrete, the assumed effective properties may

lose their accuracy, and simulation of the components of concrete may become necessary to predict the response of the structure (Verhoosel, Remmers, M.A., & de Borst, 2010).

The heterogeneous model of concrete has been the focus of research and studies over the past decades. Various modeling scales have been defined, on which one or more constituents are modeled with distinct material properties and the rest are simulated as homogeneous components with effective properties. In other words, the modeling scales are similar to the zoom level of a camera. As the camera zooms in on the material, a greater number of distinct constituents are observed.

In the following sections, the common observation scales for the heterogeneous model of concrete are presented, as found in the literature. Then, various available methods for generating a model on these scales are described and compared to demonstrate their complexity, advantages, and drawbacks. Finally, multiscale modeling is explained as an approach to consider the heterogeneity of concrete in a structural element of a common form.

2.2 The Scales of Observation

The main constituents of concrete are the aggregate (coarse to fine) and the cementitious paste (the mixture of cement particles and water). These constituents are hierarchically organized in the material structure. On the length scale of a few centimeters, the embedded aggregates in the cement paste are visible to the naked eyes. On the smaller length scale of a few millimeters, the clinker grains inside the dense cementitious paste are distinguishable. The aided eyes can observe the hydrates on the length scale of a few micrometers (Göbel, 2018).

The heterogeneous model of concrete represents the main constituents of the mixture. The scale of observation defines the extent to which the heterogeneity of the material, i.e. the number of distinct constituents, is considered in the material model. At the highest level of observation, no inhomogeneities are considered and the effective material properties are determined to be the representative of the concrete-mix as a homogeneous body; as if the mixture was composed of only one constituent. (Cusatis, Bazant, & Cedolin, 2006) describe this level as the “usual engineering scale” for the design of structural elements, i.e. beams, columns, slabs. This level is mostly referred to as “Macrolevel or Macroscale” (both terms can be used interchangeably). For example, EN 1992-1-1 recognizes the compressive strength of concrete through the compression test of a cylindrical specimen of the concrete-mix, prepared and tested following the requirements in EN 206-1. This means, that the characteristic strength of the cylindrical specimen is considered to be the representative of any points in the structural element and to be uniform all over its volume.

One of the earliest attempts to identify the observation scales goes back to (Zaitsev & Wittman, 1981). They specified four characteristic levels in descending order: Macrolevel, Mesolevel, Microlevel, and Nanolevel. Two main differences between these levels are in the number of distinctive inclusions that are

modeled, and in the linear dimension of the Representative Volume Element (RVE)¹. At the macrolevel, a typical dimension of the RVE is assumed to be of a magnitude of 100 mm. At the second level of observation, the mesolevel, the aggregate and the mortar volume are considered as two constituents in the model. Hence, concrete is regarded as a two-phase material. The typical dimension of the RVE is known to be of a magnitude of 10 mm. However, it is also common to consider an Interfacial Transition Zone (ITZ) at mesolevel, which is surrounding the coarse aggregate (Cusatis, Bazant, & Cedolin, 2006). In this sense, the material at the mesoscale can also be considered as a three-phase material. Nevertheless, the ITZ occupies a very small volume fraction of the model and its thickness may be considered to be zero (as presented in section 2.4.3).

At the third level of observation, the microlevel, (Zaitsev & Wittman, 1981) consider the mortar volume to be composed of the Hardened Cement Paste (HCP) and the big pores with a maximum diameter of 0.1 mm. The typical linear dimension of the RVE at this level is assumed to be approximately 0.5 mm. For example, (Nguyen, Stroeven, & Sluys, 2012) consider the HCP at the microlevel to be composed of the calcium silicate hydrates (CSH) and the Portlandite (CH) together with the pores (their model will be reviewed in section 2.4.4). At the fourth level in this classification, the nanolevel is introduced, which includes fine or so-called capillary pores² in the hardened cement paste. The typical dimension of the little pores and the RVE at this level are assumed to be of a magnitude of 10^{-4} mm and 5×10^{-4} mm, respectively.

In addition to the number of distinctive inclusions and the RVE size, consideration of the type of material failure varies from one scale to the other too. For example, (Zaitsev & Wittman, 1981) specify that the probability of shrinkage cracks is very small at the mesolevel and they are not taken into account. The above 4 levels are widely recognized and referred to by the researchers in the field of composite materials, i.e. (Eckardt, 2009), (Nguyen, Stroeven, & Sluys, 2012). Nevertheless, the observation scales are not limited to these 4 well-known levels. (Cusatis, Bazant, & Cedolin, 2006) distinguish two other scales besides: the atomistic scale and the mini-scale. The atomistic scale is one level lower than the nanolevel. It is characterized by the structure of the micro-crystalline particles in the hydrated Portland cement. The mini-scale is between the meso- and the microlevel. The fine aggregate, with dimensions from 0.1 to about 3 mm, is also considered as distinctive materials³ at the mini-scale, and the HCP is composed of two constituents: the bulk paste and the ITZ. The bulk paste is assumed to have the lower porosity and the higher stiffness and the ITZ to be the opposite.

(Zhang, 2013) also names six different scales from the macro- to the nanoscale. Comparing with the 6-level scale in (Cusatis, Bazant, & Cedolin, 2006), the main difference is the chosen name for the two lowest levels: the “sub-microscale” instead of the nanoscale at the fifth level and the “nanoscale” instead of the

¹ RVE is the smallest element, representing the material structure, considered in the numerical simulation. This will be discussed later in detail.

² Capillary pores are a network of very small channels and holes resulted by concrete de-watering during the hardening.

³ Fine aggregate is considered to be part of the mortar at mesoscale in contrast to mini-scale

atomistic scale at the sixth level. (Zhang, 2013) also provides the typical RVE dimension for all levels in contrast to (Cusatis, Bazant, & Cedolin, 2006). Table 2.1 summarizes the observation levels.

Table 2.1 – Comparison between the observation scales in different studies

Observation scale			Inclusions as distinct constituents				RVE typical size [mm]				
Z.W. 1981	C.B.C 2006	Z. 2013	Aggregate		Cementitious paste (Mortar)		Z.W. 1981	Z. 2013			
Macro-			Concrete is homogeneous				100				
Meso-			Coarse		Cementitious paste + fine aggregate		10				
-	Mini-	Meso-	Coarse	Fine	Bulk Cementitious paste		-	1			
Micro-			Coarse		ITZ	Big pores		0.5	0.1		
Nano-		Sub-micro-				CSH	CH	Big pores	Little pores	5×10^{-4}	10^{-4}
-	atomistic	Nano-				Micro-crystalline particles of hydrated Portland cement with all pores				-	10^{-6}

Z.W.1981: (Zaitsev & Wittman, 1981)

C.B.C.2006: (Cusatis, Bazant, & Cedolin, 2006)

Z.2013: (Zhang, 2013)

As shown in Table 2.1, the cementitious paste is composed of distinct phases. There are several models for a realistic representation of the cement paste. (Göbel, 2018) indicates the first three types of models developed for estimating the stiffness properties of cement paste:

- The Bernard model consists of five phases: (i) CSH gel, (ii) CH, (iii) unhydrated clinker grains, (iv) aluminate, and (v) capillary pores (Bernard, Ulm, & Lemarchand, 2004).
- The Constantinides model with four phases: (i) CSH gel, (ii) CH, (iii) unhydrated cement particles, and (iv) pores (Constantinides & Ulm, 2004).
- The Sanahuja model composed of (i) CSH gel, (ii) unhydrated clinker, and (iii) pores (Sanahuja, Dormieux, & Chanvillard, 2007).

The particle size that defines the boundary between the aggregate and the mortar phase is not identical in different studies. (Göbel, 2018) considers the particles smaller than 2 mm to be in the mortar phase. (Ruan, Li, Jin, Pan, & Yin, 2019) and (Tasdemir & Karihaloo, 2001) regard particle smaller than 5 mm as fine aggregate. (Nguyen, Stroeven, & Sluys, 2012) create a microscale model of mortar composed of cement particles alone with particles smaller than 0.04 mm. Including fine aggregate in the mortar phase affects the mechanical properties of the mortar. This is an extensive topic that is considered to be out of the scope of the present study.

It is noteworthy to remark on the two terms that are widely used in the literature: the “micromodel” and the “microscale”. The “micromodel” is a general term that refers to a heterogeneous model composed of

distinct constituents. A “micromodel” could be created at any of the six scales discussed in the above. The term is usually used to distinguish between homogeneous and heterogeneous models. On the other hand, the “microscale” denotes in particular that the heterogeneous model is created at the microscale. Since both terms use the prefix “micro-“, close attention to the context is necessary to avoid misunderstanding.

2.3 Generating a Micromodel

It is crucially important to generate a micromodel that can appropriately describe the internal structure of the composite material. The proper modeling takes into account both the physical geometry of the inclusions (shape and size of the particles) and the spatial distribution of the inclusions (spacing between them, or how they scatter over the volume of the material).

One way to achieve accuracy in the modeling is to use a microscopic photo of the material. For example, (Hain & Wriggers, 2008) used three-dimensional CT-scanning (Computerized Tomography) of the hardened cement paste. CT-scanning of several specimens with an edge length of 1.75 mm and a resolution of 0.001 mm were conducted in Berlin by the Federal Institute for Material Research and Testing (*Bundesanstalt für Materialforschung und -prüfung, in German*). Each CT-scan is composed of numerous data points that are called Volume Pixel or in short “Voxel”. The CT-scans are then processed through which the scanning noises are filtered out, and hydration products, non-hydrated residuals, and pores are distinguished.

In another approach, the micromodel can be artificially generated. In such a method, dimensions of the particles usually follow a prescribed “grading curve” and the geometry of the specimen is created by a random distribution of the particles. This can be achieved by several methods that will be reviewed in this section to illustrate how an artificial micromodel is generated. Firstly, it is necessary to recall and understand two common types of microstructures in composite materials: (i) Periodic microstructure, (ii) Random microstructure.

Periodic microstructures are frequently found in composite materials such as carbon fibers and honeycomb structures. They can be represented by only one unit-cell that is repeated uniformly in all directions (Figure 2.1.a). This unit-cell is sometimes called the Representative Unit-Cell (RUC). A microstructure that can be defined by the periodic distribution of an RUC may be referred to as a periodic microstructure. For example, in 2D modeling, all particles are assumed to have a uniform geometrical shape such as a circle or a regular polygon. The unit-cell is then composed of one or more particles surrounded by the mortar [(Michel, Moulinec, & Suquet, 1999), (Gitman, Askes, & Sluys, 2007)].

On the other hand, a “random microstructure” is too complicated to be represented by such a simple RUC because its structure is not formed by a repeated shape or pattern (Figure 2.1.b). For example, in concrete, the size of the aggregate particles and their spatial distribution are not uniform over the volume. Generating an RUC for a random microstructure that represents the randomness in particle size and their spatial distribution is quite challenging [(Contrafatto, Cuomo, & Gazzo, 2016), (Schutter & Taerwe, 1993)]. The

following methods are some of the most common numerical techniques to generate a random microstructure.

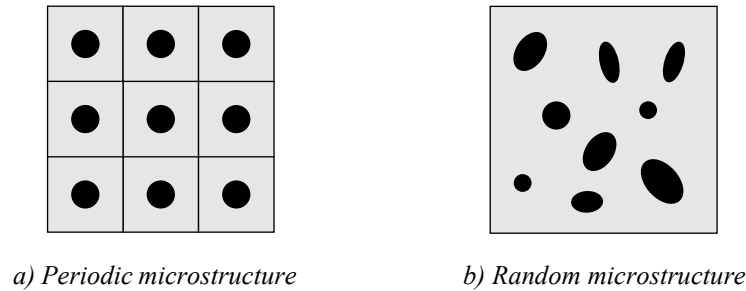


Figure 2.1 – Two common types of microstructures

2.3.1 Take-and-place method

(Cundall, 1971) proposed a method for generating particles in simulation program. (Bazant, Tabbara, Kazemi, & Cabot, 1990) later modified and improved Cundall's method, and it is known today as the take-and-place method. The title of the method is self-explanatory and the procedure follows a rather simple algorithm. Particles of different sizes are generated and placed one by one in a position that is randomly chosen from the volume of the specimen. By every placement, the particle is checked for overlap with the existing particles. The step-by-step procedure can be summarized as follows:

Step 1) The shape of the particles is determined and idealized. Two common shapes are circle and ellipsoid. (Bazant, Tabbara, Kazemi, & Cabot, 1990) choose a simple circular shape and consider the radius of the circle, r_i as the input variable for creating different sizes. (Häfner, Eckardt, Luther, & Könke, 2006) idealize the particles with ellipsoid whose surface is given by Equation (2.1), with three radii r_1 , r_2 , and r_3 , each representing the radius in one cartesian direction. They express r_1 and r_3 as a function of r_2 with Equations (2.2) and (2.3), to reduce the input variables from three radii to only one radius.

$$\left(\frac{x}{r_1}\right)^2 + \left(\frac{y}{r_2}\right)^2 + \left(\frac{z}{r_3}\right)^2 = 1 \quad r_1 \geq r_2 \geq r_3 \quad (2.1)$$

$$r_1 = \left(1 + X_2 \frac{\eta_{13} - 1}{\eta_{13} + 1}\right) r_2 \quad (2.2)$$

$$r_3 = \left(1 + X_3 \frac{\eta_{13} - 1}{\eta_{13} + 1}\right) r_2 \quad (2.3)$$

X_1 and X_2 are uniformly distributed random numbers between 0 and 1, and η_{13} is the maximum ratio between the radii r_1 and r_3 that controls the shape of the particle. Further details are provided in (Häfner, Eckardt, Luther, & Könke, 2006). As can be seen, assuming ellipsoidal shape for the particles brings some additional computation into the process.

Step 2) The volume ratio for each particle size is determined by the grading curve that is prescribed for the concrete mix-design. The Fuller ideal grading curve is frequently used for this purpose, and it is defined by Equation (2.4).

$$p_i = 100 \left(\frac{d_i}{D_{max}} \right)^{0.45} \quad (2.4)$$

In the above, p_i is the percentage of particles passing the i^{th} sieve, d_i is the opening size of the sieve, and D_{max} is the maximum particle size. The concrete mix-design also specifies the water-cement ratio, from which the total volume of the aggregate can be obtained.

$$V_{aggr} = V_{total} - V_{water} - V_{cement} - V_{air} \quad (2.5)$$

The volume ratio of each particle size can be then computed by multiplication of p_i and V_{aggr} .

Step 3) Starting with the largest size, the particles are generated one by one until the desired volume is achieved.

Step 4) The placement procedure is initiated. (Bazant, Tabbara, Kazemi, & Cabot, 1990) specify that a random number generator can be used to generate the coordinates of the particle centers in 3D space of the specimen volume. Following a similar random number generator, (Eckardt, 2009) recommends starting the placement procedure with the largest particle size.

The particles are checked for overlap as they are placed. When an overlap is detected, the generated coordinate at the previous step will be rejected and a new coordinate for the center of the particle is produced. As (Bazant, Tabbara, Kazemi, & Cabot, 1990) describe, each particle should be checked for the overlap with the previously placed particles. As more particles are placed in the volume, the procedure becomes slower because the number of particles that need to be checked for the overlap with the new particle increases progressively. This is one of the drawbacks of the take-and-place method. However, (Häfner, Eckardt, Luther, & Könke, 2006) propose a technique that reduces the required time for checking overlap significantly. The specimen is subdivided into regular cuboids. The generated coordinate of the new particle center point identifies the cuboids that the new particle belongs to. The separation check is then performed between the new particle and only those particles that were previously placed in the same cuboid. To examine the efficiency of the technique, (Eckardt, 2009) provides numerical examples and compares the required time for creating specimens with and without the subdivision. The required time to generate the specimen is a fraction of the time that it takes when no subdivision is applied. An extensive description of the proposed technique is provided in (Häfner, Eckardt, Luther, & Könke, 2006) and (Eckardt, 2009).

Another innovative method to speed up the overlap check, is “grid-based approach” proposed by (Häfner, 2007). He considers the volume of the specimen, where the particles will be placed, as a domain grid. Knowing the coordinate of the particle center and its radii, the free space in the domain grid that is not yet occupied by any other particle can be determined. The next particle will be placed only in the free space of the domain grid. In other words, the occupied space in the specimen volume, will be cut off from the available space for particle placement. Comparing with the other solutions for particle separation check,

the main achievement in the grid-based approach is the complete elimination of the overlap check. (Bishnoi & Scrivener, 2009) used a similar approach known as cube grid subdivision.

Another honorable mention is the algebraic condition for the separation of two ellipsoids in 3D space that was proposed by (Wang, Wang, & Kim, 2001). Given X is a vector describing the coordinates, an ellipsoid is defined by Equation (2.6). The parameters in Equation (2.7) are similar to those in Equation (2.1).

$$X^T A_i X = 0 \quad X = \{x, y, z, 1\}^T \quad (2.6)$$

$$A_i = \begin{bmatrix} 1/r_{i,1}^2 & & & \\ & 1/r_{i,2}^2 & & \\ & & 1/r_{i,3}^2 & \\ & & & -1 \end{bmatrix} \quad (2.7)$$

The *characteristic equation* of two ellipsoids A_1 and A_2 are defined by

$$f(\lambda) = \det(\lambda A_1 + A_2) = 0 \quad (2.8)$$

(Wang, Wang, & Kim, 2001) prove that Equation (2.8) always has at least two roots and two ellipsoids A_1 and A_2 are separated if and only if Equation (2.8) has two distinct positive roots. (Sun, Guo, Guo, Wu, & Wang, 2020) employs the algebraic condition for the particle separation check in the mesoscopic model generated to study crack propagation in concrete.

The minimum spacing between particles is another criterion that needs to be taken into account when generating a specimen. This is usually implemented in the procedure for overlap check. For example, (Eckardt, 2009) considers a temporary enlargement of the particle radii before placement. The enlargement is defined as a function of the second-largest radius, and it can be adjusted by the relative enlargement factor ε_r defined by the user in Equation (2.9).

$$\Delta r = \varepsilon_r r_2 \quad (2.9)$$

(Bazant, Tabbara, Kazemi, & Cabot, 1990) compare the distance between the center points of two particles with the controlling length. For two successfully placed particles, the controlling length is equal to the sum of their radii and the minimum required spacing.

The take-and-place method is a very useful and popular technique that can be employed to generate a model at various observation scales. For instance, (Nguyen, Stroeven, & Sluys, 2012) use this method to create a microscale model of cement particles for simulation of the cement hydration.

2.3.2 Divide and fill method

It is a rather efficient method for obtaining a random particle model in 2D that was proposed by (Schutter & Taerwe, 1993). The method consists of two major steps: firstly, the material space is divided into separate areas; secondly, each area is filled with grain particles, taking into account the given grading curve and gravel content. Particles with circular or ellipsoidal shapes of different sizes are generated similar to the

take-and-place method. However, dividing the 3D space into separate portions is very complicated and unmanageable. Therefore, the method is limited to 2D square models. This means that the grading curve must also be converted into a 2D grading curve. This can be done based on some statistical consideration and through a mathematical calculation, which is described extensively in (Schutter & Taerwe, 1993).

The concept of Voronoi polygons¹ can be used for partitioning the concrete square: Let N number of arbitrary basic points A_i ($i = 1, 2, \dots, N$) be given. A square can be divided into N areas in such a way that each point in area j has a fixed point A_j as the nearest neighbor. In other words, each point in area j is closer to A_j than to any other basic point A_i . The boundary of area j is formed by drawing perpendicular lines to the lines connecting the basic points (Figure 2.2.a).

An easier approach is to use the Delaunay triangulation², also known as a Delone triangulation, for partitioning the concrete square: For the given N number of arbitrary basic points A_i ($i = 1, 2, \dots, N$) in a plane, triangulation can be constructed such that no A_i point is inside the circumcircle of any triangle (Figure 2.2.b). In (Grassl & Jirásek, 2010), the lattice elements of the mesoscale model are purely obtained by constructing the Delaunay triangulation. The edges of the triangles define the lattice elements, and the middle cross-section of the lattice elements are the edges of the Voronoi polygons (Figure 2.3).

One advantage of this method over the take-and-place method is the elimination of checking overlap between the particles; nevertheless, one can argue that the construction of Voronoi polygons or Delaunay triangulation can be as time-consuming as the overlap check.

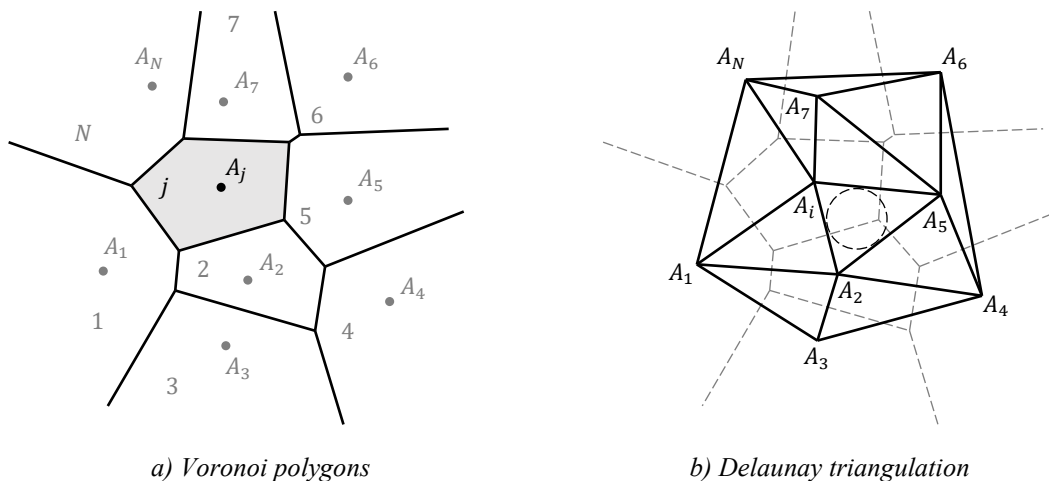


Figure 2.2 – Two common methods for dividing material space

¹ Named after Russian mathematician *Georgy F. Voronoy* who defined and studied the general n-dimensional case in 1908. Nevertheless, it is known that the German mathematician *Peter G.L. Dirichlet* used 2D and 3D Voronoi diagram in his study of quadratic forms, earlier in 1850.

² Discovered in 1934 by the Russian mathematician *Boris Nikolaevich Delaunay* or *Delone*.

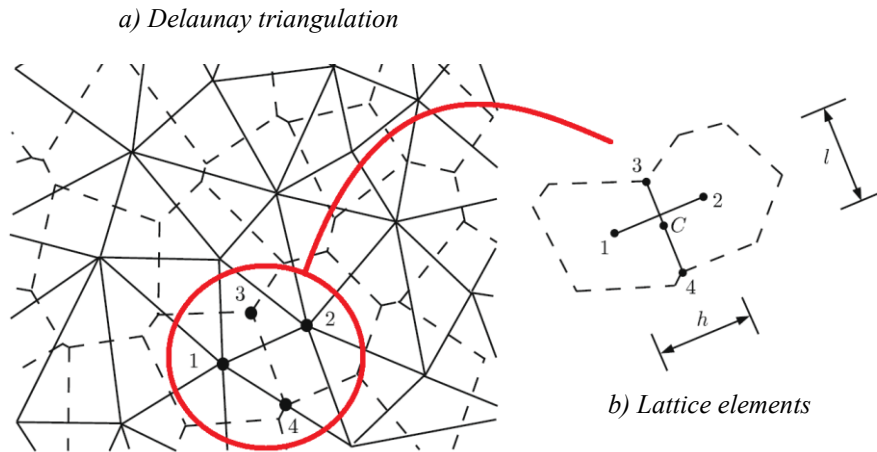


Figure 2.3 – Lattice element obtained from Delaunay triangulation by (Grassl & Jirásek, 2010)

2.3.3 Random particle drop method

In 1978 Cundall simulated the pouring of sand into a bucket. The particles are vertically dropped onto the heap of the sand deposit while they are allowed to roll or slide to a stable position after coming in contact with the deposit of the sand (Bazant, Tabbara, Kazemi, & Cabot, 1990). This simulation has motivated others to define a similar procedure for placing aggregate particles. For instance, (Van Mier & Van Vliet, 2003) employ a similar technique to model a mesoscopic specimen. After creating a collection of particles based on the grading curve, the particles are drawn from the collection and dropped from the top of a box that must be filled. The horizontal position at the top, from which the particle is released, is chosen at random. The particles fall vertically until they hit the particles that have been placed earlier. Some rules are applied to regulate the sliding and movement of the particles after dropping down. (Van Mier & Van Vliet, 2003) highlight that the method can be employed to achieve a higher particle density by using less computational effort.

Generating particles in this method may also follow the formulation that was provided in section 2.3.1. Although the method has been introduced for the mesoscale model, it is very suitable for simulation of the cement hydration at the microscale. The high particle compaction that it can deliver is beneficial for modeling cement particles.

2.3.4 Stochastic-heuristic algorithm

Inspired by the real process of concrete placing and compacting, (Leite, Slowik, & Mihashi, 2004) proposed a different approach for particle placement. The method was introduced for mesoscale modeling of a 3D specimen, but a 2D sample can be easily obtained by slicing the 3D model.

Ellipsoidal particles are generated in an almost similar manner to the take-and-place method. The middle radius of the ellipsoid, r_2 , is randomly selected within the size of two adjacent sieves. The other two radii are then computed as functions of r_2 in such a way that the required roundness of the particle is achieved

and the particle is retained in the lower sieve. The size of the sieves follows the prescribed grading curve. (Leite, Slowik, & Mihashi, 2004) start the placement procedure with the largest particle. The coordinates of the center point and the axis directions are randomly allocated to particles one by one. If the particle is completely inside the specimen and it does not overlap another particle, the position is granted. Otherwise, a stochastic-heuristic algorithm is employed to remove the overlap in a “stepwise” manner. The algorithm shifts the center point of the particle and rotates it around the axes to remove the overlap. The algorithm performs some local heuristic search in the neighborhood of the initial random position, using rotational and translational moves. In the “stepwise” movement of the particles, the step values are proportional to the ellipsoid axes and the step size is determined such that the desired aggregate content is achieved. (Leite, Slowik, & Mihashi, 2004) describe that in real concrete, the smaller particles are adjusted by the settlement of the larger particles. In that sense, the proposed mechanism begins with placing the larger particles, when the model volume still has free space and the probability of overlap is slim, and it shifts the following particles of the smaller size as it progresses, which simulates the smaller particles hitting the large particles and bouncing back until they have found their final position. This results in a more realistic structure than a purely random placement that is often used in the take-and-place method.

2.3.5 The unique method of (Contrafatto, Cuomo, & Gazzo, 2016)

Almost all methods that were presented in sections 2.3.1 to 2.3.4 follow a similar procedure for generating the particles: They all consider certain shapes (circular or ellipsoidal), and they generate various sizes according to the prescribed grading curve. But when it comes to the particle placement and separation check, each method has its own particularity and takes a different approach. This shows that the placement, or specifically the particle separation check is the main challenge for all methods. Motivated to address and overcome this challenge, (Contrafatto, Cuomo, & Gazzo, 2016) adopt a rather unique technique for modeling the microstructure of concrete that deviates from the other methods: their model does not require the physical size of the particles, nor does it require the overlap check.

The first step of the procedure is to select the number of phases in the model, e.g. a three-phase model consists of aggregate, cement paste, and voids. At the next step, each phase is solely characterized by its mechanical properties and has to comply with its volume fraction, e.g. as specified in the concrete mix-design. The mesh and the Gauss points are defined, and a Pseudo Random Number Generator (PRNG)¹ assigns one of the phases to each Gauss point in the mesh. The assignment depends on the generated number that is taken from an interval between 0 and 1. The interval is divided into sub-intervals according to the volume fractions of the components. The procedure of the phase assignment starts with an initial seed. If the initial seed is stored during the procedure, the phase assignment will become deterministic, which means

¹ PRNG refers to an algorithm that uses mathematical formulas to produce sequences of random numbers. It starts from an arbitrary initial seed and generates many numbers in a short time. If the initial seed is stored, the numbers can be reproduced at any time. Hence, the generated numbers are *deterministic*.

it can be regenerated during multi-scale analyses at any step by recalling the initial seed. Figure 2.4 illustrates the procedure.

(Contrafatto, Cuomo, & Gazzo, 2016) explain that the mesh generation and the phase allocation are carried out simultaneously. No particular mesh type is preferred, and no geometrical model of any phase has to be created. This overcomes the difficulty of generating particles with various shapes and sizes. Moreover, no special numerical procedure is required for overlap or separation check. To demonstrate and examine the performance of the procedure, numerical examples with successful results are provided in (Contrafatto, Cuomo, & Gazzo, 2016).

The proposed method by (Contrafatto, Cuomo, & Gazzo, 2016) is a time-saving technique because the RVE can be modeled with a solid cube without any explicit elements representing the phases in the material. The phases are distinguishable only at the Gauss points. This reduces modeling time, and it is certainly the main advantage of this method. For instance, the difficulty in creating a model for the ITZ will be discussed in section 3.4. Allocating the ITZ phase to the Gauss points certainly overcomes the encountered difficulty. However, the ITZ has not been considered in the numerical examples in (Contrafatto, Cuomo, & Gazzo, 2016). Therefore, it is unknown to what extent the technique can facilitate the ITZ modeling.

Eliminating the shape of the aggregate in the micromodel of concrete may not always be advantageous. For example, (Wang, Zhang, & Jivkov, 2016) study the mesomodel of concrete with different aggregate shapes: spherical, ellipsoidal, and crushed aggregate. Explicit modeling of the particles is required when the impact of aggregate shape on the concrete strength is investigated, and the phase allocation method is unsuitable for such a study.

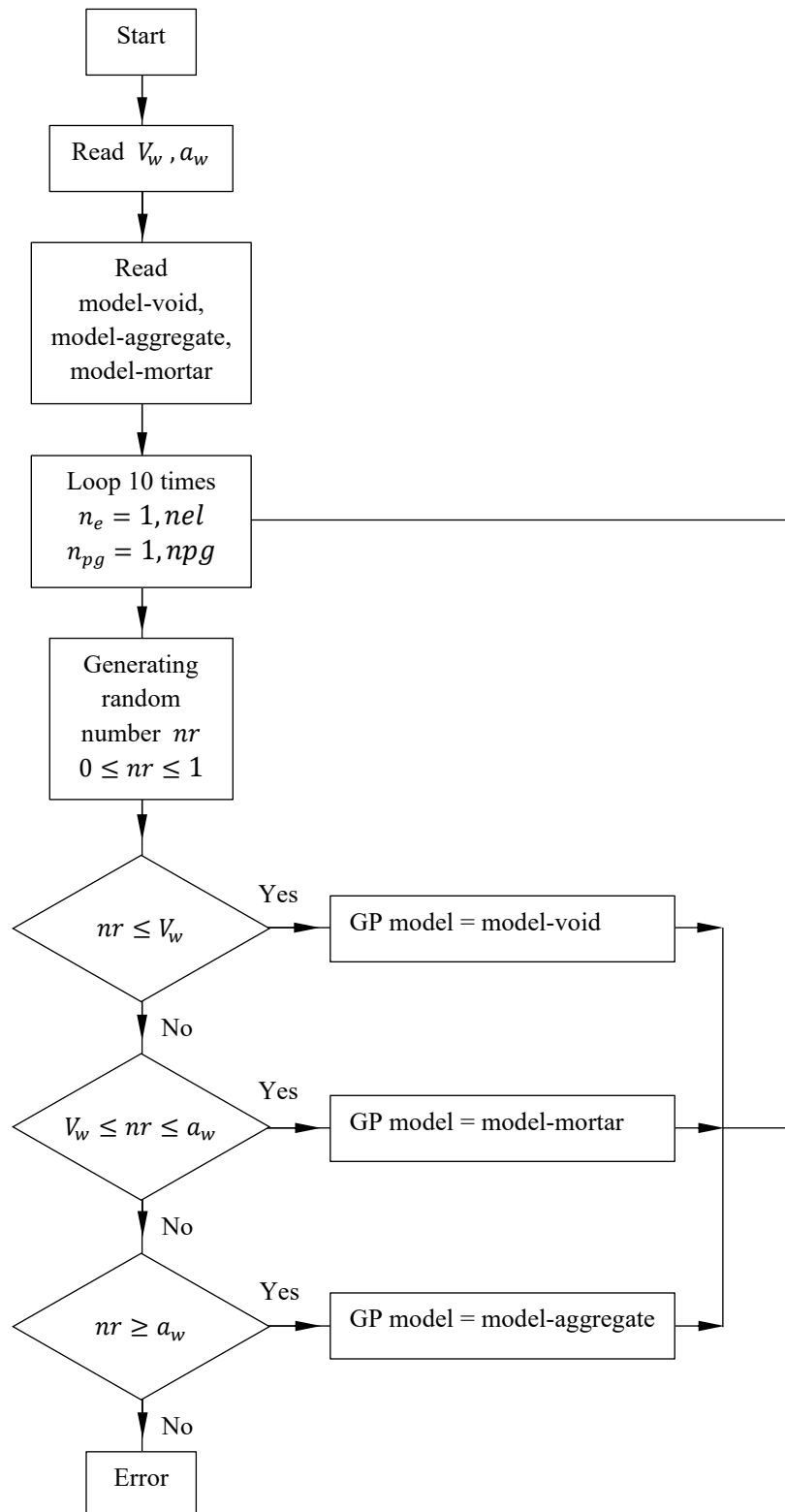


Figure 2.4 – Allocation procedure proposed by (Contrafatto, Cuomo, & Gazzo, 2016)

2.4 Multiscale Modeling of Concrete

Crack initiation and propagation in homogeneous materials can be described with classical fracture mechanics. When stress exceeds the tensile resistance of the material, debonding between atomic particles will occur and cracks start to develop. The theory was formed in the early 1900s and has been very well developed so far. (Kaplan, 1961) is probably one of the first researchers who applied classical fracture mechanics to concrete. However, the assumption of material homogeneity makes this theory rather limited to describe crack propagation in the heterogeneous structure of concrete. (Zaitsev & Wittman, 1981) state that in concrete, cracks begin to propagate far below the ultimate load and it will be controlled by high strength conclusions. Therefore, failure in concrete is a gradual degradation of the material.

One way for extending classical fracture mechanics to heterogeneous material is to model the entire structural element at meso- or microscales and to apply classical fracture mechanics to the distinct inclusions separately. This is known as Direct Numerical Simulation (DNS) in the literature, for example (Nguyen V. P., Valls, Stroeve, & Sluys, 2011) refer to it as a full-scale simulation method. But this approach would demand a sophisticated machine with very high computational power and such a simulation would be very time-consuming. Therefore, many “multiscale methods” for modeling have been developed to reduce computation time as much as possible and yet produce a heterogeneous model. In the multiscale method, different parts of a structural element are modeled at different scales. Ideally, the critical regions, where force or stress is at the highest, are modeled at lower scales to include heterogeneity, while the rest of the structure is modeled at macroscale with the homogeneous assumption of the material. Different combinations of scales, e.g. macro-mesomodel, meso-micromodel, have been introduced and examined by the researches, and examples of them will be reviewed later in this section.

Several classifications have been proposed by the researchers to categorize the available multiscale methods. (Feyel, 2003) classifies these methods into two main categories: 1) Sequential methods, 2) Integrated methods. (Belytschko & Song, 2010) suggest the same classification, but they call them hierarchical methods and concurrent methods, respectively.

In the first class, sequential methods, the detailed microscopic analysis provides the relevant mechanisms that are responsible for the macroscopic behavior. In these methods, numerical computation involves the RVE, which is a heterogeneous unit sample of material used to compute the response to a domain of inputs. (Belytschko & Song, 2010) explain that this response is precomputed for the strain at macromodel (the domain of input) and can be stored in various forms, such as parameters of a constitutive equation, or even a database. When the macromodel is run and macro-strain is obtained, this response is interrogated to obtain the stress for the macromodel (Figure 2.5). As (Feyel, 2003) describes it, only a purely macroscopic model is needed to be built using the internal variables for the “precomputed microscopic response”. However, one main drawback is the loss of some information, such as the interaction between different material inclusions which greatly influences the damage process. By summarizing several studies, (Eckardt, 2009) explains that the first class of methods employs the assumption of “scale separation”. The response of a

material point to the strain at the higher scale is computed at the lower scale through analysis of the heterogeneous RVE. In other words, the strain at the higher scale is transmitted to the lower scale as an input and the response of the RVE at the lower scale is returned to the higher scale as an output. Defining such an RVE is a complicated task and this will be reviewed in detail in section 2.4.1.1.

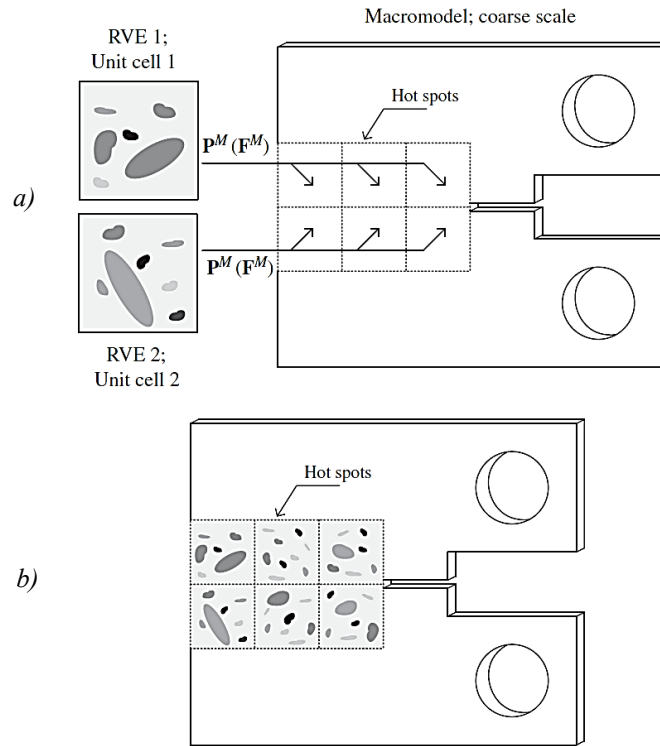


Figure 2.5 – Multiscale methods: a) hierarchical, b) concurrent, illustration by (Belytschko & Song, 2010)

In the second category, integrated or concurrent methods, the micromodel is embedded into the macromodel and run “concurrently”. Strong coupling of the models at two scales is enforced in form of the equilibrium and compatibility across the interface between the scales, and they are solved simultaneously (Belytschko & Song, 2010). (Eckardt, 2009) continues that in contrast to the first class, the second class does not require the assumption of “scale separation”. The model of the structural element is decomposed into two domains, namely the macrodomain and the microdomain. The microdomain is provided where explicit heterogeneity of material is a priority. For example, a mesoscale model is planted in a mid-span of a simply supported beam where the prediction of crack propagation is required.

Although the above classification can demonstrate two major approaches, there are other variants of the multiscale techniques that fall in between them. (Belytschko & Song, 2010) explain that the variation of these techniques creates a spectrum, spanning between the above two classes. When a strong formulation of the equilibrium is applied to the interface between the scales (strong coupling), the method is closer to

the second class (concurrent or hierarchical methods), and when the weak formulation is proposed for the interfacial conditions, the technique is more similar to the first class (sequential methods).

Regardless of the class of the methods, there are two main challenges in the multiscale modeling approach: i) Generating a model that represents the microstructure of the material at lower scale, ii) Communication between different scales through which, stress and strain are transmitted, back and forth, from one scale to the other (also known as “coupling”).

Generating a micromodel was discussed in section 2.3, and several methods were presented. Communication between the scales will be reviewed for two classes separately in the following sections. However, it is necessary to highlight that the link or so-called “coupling” of the scales is not usually seen as a separate computation. It is rather an implementation of a set of principles in the numerical solution of the multiscale model. Therefore, in the following sections, the implementation of these principles in the numerical solution will be reviewed as provided in the literature.

Finally, three developed multiscale models of concrete from the literature will be introduced to provide examples for the two classes.

2.4.1 Class I: Sequential methods

The main idea in the first class is the separation of scales: homogeneity and heterogeneity are defined at two separate scales. At the macrolevel, the macromodel represents the entire structural element with the assumption that the material is homogeneous, and the effective material properties describe the material behavior. The heterogeneity of the material is then considered at least in the critical regions. For instance, where cracks are expected to initiate and propagate. For every point in the critical region, the RVE is defined at a lower scale (e.g. mesoscale). The RVE computes the response of the material to the macrostrain (strain at the macrolevel) while taking into account some degree of material heterogeneity. The response is then returned to the higher scale.

Two main aspects of the method are the RVE and communication between the scales. For this purpose, (Feyel, 2003) proposed the FE^2 approach (FE-squared, developed and published earlier in 1998 in Feyel’s Ph.D. dissertation). In this method, simultaneous computation of the mechanical response at two different scales is performed: at the scale of the whole structure, and at the lower scale where the underlying microscopic RVE is placed. Three main ingredients are required for constructing such a model: (i) the RVE, (ii) a localization rule, and (iii) a homogenization rule. The localization rule determines the input that is sent from a higher scale to a lower scale, whereas the homogenization rule returns the micromechanical response from a lower scale to a higher scale (see Figure 2.6). These ingredients are reviewed and discussed in this section.

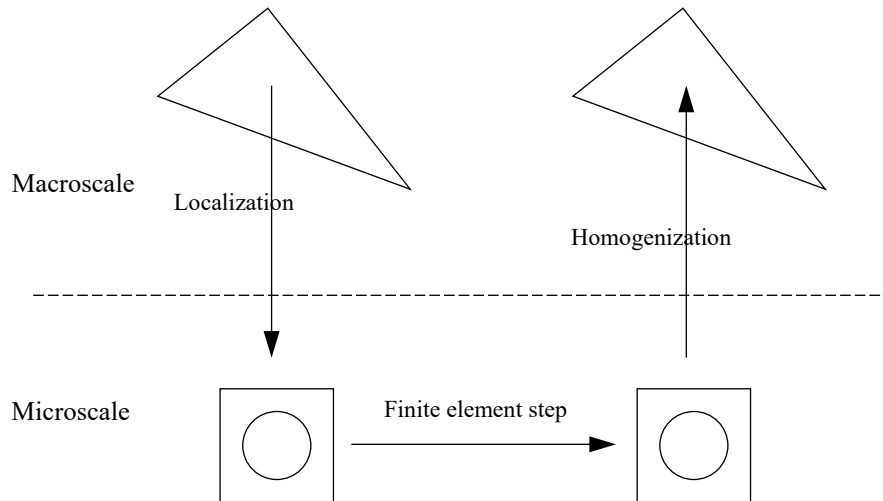


Figure 2.6 – FE² method developed by (Feyel, 2003)

2.4.1.1 Representative Volume Element (RVE)

The definition of RVE in the literature is not separated from its size. Since the element is supposed to represent the microstructure at one hand and provides the macro-response on the other hand, (Gitman, Askes, & Sluys, 2007) suggest that the RVE is required to be small enough to describe the microstructure and to be large enough to be constitutively¹ valid. However, finding the RVE that can hold a constitutive relationship between stress and strain, particularly in the nonlinear regime, is a debatable topic. This section provides a brief review of the definition of RVE and its size in the literature. The existence of RVE will be argued in section 2.4.1.3.

(Hill, 1963) describes that the RVE is a sample that, (i) is structurally entirely typical of the whole mixture on average, and (ii) contains a sufficient number of inclusions for the apparent overall moduli to be effectively independent of the surface values of traction and displacement, as long as these values are “macroscopically uniform”. Hill suggests that the contribution of the surface value can be made negligible by taking the RVE large enough.

(Hashin, 1983) discusses in an extensive survey of analysis of composite materials that the RVE is a detailed model of the material that is chosen to determine the corresponding effective properties for the homogenized macroscopic model. The RVE should be large enough to contain sufficient information about the microstructure that it represents, however it should be much smaller than the macroscopic body. Hashin remarks that it may be assumed that statistically homogeneous fields are statistically indistinguishable within different RVEs in a heterogeneous body. This implies that averaging stress, moments, etc. over any RVE is the same; thus, macro-body average and the RVE average are the same (Figure 2.7).

¹ Constitutive equation refers to the relationship between stress and strain in a solid material.

(Drugan & Willis, 1996) develop a constitutive relationship for composite materials and from that constitutive perspective, they emphasize that compared to the microstructure of the composite material, the smallest RVE must be sufficiently large to be statically representative of the composite and consequently a macroscopic effective constitutive relationship could be derived from it.

(Evesque, 2000) explores granular materials and indicates that the size of the RVE should be large enough with respect to the individual grain size to define the overall quantities such as stress and strain, but this size should also be small enough to hide macroscopic heterogeneity.

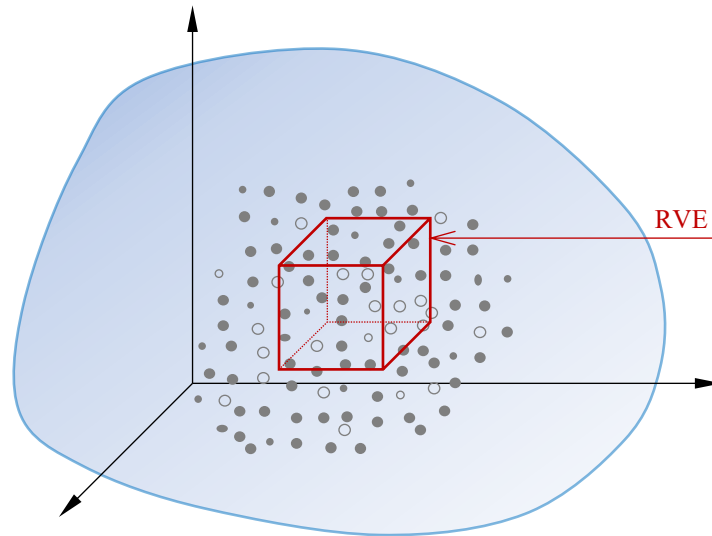


Figure 2.7 – Perception of the RVE by (Hashin, 1983)

All definitions disclose that the RVE should contain enough information about the heterogeneity of the material structure. Therefore, it needs to be large enough to include a sufficient number of constituents to be the representative of the material. On the other hand, it needs to be small enough so that the constitutive response, which is transmitted to the macrostructure, is not affected by its size and it can be produced at any point in the entire volume of the material. Today, this is known as Hill's energy condition, which implies that for an adequately defined RVE, the body averages, and the averages over the RVE are identical (Hill, 1963). This will be discussed further in the following section.

2.4.1.2 Data transmission between scales: Localization–Homogenization

(Feyel, 2003) emphasizes that any localization–homogenization scheme can be used in the FE^2 approach. The localization rule leads to a set of linear equations that are imposed on the RVE. The homogenization rule is a spatial average of the microscopic stress distribution in the RVE. The macromechanical behavior arises directly from what happens at the lower scale by formulating constitutive equations at the lower scale. Firstly, strain at the macrolevel is obtained. Then, a localization scheme is used to load the chosen RVE based on the macro-strain. After solving the RVE by the FEM scheme, the distribution of stress inside the RVE is obtained (micro-stress). A homogenization rule finally computes the macro-stress from the micro-stress and returns it to the macrolevel. (Feyel, 2003) provides a comparison of the FE^2 approach

with the classical scheme as shown in Figure 2.8. It is necessary to mention that the FE^2 approach does not require any constitutive equation to be written at the macrolevel because the relationship between stress and strain is only used at the lower scale for the RVE. One advantage of this method is the possibility of parallel computation (using separate processors at each level) to reduce computation time.

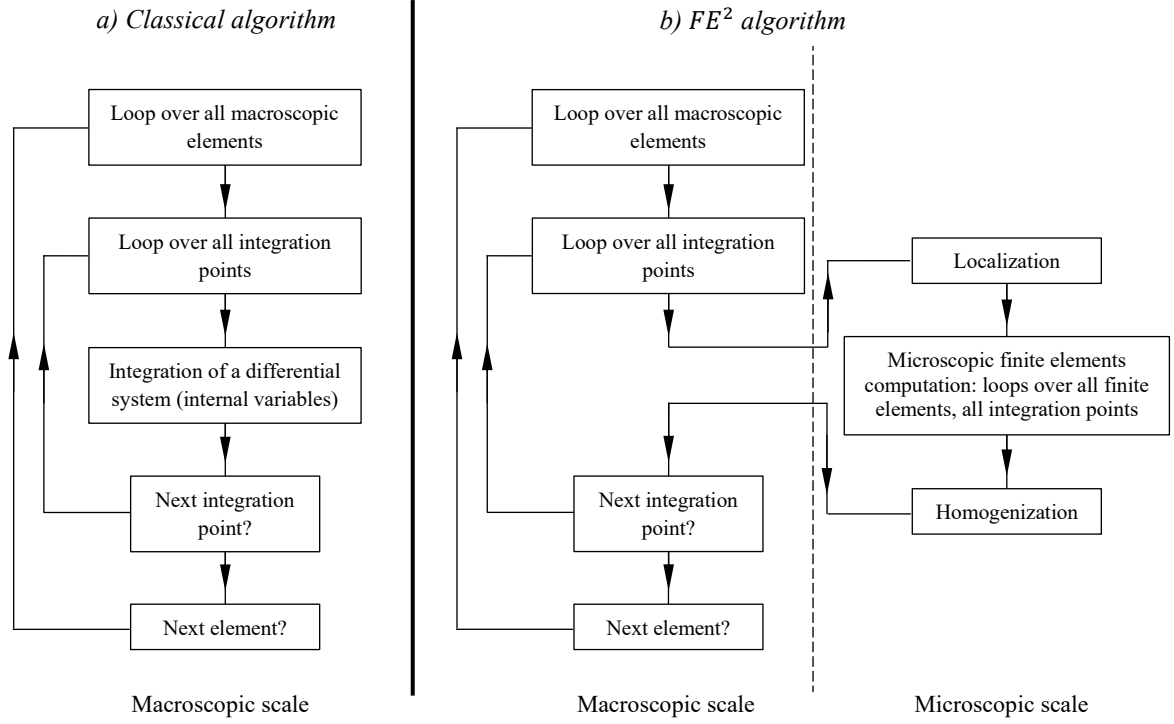


Figure 2.8 – Comparison between the classical and FE^2 model, illustration by (Feyel, 2003)

The Hill's energy condition, mentioned in section 2.4.1.1, states that for a body with perfectly bonded constituents and no body forces:

$$\langle \varepsilon \rangle_{\Omega} \cdot \langle \sigma \rangle_{\Omega} = \langle \varepsilon \cdot \sigma \rangle_{\Omega} \quad (2.10)$$

where Ω is the volume of the model and the equation means, as phrased by (Wriggers & Moftah, 2006), the volume averaged strain energy density of a heterogeneous material can be obtained from the averaged stress and strain formulated as below:

$$\langle \sigma \rangle_{\Omega} = \frac{1}{V} \int_{\Omega} \sigma_m \cdot d\Omega \quad (2.11)$$

$$\langle \varepsilon \rangle_{\Omega} = \frac{1}{V} \int_{\Omega} \varepsilon_m \cdot d\Omega \quad (2.12)$$

where subscript m refers to microscopic stress or strain. Equations (2.11) and (2.12) describe the standard homogenization scheme that is sometimes referred to as Hill's homogenization method in the literature (Mercer, Mandadapu, & Papadopoulos, 2015).

As highlighted at the beginning of section 2.4, one main purpose of multiscale modeling is the simulation of the progressive degradation caused by cracking at lower scales (microcracking). Therefore, damage degree should be considered in the homogenization scheme and this can be formulated through the classical Continuum Damage Mechanics. As per the formulation in (Wriggers & Moftah, 2006), the stress-strain law of “elasto-damaging” material can be defined by the following expression:

$$\sigma = (1 - D) \cdot \mathbb{C} \cdot \varepsilon \quad (2.13)$$

where \mathbb{C} is the effective stiffness tensor and D is the damage scalar and ranges from 0 for undamaged material to 1 for completely damaged material. It can be computed for concrete by:

$$D = \alpha_t D_t + \alpha_c D_c \quad (2.14)$$

where D_t and D_c are the damage variables in tension and compression, respectively. α_t and α_c are the weighting coefficient. In uniaxial tension $\alpha_t = 1$ and $\alpha_c = 0$ and in uniaxial compression $\alpha_t = 0$ and $\alpha_c = 1$. There are eight model parameters for determination of D_t and D_c , and they are measured from the uniaxial compression and tensile tests. Comprehensive formulation is provided in (Wriggers & Moftah, 2006). The above model of damage is also known as the Isotropic Damage Model in the literature.

2.4.1.3 Discussion

In the last two sections, a brief introduction to the definition of RVE and the standard localization-homogenization scheme in the FE^2 approach was presented. Both topics have been addressed and discussed in the literature by many researchers. Several problems have been raised and several solutions or alternatives have been developed to improve the sequential multiscale modeling. This section aims to bring these works into a discussion and underline their features.

Several definitions of the RVE were reviewed in section 2.4.1.1 and the importance of its size was emphasized. One of the early arguments is the existence of the RVE for concrete. (Ostoja-Starzewski, 2002) clarifies that RVE can be defined only in two situations: (i) unit cell in a “periodic” microstructure, and (ii) volume containing a large set of inclusions (mathematically infinite), possessing statistically homogeneous and “ergodic” properties. “Periodic” microstructure was defined in section 2.3 and illustrated in Figure 2.1. In “ergodic” materials, every sizable sample is equally representative of the whole. These two conditions imply that the RVE should have homogeneity and ergodicity of the material and contain enough number of micro-inclusions to ensure that it is independent of its overall size.

One of the well-known studies on the existence and size of the RVE is (Gitman, Askes, & Sluys, 2007). They considered a series of concrete mesomodels with different sizes. For each size, several samples with different volume fraction of the inclusions were created. The uniaxial tension test of the samples was simulated. The damage model of Equation (2.13) with a slightly modified formulation of the damage scalar was employed. Equations (2.11) and (2.12) were used for averaging micro-stress over the “entire”

RVE volume. By comparing the load-displacement (stress-strain) curves, as shown in Figure 2.9, they concluded that “*in the pre-peak regime, the mathematical expectation shows a constant behavior with respect to size, while the standard deviation converges with increasing size. Therefore, representative volumes can be found. Conversely, in softening (post-peak regime), the mathematical expectation of the material stiffness does not converge with the specimen size, in other words, every size exhibits as intrinsically different material behavior, and in conclusion, an RVE cannot be found.*” In short, when material enters the nonlinear regime, the RVE for determination of the material behavior at macrolevel cannot be found.

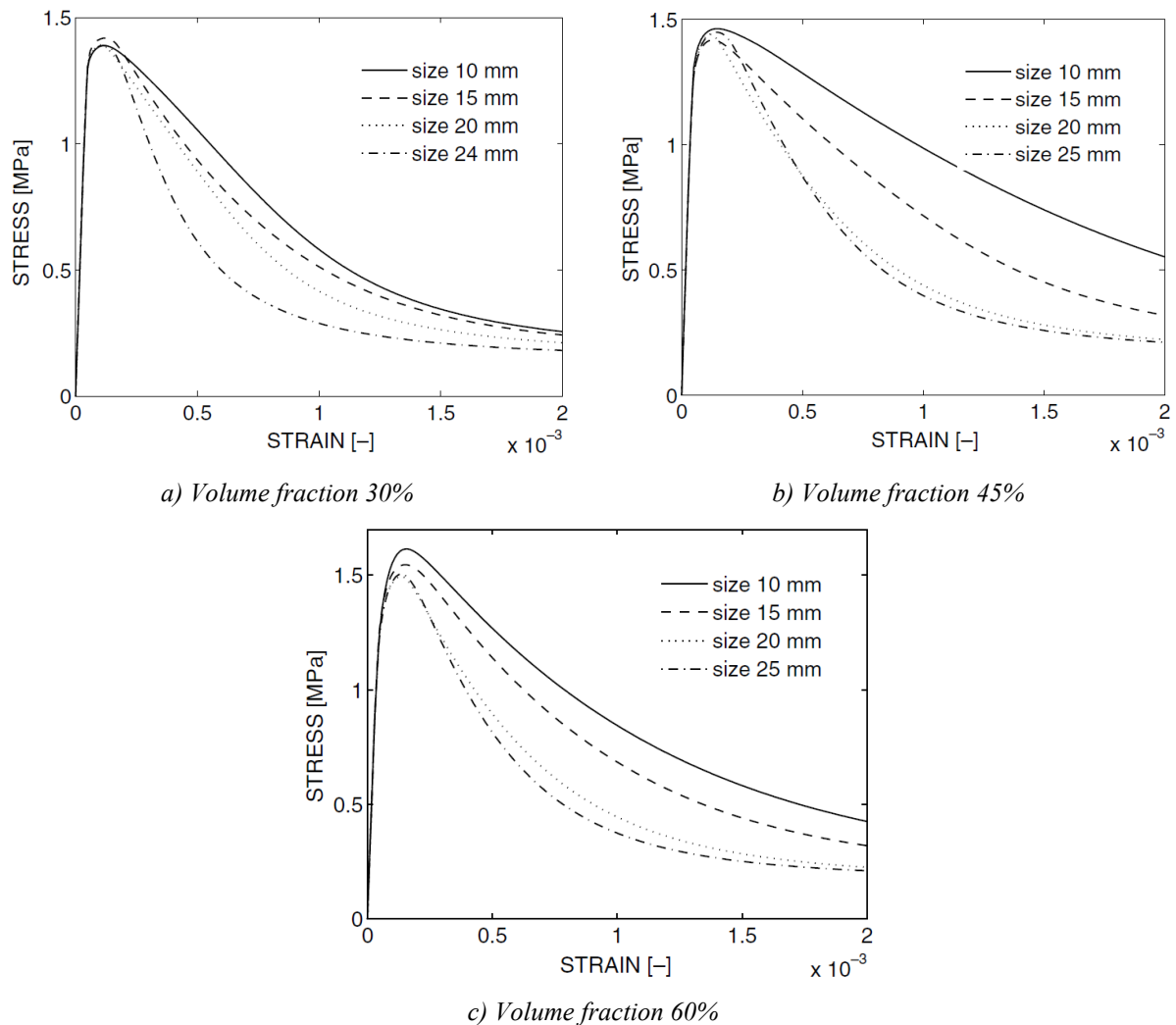


Figure 2.9 – Stress-strain curves of different volume fractions by (Gitman, Askes, & Sluys, 2007)

(Gitman, Askes, & Sluys, 2007) observed that the dissipated energy, expressed by the area under the stress-strain curve, decreased with respect to the increasing sample size, which showed an inverse proportionality of the dissipated energy with the sample size. They explained this inverse proportionality as follows:

“*The localization zone (at macrolevel) has a constant width (say w) independent of the sample size; the stored elastic energy is proportional to L^2 (L is the length of the RVE); the energy necessary to create the*

localization zone is proportional to $w \times L$; as a result, the ratio of dissipated (necessary) energy and elastic (available) energy is proportional to w/L ; Consequently, the dissipated energy scales with $1/L$.”

(Belytschko, Loehnert, & Son, 2008) developed an approach called Multiscale Aggregating Method. The notable feature of the method is an averaging scheme that deviates from the standard averaging in Equations (2.11) and (2.12). All subdomains in the RVE that exhibit crack are excluded in this approach. The resulted RVE is named “perforated unit cell” (Figure 2.10). Stress and strain are then averaged over the “perforated volume” instead of the “entire volume” by Equations (2.15) and (2.16).

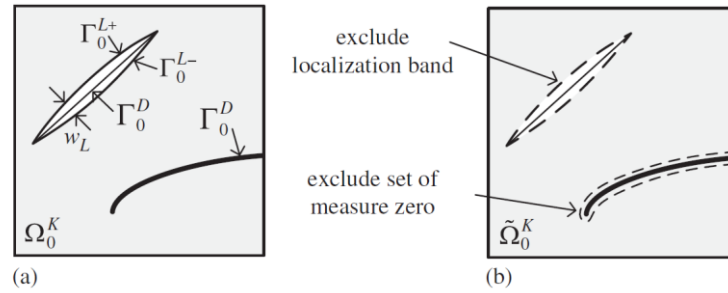


Figure 2.10 – a) Original unit cell at scale K , b) Perforated unit cell at scale K , illustration by (Belytschko, Loehnert, & Son, 2008)

$$\langle \sigma \rangle_{\Omega_0^K} = \frac{1}{\tilde{\Omega}_0^K} \int_{\tilde{\Omega}_0^K} \sigma_m \cdot d\tilde{\Omega}_0^K \quad (2.15)$$

$$\langle \varepsilon \rangle_{\Omega_0^K} = \frac{1}{\tilde{\Omega}_0^K} \int_{\tilde{\Omega}_0^K} \varepsilon_m \cdot d\tilde{\Omega}_0^K \quad (2.16)$$

The above averaging scheme overcomes the loss of RVE in the post-peak regime that was observed in (Gitman, Askes, & Sluys, 2007).

In a slightly different averaging approach, (Nguyen V. P., Valls, Stroeven, & Sluys, 2010) proposed “a failure zone averaging scheme”, in which stress and strain are averaged over the “active damaged domain” rather than the “entire domain” in the standard averaging. The “active damaged domain” in this approach is exactly the portion of the unit cell that was excluded in the method proposed by (Belytschko, Loehnert, & Son, 2008). Figure 2.11 illustrates the “active damaged domain”, and Equations (2.17) and (2.18) formulate the averaging scheme.

$$\langle \sigma \rangle = \frac{1}{\Omega_d} \int_{\Omega_d} \sigma_m \cdot d\Omega_d \quad (2.17)$$

$$\langle \varepsilon \rangle = \frac{1}{\Omega_d} \int_{\Omega_d} \varepsilon_m \cdot d\Omega_d \quad (2.18)$$

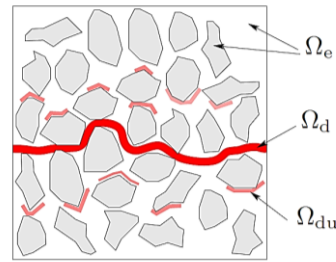


Figure 2.11 – The active damaged domain Ω_d defined by (Nguyen V. P., Valls, Stroeven, & Sluys, 2010)

(Nguyen V. P., Valls, Stroeven, & Sluys, 2010) explain that by averaging over the “entire volume” of the RVE, the non-damaged subdomain, which is still in the linear state, contributes to the averaging and this contribution results in a stress-strain curve that is size-dependent. However, by averaging over the “active damaged domain”, the linear contribution is filtered out, and the homogenized stress-strain, and consequently, the RVE for the post-peak regime can be obtained. (Nguyen V. P., Valls, Stroeven, & Sluys, 2010) provide numerical examples for both periodic and random microstructure to illustrate that employing their technique can ensure the existence of the RVE for the post-peak regime.

2.4.2 Class II: Concurrent methods

In the second class of multiscale methods, the microstructure is embedded into the macrostructure. The heterogeneity of the material is modeled in the domain of the microstructure while the material homogeneity is assumed in the domain of the macrostructure. In contrast to the first class, multi-scaling here does not mean separation of scales, nor does it mean resolving the RVE in a separated domain. In the second class, embedding the microstructure into the macromodel is an improvement on the assumption of the material structure at the macrolevel. The assumed homogeneous properties of the material are refined and replaced with a model that holds the heterogeneous structure of the material to a certain degree, and it can consequently estimate an improved and necessarily more accurate behavior of the material under the given stress or strain. In this respect, creating the RVE is no longer a matter of consideration. However, the coupling condition and linking between the coarse mesh of the macromodel and the fine mesh of the microstructure in FEM is the challenge in this class.

Several techniques for mesh refinement have been developed. (Hirai, Wang, & Pilkey, 1984) proposed the “exact zooming technique” that can be adopted in FEM. The proposed technique permits the stress distribution in the “zoomed area” to be estimated with high accuracy and less computational power. Each zooming is performed within the prior level of zoom. Static condensation¹ reduces the system to the degrees of freedom within the zoomed area of the structure (Figure 2.12). Then, the displacements of these DOFs are obtained, and consequently, all other responses of interest can be computed.

¹ Static condensation is a method that reduces the number of DOFs by expressing the unloaded DOFs in terms of the loaded DOFs. It is commonly used in Matrix Structural Analysis.

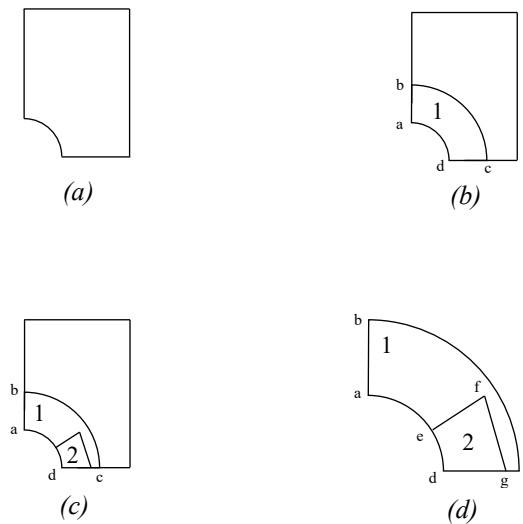


Figure 2.12 – Zooming technique: a) initial model; b) 1st zooming; c) 2nd zooming; d) details of the 2nd zooming

In concurrent methods, prioritized decomposition means adopting a micromodel (fine mesh) only in the critical regions of the structural element, where stress is concentrated or cracks are expected to develop. The rest of the structure has a macromodel (coarse mesh). In this sense, concurrent methods are similar to the exact zooming technique. Figure 2.13 illustrates one example of such a multiscale model.

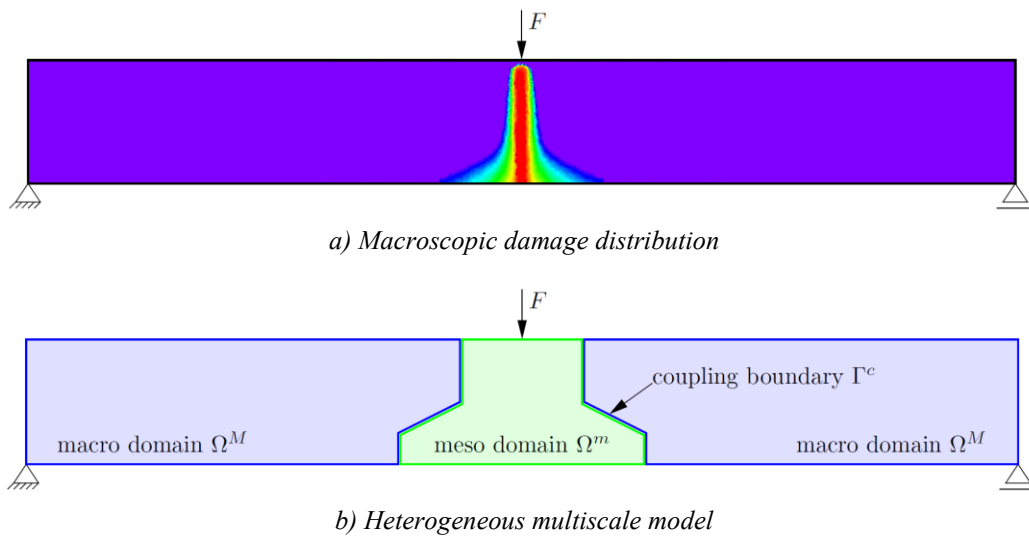


Figure 2.13 – Multiscale model (b) suggested for the macroscopic model (a), illustration by (Eckardt, 2009)

The methods in section 2.3 can be employed for generating a microstructure in the second class as well. The isotropic damage model, formulated in Equation (2.13), applies to this class too. The coupling of the two scales is discussed in the following section.

Coupling of two scales

A vital point in concurrent methods is the coupling of the macromodel and the model at the lower scale (microstructure). As illustrated in Figure 2.14, two domains are not only different in the size of the finite

element, but also the resolution: the macro-domain has homogeneous material properties, but the lower scale (here meso-domain) carries heterogeneous material properties (Eckardt, 2009).

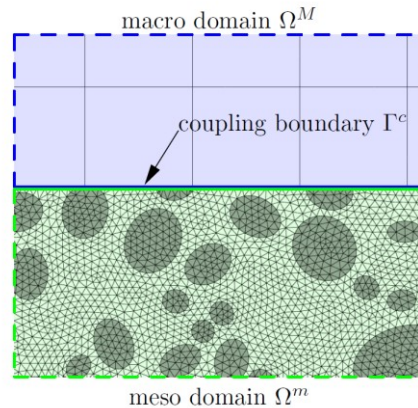


Figure 2.14 – Coupling of macro- and meso-domain, illustration by (Eckardt, 2009)

The coupling in multiscale simulation refers to the transformation of information between two nonconforming meshes. Different methods can be found in the literature for this purpose, such as nearest-neighbor interpolation, projection methods, and methods based on interpolation by splines. (de Boer, van Zuijlen, & Bijl, 2007) provide a comprehensive comparison between these three methods. They highlight several criteria that a coupling method should ideally satisfy. The most important among them are (i) global conservation of energy over the interface, (ii) global conservation of loads over the interface, (iii) accuracy, (iv) conservation of the order of the coupled solvers, and (v) efficiency defined as the ratio between accuracy and computational cost.

Nearest-neighbor interpolation method (NN) is the simplest and fastest method of transferring data from mesh A to mesh B. The search algorithm determines the point x_A in mesh A that is the closest to a given point x_B in mesh B. The value for the variable in x_B is then taken to have the same value as in x_A . However, this provides a satisfactory result only if the two grids are almost matching.

Projection methods provide a more accurate data transfer. The point x_B in mesh B is orthogonally projected on mesh A and the information in the projection point is then transferred to point x_B . This technique can especially be exploited when Gauss integration is used in the calculation of integrals over the interface.

Another alternative is to use spline-based methods. They are often applied in computer graphics and medical imaging that are out of the scope of this thesis.

(de Boer, van Zuijlen, & Bijl, 2007) specify that the above methods are direct ways to treat coupling. They can be easily and efficiently employed when explicit boundary conditions are considered. However, there are many situations when the boundary conditions are in fact “constraint relations”. For example, when a point on the boundary is required to follow a prescribed path, or when there is some form of cyclic continuity in the problem, which is very much the case in multiscale modeling. These types of boundary conditions are difficult to impose on a problem when direct solution methods are used. In cases that

Dirichlet¹ type boundary condition is imposed, the method of Lagrange multiplier can be used. For instance, when coupling the displacement between two structural sub-domains. (Babuska, 1973) provides a comprehensive study in this field.

(Eckardt, 2009) names two groups of approaches: strong and weak coupling. Constraint equations are used in the strong coupling approach, in which there is no relative displacement between any two points on the coupling boundary of two adjacent sub-domains. In the weak coupling approaches, such as the mortar method and Arlequin method, the sum (integral) of relative displacements of all points on the coupling boundary is equal to zero. However, this may result in a small gap or overlap (Figure 2.15).

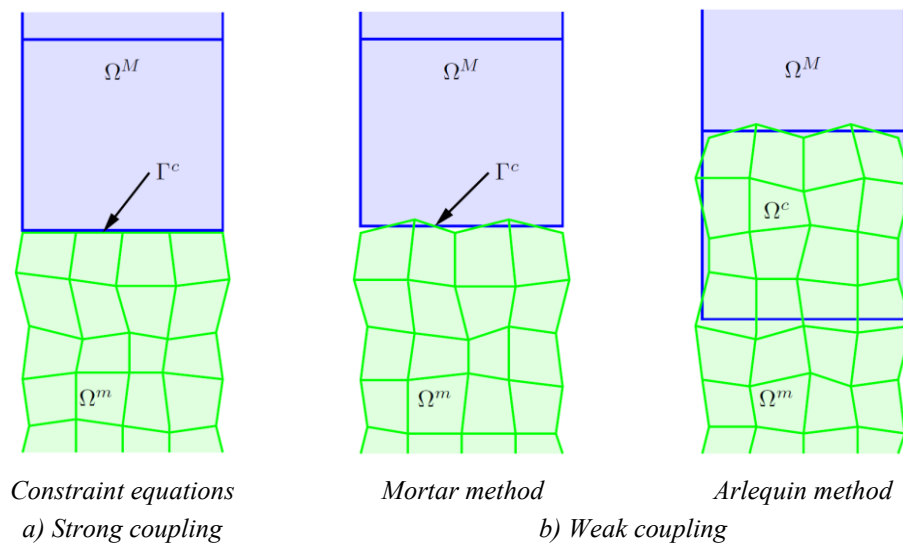


Figure 2.15 – Coupling methods, illustration by (Eckardt, 2009)

2.4.3 Adaptive Heterogeneous Method by (Eckardt, 2009)

Through an in-depth study (Eckardt, 2009) proposed a macro-meso model as an approach for multiscale simulation of concrete. In the proposed model, concrete is assumed to be homogenous at macrolevel and heterogeneous at mesolevel. An adaptive solution strategy detects the critical regions of the macromodel during the simulation and replaces it with the mesoscale model. The model can be applied to both 2D and 3D simulation.

The mesoscale model consists of ellipsoidal aggregate, mortar-matrix, and the ITZ in between them. The model is generated by using the take-and-place method with cuboidal subdivisions for particle separation check (as described in section 2.3.1). Zero-thickness ITZ is assumed, and aligned finite element discretization is suggested for the mesoscale geometry.

¹ Among five types of boundary conditions for differential equations (Dirichlet, Neumann, Robin, Mixed, and Cauchy), Dirichlet is predominant and prescribes a value to the dependent variable directly, e.g. $y(a) = A$.

The mortar method with Lagrange multipliers (weak coupling approach) is used for coupling of macro- and meso-domains, although constraint equations are well suited too. The Arlequin method is preferably avoided due to its complexity and time consumption.

Conversion of sub-domains from macro- to mesoscale is performed either by creating a new mesoscale sub-domain or by enlarging an existing meso-domain. The simulation starts with creating a macro model of the entire structure and progresses by using an “incremental solution strategy” with “updating variables’ history” after each step is converged. On the macroscale, the stress distribution is used as an indicator of model adaptation. If at least one integration point has principal stress larger than a certain limit (defined by the user), the macroscale elements in the vicinity of that point are replaced with mesoscale sub-domains. On the other hand, initiation of damage near the coupled boundaries indicates model adaptation on the mesoscale. For this purpose, the mesoscale sub-domain is divided into 3 zones: “inner zone” and “border zone” with the material nonlinearity, and “elastic border zone” with the linear elastic material property. If damage initiates in or develops into the border zone, mesoscale sub-domain, in the direction of damage evolution, will be adopted.

Several numerical tests and simulations were performed on various models and the results were reported in (Eckardt, 2009). In summary, the proposed method allows for explicit representation of the internal structure of the heterogeneous material, and simulation of nonlinear behavior of composite, in particular concrete.

2.4.4 The Macro-Micro Model of HCP by (Nguyen, Stroeven, & Sluys, 2012)

Simulation of cement hydration has been attempted by several researchers. (Bishnoi & Scrivener, 2009) developed a modeling platform called μic^1 (Mike) that enables the user to model the evolution of cement paste hydration. Motivated for modeling crack initiation in concrete, (Nguyen, Stroeven, & Sluys, 2012) proposed a macro-micro model of concrete, in which cement particles and their hydration are modeled at the microlevel (microlevel is one level lower than the mesolevel as reviewed in section 2.2).

By employing the take-and-place method, the 3D microscale geometry is created by generating spherical particles of cement following the prescribed particle distribution. Particle separation check is performed as per the grid subdivision method in (Bishnoi & Scrivener, 2009) that was reviewed in section 2.3.1.

Using the μic platform and below expression, the reaction of tricalcium silicate (C_3S) and water (H_2O) in the hydration is simulated.



In the above expression, V refers to the volume of the components and CSH is the silicate hydrates and CH is the portlandite. The degree of hydration with respect to time is expressed between 0 (for non-hydrated

¹ A free platform which can be downloaded at <https://sourceforge.net/projects/micepfl/files/micTheModel/>

cement paste) and 1 (for fully hydrated cement paste). The simulation follows a rather simple algorithm. The produced CSH from reaction precipitates¹ into particles and partially fills the space of the reacted C_3S that has left behind. The resulted CH fills the pores. These elements are used to determine the volume fraction of the capillary pores in the hardened cement paste (HCP). The comprehensive details of the hydration simulation can be found in (Bishnoi & Scrivener, 2009).

After the end of the hydration (the hydration end can be determined by the user), a 2D slice of the 3D geometry of the HCP is obtained for generating the mesh for FEM (Figure 2.16). The meshing starts with regular triangle/quadrilateral mesh, and it is refined by minimizing a cost function that is the sum of the energy value of all elements. The detailed procedure is described in (Nguyen, Stroeven, & Sluys, 2012).

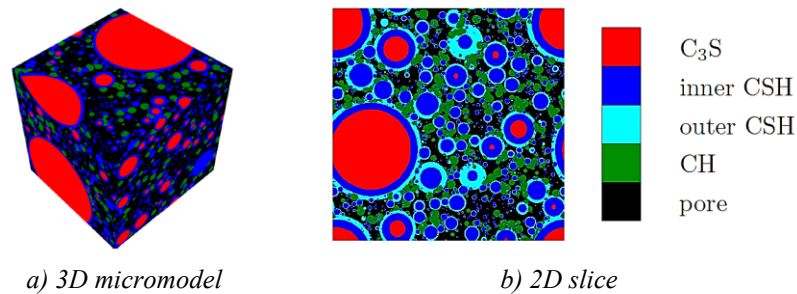


Figure 2.16 – 3D micromodel and 2D slice of the HCP, illustration by (Nguyen, Stroeven, & Sluys, 2012)

The isotropic damage model in section 2.4.1.2 and the “failure zone averaging scheme” in section 2.4.1.3 are used in the simulation. Furthermore, the “processor farming model” is adopted for parallel computation to reduce the analysis time. Tasks are distributed by one “farmer processor” to several “worker processors” and the results are sent back to the farmer processor. The efficiency is assured since the time spent on communication is small compared to the processing time for each task. The communication is only between the farmer and the workers, not between the workers. The farmer collects the displacement jumps and sends them to the workers. The workers will then solve the RVE problems and return the tractions and tangents to the farmer. The farmer uses the data to compute the stiffness and internal forces.

(Nguyen, Stroeven, & Sluys, 2012) provide three extensive numerical examples to examine the performance of the above multiscale scheme. The result proves that the mechanical behavior of the hardened cement paste can be very well simulated and using multiple processors and parallel computation can significantly reduce the processing time.

¹ In chemistry, “precipitation” means the creation of a solid from a solution through a chemical reaction.

2.4.5 A Macro-Meso model under cyclic load by (Sun, Guo, Guo, Wu, & Wang, 2020)

The cyclic fatigue crack in concrete is usually associated with a varying stress level that remains usually in the elastic stage. It is the periodic loading and unloading that contributes to crack propagation, not the stress exceedance of the tensile resistance. In this regard, (Sun, Guo, Guo, Wu, & Wang, 2020) developed a multiscale model of concrete for high cyclic loading to simulate the initiation and propagation of fatigue cracks. The structure is entirely modeled at the macrolevel with the homogeneous assumption of material. The crack is then calculated at the mesolevel and returned to the associated point at the macrolevel.

The three-phase mesoscale model is composed of aggregate, cement mortar, and the ITZ with thickness ranging between 0.02~0.05 mm. The ITZ thickness is non-zero in this model since the weak mechanical properties of the ITZ often become an important factor leading to crack initiation in fatigue. The take-and-place method is employed to create the aggregate. Ellipsoidal particles are generated for a prescribed grading curve. Particle separation check is done following the algebraic condition introduced by (Wang, Wang, & Kim, 2001), which was reviewed in section 2.3.1.

The localization-homogenization scheme is as same as the standard procedure that was described in section 2.4.1.2. However, the isotropic damage model in Equation (2.13) is required to be modified to capture the fatigue damage. For this purpose, the fatigue damage model proposed by (Guo, et al., 2009) is adopted as formulated by:

$$\begin{cases} \sigma_n = (1 - D_{n-1})\mathbb{C}^e \cdot \varepsilon_n \\ D_n = D_1 \left(\frac{n}{N}\right) D_2(\bar{\varepsilon}_n) \end{cases} \quad (2.20)$$

where n is the number of cycles, N is the fatigue life of material, D_1 and D_2 are the portion of damage relating to the number of cycles and deformation level, respectively, and \mathbb{C}^e is the initial stiffness tensor. Considering ε_t as the tensile strength of the material, D_1 and D_2 can be obtained from:

$$\begin{cases} D_1 = A \left(\frac{n}{N}\right)^3 + B \left(\frac{n}{N}\right)^2 + C \left(\frac{n}{N}\right) \\ D_2 = \alpha \left(\frac{\varepsilon_n}{\varepsilon_t}\right) \end{cases} \quad (2.21)$$

where A , B and C are material parameters determined by experiment, and α is the modal parameter. As it can be seen in Equation (2.20), stress at each cycle, σ_n , relies on the damage degree on the previous cycle, D_{n-1} . Therefore, the history of the damage degree is stored during the process. The above algorithm assumes that the damage accumulates in material only under tensile stress.

The ‘‘cycle block’’ technique is used in the analysis. A cycle block represents a certain number of cycles and it is smaller than the fatigue life of concrete, e.g. 10^4 cycles as one cycle block for a total fatigue life

of $2 \cdot 10^6$ cycles. With this respect, increasing the number of cycle blocks leads to improved accuracy and convergence. A cycle block consists of loading and unloading steps that can be summarized as follows:

- For cycle block n :
 - loading for computation:
 - if σ_{n-1} is compression $\rightarrow D_n = 0$ and $E_n = E_{n-1}$
 - else \rightarrow compute D_n using ε_{n-1} and
 - if $\varepsilon_{n-1} < \varepsilon_t \rightarrow E_n = (1 - D_n)E_{n-1}$
 - else $\rightarrow E_n = 0.1 E_{n-1}$
 - end if
 - update stress with $\sigma_n = (1 - D_n)\mathbb{C}^e \cdot \varepsilon_n$
 - Unload to prepare for the next cycle

In the above algorithm, only the number of tension cycles is used in computation of D . Fatigue cracks in macroscopic model expand according to Paris' law, given by:

$$\frac{da}{dN} = c(\Delta K)^m \quad (2.22)$$

where a is the crack length and $\frac{da}{dN}$ is the rate of fatigue crack growth over load cycle growth, K is the stress intensity factor, c and m are material coefficient obtained from experiment.

As soon as mesoscopic cracks have separated from the aggregate boundary and entered into the cement mortar matrix, they will be transferred into the macroscopic model. The coordinates of the end point of the longitudinal axis of the mesoscopic crack, are inserted into the macroscopic model as geometrical parameters to establish a macroscopic model with initial cracks. The end point coordinates are updated after each cycle block and the mesh is renewed if necessary. When the stress intensity factor K of any crack tip reaches the unstable fracture toughness of concrete, the crack will expand uncontrollably and transient break happens (Figure 2.17).

The stress intensity factor K in Equation (2.22) characterises the load around the crack tip and its magnitude can be determined through several methods. (Roylance, Fatigue, 2001a) offers an intensive review of these methods.

(Sun, Guo, Guo, Wu, & Wang, 2020) provide numerical examples to demonstrate that the proposed multiscale model can be employed to simulate the fatigue failure of concrete under high-cycle loading.

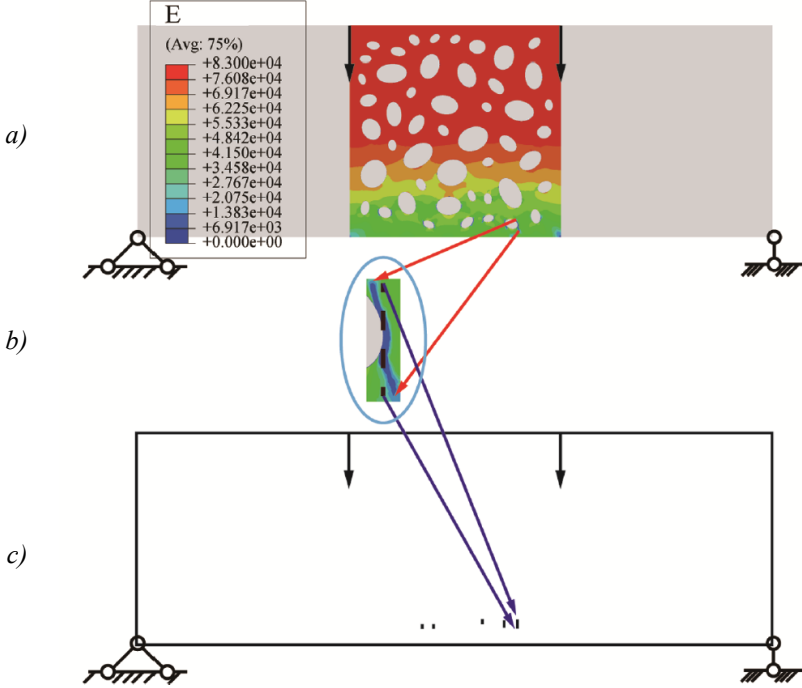


Figure 2.17 – Crack transfer between mesoscopic and macroscopic models: (a) the end state of mesoscopic model; (b) the effective generated crack and its central axis; (c) the initial state of macroscopic model. Illustration by (Sun, Guo, Guo, Wu, & Wang, 2020)

3 Generic Model for Post-failure Behavior of Concrete

3.1 Introduction

Post-failure behavior of concrete in tension is usually described by softening, which refers to decreasing stress and increasing strain simultaneously. To understand softening and its basic principles, consider the uniaxial tensile stress test in Figure 3.1 presented in (Jirásek, 2004).

The material is idealized as a bundle of fibers stretching in the stress direction (Figure 3.1.a). Each fiber is assumed to behave perfectly brittle (Figure 3.1.d), which means stress in a fiber immediately drops to zero when strain reaches a critical limit. The critical strain is different for each fiber. Hence, they fail progressively. The “initial sectional area” of the fibers is shown by A . The “effective sectional area”, denoted by \bar{A} , is equal to the initial area minus the area of the ruptured fibers (Figure 3.1.c). The “nominal stress” (σ) is defined as force per unit of the “initial area” and the “effective stress” ($\bar{\sigma}$) is defined as force per unit of the “effective area”.

Before reaching the failure strain (ε_t), the effective area is equal to the initial area. As the fibers start to fail, the effective area begins to decrease. At the end of the experiment, the effective area is equal to zero, indicating that all fibers are broken. The equilibrium requires that at each stage $\bar{\sigma}\bar{A} = \sigma A$. Therefore,

$$\sigma = \frac{\bar{A}}{A} \bar{\sigma} \quad (3.1)$$

The rupture of fibers at ε_t is sudden and the effective area reduces very quickly. To satisfy the above equation, the effective stress should increase to counterbalance the reduction in the effective area. However, the increasing rate of the effective stress is not fast enough. Consequently, the nominal stress reduces while the strain is still increasing. This phenomenon is called “softening” (Figure 3.1.e).

(Jirásek, 2004) specifies that softening results in serious mathematical and numerical problems if the constitutive law is formulated with the stress-strain relationship according to the standard continuum theory. (Bazant & Pijaudier-Cabot, 1987) associate this mathematical problem with the negative slope of the stress-strain diagram in softening branch that leads to the loss of material stability, or as (Belytschko & Song, 2010) explain, the loss of ellipticity in the partial differential equation in the equilibrium process.

Crack formation and crack growth play important parts in the performance of concrete after failure and a rational model should consider them to predict a realistic behavior. For this purpose, fracture mechanics offers several approaches to choose from. For instance, the “Stress intensity factor” focuses on stress near the crack tip to determine crack propagation (Roylance, 2001b).

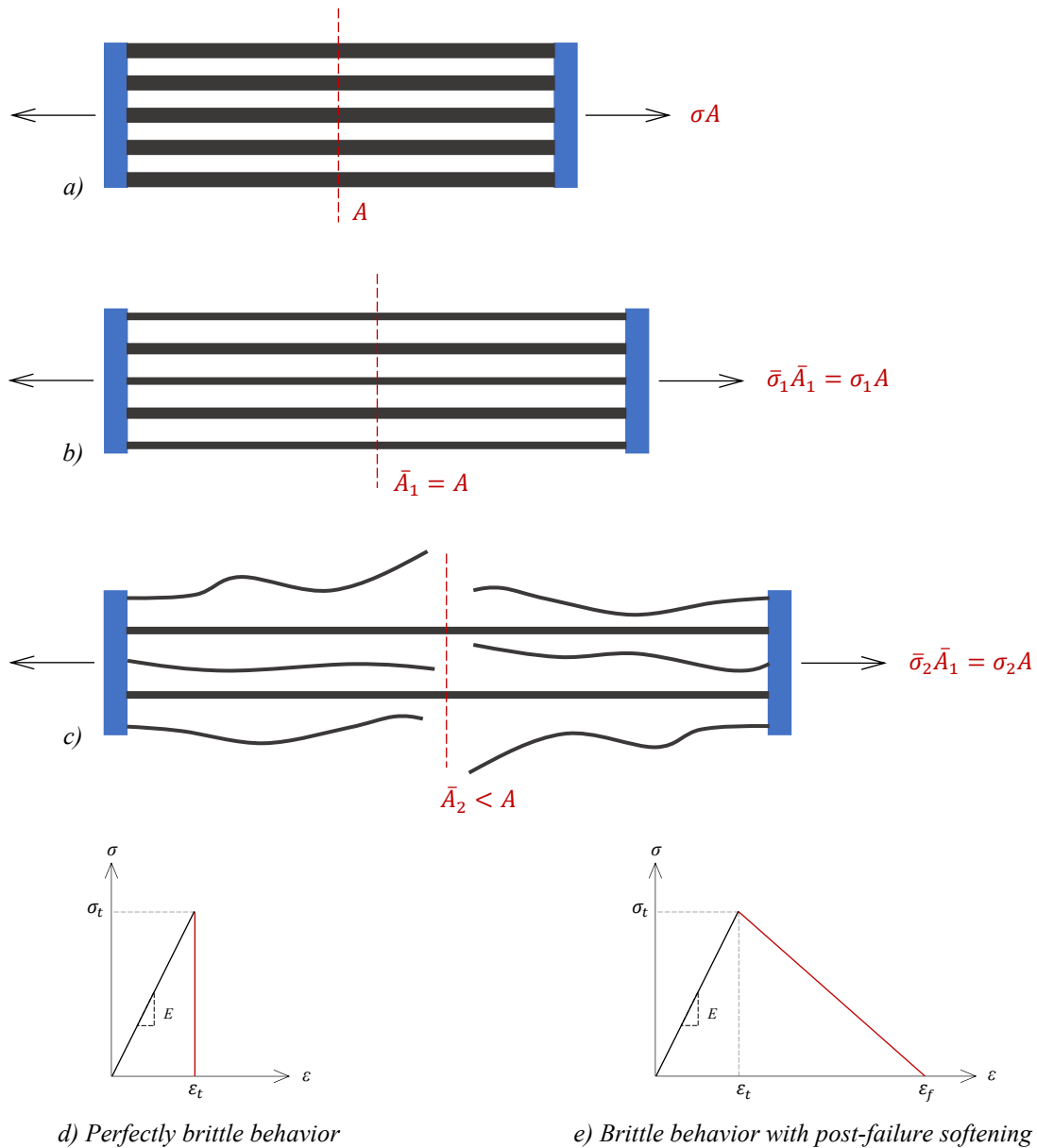


Figure 3.1 – Progressive failure of bundled fibers in uniaxial tensile stress test (Jirásek, 2004)

In the “energy balance approach”, a certain amount of energy is assumed to be stored in the unit area of the crack surface that needs to be overcome for the evolution of cracks. (Hillerborg, Modéer, & Peterson, 1976).

In the present study, a generic model for the post-failure behavior of concrete in tension is introduced. In this regard and to consider the heterogeneity of concrete into account, the material is modeled at mesoscale with three phases: aggregate, mortar matrix, and the ITZ. Both local and non-local formulations of the damage model are implemented and the results are compared. Abaqus is employed to solve the FEM model. Aggregate particles are generated with the help of two available open-source functions in Octave. For the implementation of the non-local damage, as well as the computation of the homogenized stress-strain diagram, two algorithms are developed and programmed in Octave.

3.2 Local formulation of the damage model

Continuum damage mechanics describes the progressive loss of material integrity by using a damage model. Its application in brittle fracture was initiated by (Kachanov, 1986). A damage model should possess variables that can characterize the loss of integrity in the material. In the simplest form, a single scalar parameter describes the damage. In the uniaxial tensile stress test of (Jirásek, 2004), presented in section 3.1, the ratio of the effective area over the initial area shows the integrity of the material at any moment during the test. Therefore, the loss of integrity is formulated by:

$$D = 1 - \frac{\bar{A}}{A} = \frac{A - \bar{A}}{A} = \frac{A_d}{A} \quad (3.2)$$

In the above equation, D is called the damage parameter and A_d is the damaged area. As seen in Figure 3.1, the damaged area is equal to zero at the early stages of the test, which results in $D = 0$. It then starts to grow as soon as strain becomes greater than ε_t . At the end of the test, all fibers are ruptured and the damaged area is equal to the initial area. This creates an upper limit of 1.0 for D . The material is completely damaged when $D = 1$.

$$\begin{cases} D = 0 & \varepsilon \leq \varepsilon_t \\ 0 < D \leq 1.0 & \varepsilon_t < \varepsilon \end{cases} \quad (3.3)$$

By combining Equations (3.1) and (3.2):

$$\sigma = (1 - D)\bar{\sigma} \quad (3.4)$$

As shown in Figure 3.1.e, the material remains linear elastic for strain smaller than ε_t . Hence, the relationship between the nominal stress and strain is described by Hooke's law. At this stage, the effective stress is equal to the nominal stress. Therefore, the effective stress is governed by Hooke's law too.

$$\bar{\sigma} = E\varepsilon \quad (3.5)$$

By combining Equations (3.4) and (3.5):

$$\sigma = (1 - D)E\varepsilon \quad (3.6)$$

Equation (3.6) is the constitutive law capable of describing post-failure behavior, and it is frequently referred to as the "simple isotropic damage model" [(Kachanov, 1986), (Bazant & Pijaudier-Cabot, 1987), (Eckardt, 2009), (Grassl & Jirásek, 2010), (Nguyen, Stroeven, & Sluys, 2012)]. It is necessary to mention that the damage parameter in the above context is often shown by ω in the classic literature, particularly when referring to the local damage model. However, it is shown by D throughout this study.

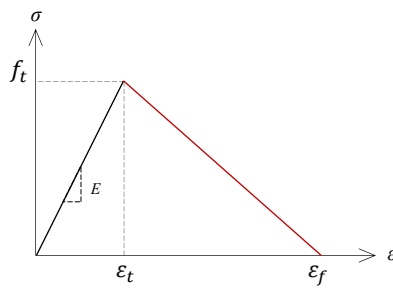
In Equation (3.3), the failure strain (ε_t) defines the criteria for damage initiation, but the damage parameter in Equation (3.2) is not a function of strain. For consistency in the formulation, the damage parameter is defined as a function of strain too (Jirásek, 2004).

$$D = d(\varepsilon) \quad (3.7)$$

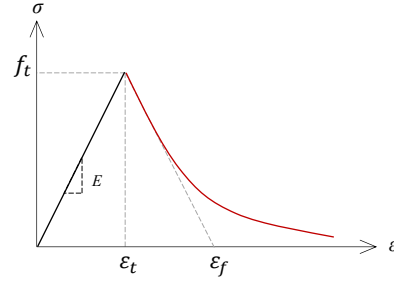
Several formulas can be found in the literature for $d(\varepsilon)$. For instance, (Jirásek, 2004) explains that $d(\varepsilon)$ can be directly identified from the uniaxial stress-strain curve. The linear softening (Figure 3.2.a) can be formulated by Equation (3.8), and the exponential softening (Figure 3.2.b) by Equation (3.9).

$$d(\varepsilon) = \begin{cases} 0 & \varepsilon \leq \varepsilon_t \\ \frac{\varepsilon_f}{\varepsilon_f - \varepsilon_t} \left(1 - \frac{\varepsilon_t}{\varepsilon}\right) & \varepsilon_t \leq \varepsilon \leq \varepsilon_f \\ 1 & \varepsilon_f \leq \varepsilon \end{cases} \quad (3.8)$$

$$d(\varepsilon) = \begin{cases} 0 & \varepsilon \leq \varepsilon_t \\ 1 - \frac{\varepsilon_t}{\varepsilon} \exp\left(-\frac{\varepsilon - \varepsilon_t}{\varepsilon_f - \varepsilon_t}\right) & \varepsilon_t \leq \varepsilon \leq \varepsilon_f \end{cases} \quad (3.9)$$



a) Linear softening



b) Exponential softening

Figure 3.2 – Stress-strain diagram with two alternatives for softening branch

In the above equations, ε_t is the strain at the failure stress (f_t) and ε_f is a parameter that controls the slope of the softening branch and it will be discussed later (Figure 3.2).

In an incremental analysis, the damage parameter at each stage should be computed for the strain at the previous stage. This means that ε in Equations (3.8) and (3.9) is the largest strain that was previously reached, not the strain at the current stage (Jirásek, 2004).

In this study, Equation (3.9) is used for the computation of the damage parameter.

Problem statement: spurious mesh sensitivity

The damage model described by Equation (3.8) or (3.9) suffers from mesh sensitivity when implemented in FEM (Bazant & Pijaudier-Cabot, 1987). Mesh sensitivity means that the analysis result depends on the mesh size and it will change if the mesh size is altered. (Jirásek, 2004) provides a comprehensive explanation for mesh sensitivity by using a uniaxial tension test of a bar as illustrated in Figure 3.3. A summary of the test is provided here.

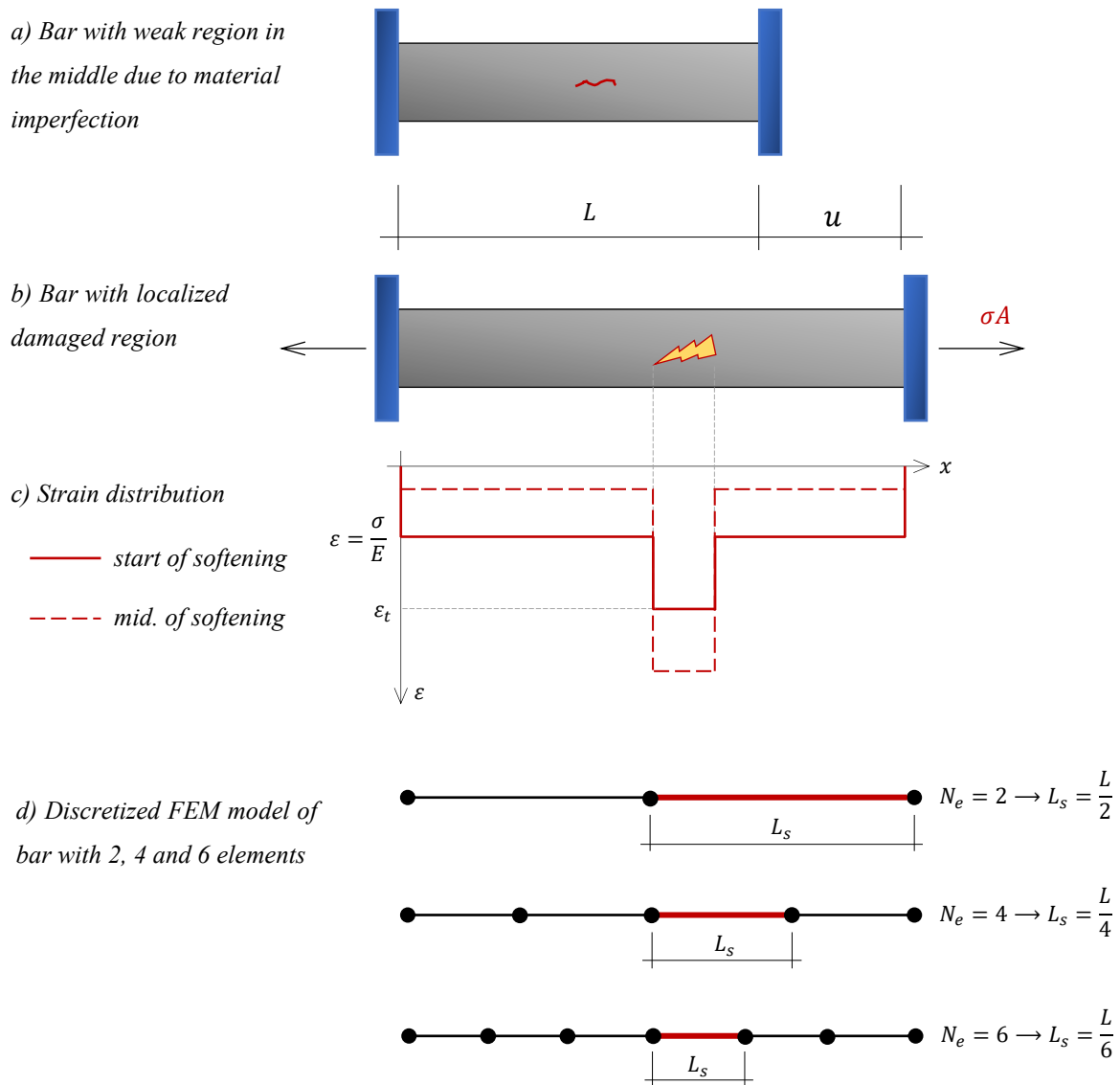


Figure 3.3 – Uniaxial tension test of a bar with material imperfection in the middle

The material properties and the sectional dimensions of the bar cannot be perfectly uniform in reality. For instance, the material strength in a small region in the middle of the bar could be slightly lower than the other regions (Figure 3.3.a). Therefore, the weaker region fails earlier than the other regions (Figure 3.3.b). Softening starts and the stress decreases in the weak region. Consequently, the stress in the other zones decreases too. However, the other zones are still in the elastic state; therefore, the strain reduces in them as the stress declines. In contrast, the strain in the weak region increases constantly. This means that the softening behavior of the entire bar is governed mainly by the weak region. The strain-distribution diagram of the bar at the beginning of softening can be represented by a piecewise constant function as shown in Figure 3.3.c by the solid line. By capturing the strain at one sample moment during softening, the strain-distribution diagram would be the dashed line in Figure 3.3.c.

Suppose that the bar is discretized by two elements in such a way that the weak region is perfectly captured by one node. The numerical algorithm will detect the softening of the weak region and extend it over one element. Therefore, the length of the softening region (L_s) will be $L/2$ (Figure 3.3.d). If the bar is

discretized by a larger number of elements, for instance, N_e elements, the algorithm will similarly detect the weak region and extend it over one element. Hence, the length of the softening region will be L/N_e (Figure 3.3.d). This procedure persists regardless of how fine the mesh size is. Since L_s is unknown, it remains unclear which discretization can result in the true length of the damaged region. For this reason, it is said that the analysis result is sensitive to the mesh size (Jirásek, 2004).

Mesh sensitivity is caused by the fact that in the local formulation of the damage, strain at any material point (and consequently the damage parameter) is determined independently and without considering strain at the neighboring material points. Nevertheless, there are several remedies for reducing mesh sensitivity while using the local formulation. In this study, the approach proposed in (Hillerborg, Modéer, & Peterson, 1976), which is based on the fracture energy, is employed to reduce mesh sensitivity.

Hillerborg energy approach: a remedy for mesh sensitivity

(Hillerborg, Modéer, & Peterson, 1976) propose a model for stress distribution at the tip of an opening crack (mode I fracture). According to their model, a crack initiates when the tensile stress at the crack tip reaches the tensile strength f_t . When the crack opens, the stress does not fall to zero at once, but it decreases gradually with increasing crack width. At a point where the crack width is equal to w_1 , the stress will be equal to zero (Figure 3.4.a). This means that the stress may remain present in the entire crack, as long as the crack width is smaller than w_1 .

Opening a crack requires energy because there is stress to be overcome. (Hillerborg, Modéer, & Peterson, 1976) demonstrate that this energy, which is required to open a crack from zero to or beyond w_1 , can be calculated by

$$G_f = \int_0^{w_1} \sigma \cdot dw \quad (3.10)$$

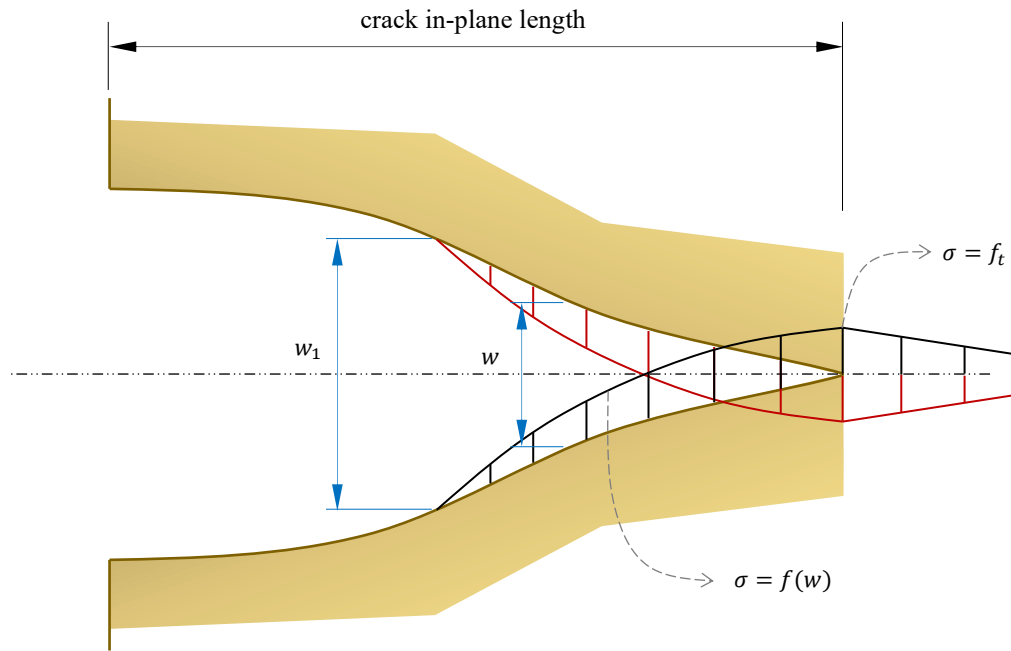
Equation (3.10) corresponds to the area under the stress-crack width curve in Figure 3.4.b. The authors propose a linear relationship between the stress and the crack width to simplify the curve (Figure 3.4.c). By this simplification, the integral in Equation (3.10) will be equal to the area of the triangular diagram.

$$G_f = \int_0^{w_1} \sigma \cdot dw = \frac{f_t w_1}{2} \quad (3.11)$$

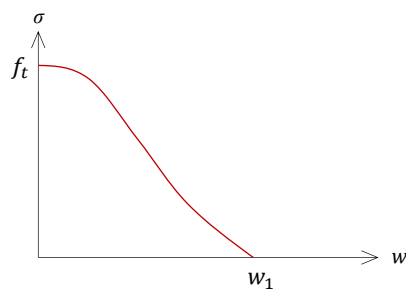
When G_f is determined by the experiment, w_1 can be computed by

$$w_1 = \frac{2 G_f}{f_t} \quad (3.12)$$

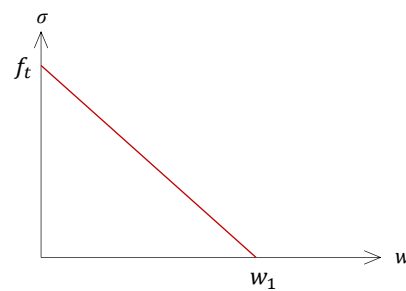
(Hillerborg, Modéer, & Peterson, 1976) specify that for ordinary concrete, G_f/f_t seems to fall between 0.005 and 0.01. The authors also highlight that the proposed model can be used in the FEM with coarse mesh because the absorbed energy is not very sensitive to the mesh size.



a) Stress distribution diagram of an opening crack



b) Variation of stress with crack width



c) Simplified $\sigma - w$ diagram

Figure 3.4 – Proposed model for an opening crack by (Hillerborg, Mod er, & Peterson, 1976)

It should be noted that the crack out-of-plane length is not included in the above model. Therefore, G_f is the required energy for opening a crack on a surface. To convert G_f to a volume-specific parameter, G_f should be divided by the crack out-of-plane length. (Eckardt, 2009) considers the out-of-plane length to be a numerical parameter proportional to the nonlocal interaction radius R . Therefore, the volume-specific fracture energy can be obtained by

$$g_f = \frac{G_f}{\beta R} \quad (3.13)$$

In Equation (3.13), β is a parameter representing the damage distribution in the fracture zone. (Eckardt, 2009) determines β by simulation of the uniaxial tension test of a concrete specimen and obtains a value of 1.7 for it. The nonlocal interaction radius R will be introduced and discussed in section 3.3.

In a pioneering work, (Bazant & Oh, 1983) demonstrate that the fracture energy can also be linked to the area under the uniaxial stress-strain diagram. Therefore, w_1 will be converted to ε_f (fracture strain). ε_f is the largest strain that concrete encounters when following the unloading path of the softening branch in Figure 3.2. The uniaxial stress at ε_f is theoretically zero.

To conclude this section, the definition of fracture energy by (Bazant & Oh, 1983) is provided:

The fracture energy G_f is the energy consumed in the formation and opening of all microcracks per unit area of plane (or per unit volume when denoted by g_f).

Implementation in Abaqus

As stated in section 3.1, Abaqus is employed in this study to solve the FEM problem. This section describes the implementation of the local damage model in Abaqus.

(Jirásek & Zimmermann, 1998) decomposed strain into an elastic part and an inelastic part caused by cracking. The elastic part of the strain is related to the stress by the linear elasticity, whereas the stress-strain relationship for the plastic part is formulated by the constitutive equation of the damaged material such as Equation (3.6). The decomposition of strain can be defined in Abaqus for modeling the plasticity of brittle materials such as concrete or mortar (Abaqus documentation, 2020).

For a better understanding of strain decomposition, consider the mortar specimen in Figure 3.5.a. As illustrated in Figure 3.5.b, the mortar material under uniaxial tension shows a linear stress-strain relationship up to the point $(\varepsilon_t, \sigma_t)$ and exhibits a softening behavior beyond that point similar to concrete [(Huang, Yang, Ren, Liu, & Zhang, 2015), (Wang, Jivkov, Engelberg, & Li, 2018)].

Suppose that an incremental load F is applied to the specimen (Figure 3.5.c). As F increases, the stress-strain relationship follows the linear path between points 1 and 2 with the elastic Young's Modulus E_0 . Once F becomes larger than F_t , softening starts and the stress-strain relationship enters the path between points 2 and 3 (Figure 3.5.e). As per the criteria for crack initiation, which was discussed earlier in this section, the specimen is cracked at this stage. For simplicity, the accumulation of the opening cracks is illustrated by a single crack in Figure 3.5.c (Belytschko, Loehnert, & Son, 2008). The width of the opened crack is shown by Δx^{pl} and it is called the plastic displacement (Abaqus documentation, 2020).

By unloading the specimen, the stress-strain relationship follows the declining path of 3 – 4 (Figure 3.5.e). Due to elasticity that still exists in the undamaged material between the cracks, the specimen retracts during unloading by an elastic displacement shown by Δx_o^{el} in Figure 3.5.d. The stress-strain relationship in the undamaged area between the cracks is linear elastic with the same slope as the path 1 – 2 [(Eckardt, 2009), (Jirásek & Zimmermann, 1998)]. Δx_o^{el} corresponds to the elastic part of the strain decomposition in (Jirásek & Zimmermann, 1998).

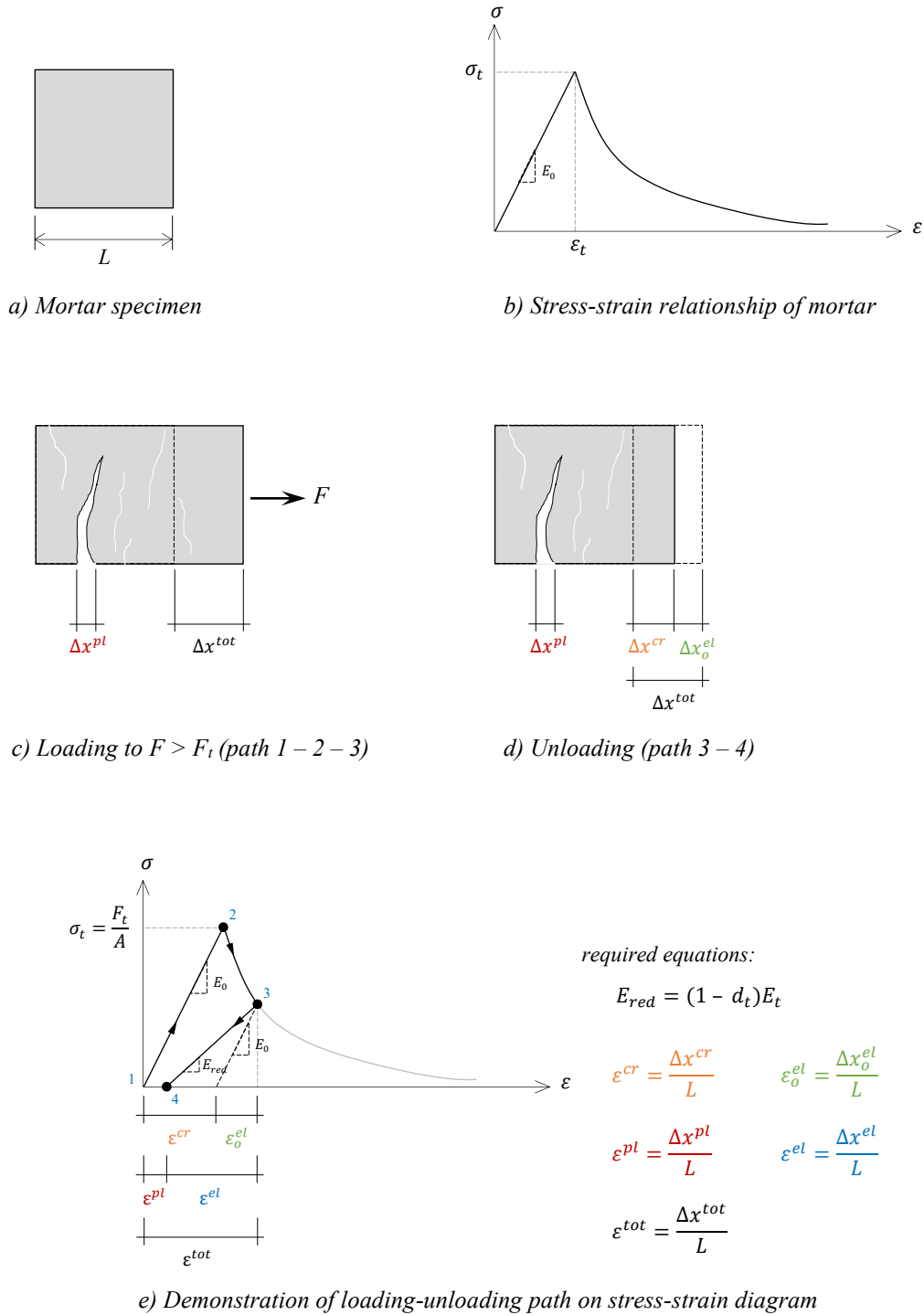


Figure 3.5 – Strain decomposition of mortar specimen under incremental tensile force

The total displacement Δx^{tot} minus the elastic displacement Δx_0^{el} is equal to the cracking displacement Δx^{cr} (Figure 3.5.d). The cracking displacement is the inelastic component of the total displacement that the specimen should undergo to experience the irreversible crack Δx^{pl} (Kim & Abu Al-Rub, 2011).

The unloading path between points 3 and 4, shown in Figure 3.5.e, is governed by the constitutive law for the damaged material given by Equation (3.6) and the damage parameter as a function of strain given by

Equation (3.7). By dividing both sides of Equation (3.6) by strain, the reduced Young's modulus is obtained (Kim & Abu Al-Rub, 2011).

$$E_{red} = (1 - d_t)E_0 \quad (3.14)$$

d_t in Equation (3.14) is the damage parameter computed at point 3. The subscript t refers to tension and E_0 is the initial Young's modulus of the undamaged material. At point 4, where the stress is equal to zero, the non-zero strain corresponds to the permanent plastic displacement Δx^{pl} . Figure 3.5.e demonstrates the loading and unloading path on the stress-strain diagram and it shows the equations required to convert the displacement to the corresponding strain.

The Concrete Damaged Plasticity (CDP) is an integrated function in Abaqus that allows the user to describe the damage with the strain decomposition model. The user can define the softening behavior of the material by providing the stress-cracking strain relationship ($\sigma_t - \varepsilon^{cr}$) in tabular form as an input. Similarly, the damage evolution is specified as an input by the relationship between the damage parameter and the cracking strain ($d_t - \varepsilon^{cr}$). The CDP will compute the plastic strain using Equation (3.15) (Abaqus documentation, 2020).

$$\varepsilon^{pl} = \varepsilon^{cr} - \left(\frac{d_t}{1 - d_t} \right) \left(\frac{\sigma_t}{E_0} \right) \quad (3.15)$$

The following procedure is used in this study to generate the input data for Abaqus.

Step 1) The mechanical properties of the mortar are obtained from the literature. Some of the important properties are listed in Table 3.1.

Table 3.1 – Required input parameters for the CDP in Abaqus

Parameter	Description
ρ	Mass density [kg/m ³]
E_0	Young's modulus [MPa]
ν	Poisson's ratio
ψ	Dilation angle [°]
ϵ	Eccentricity
f_{bo}/f_{co}	The ratio of initial biaxial compressive yield stress to the initial uniaxial compressive yield stress
K_c	The ratio of the second stress invariant on the tensile meridian to the compressive meridian at the initial yield
f_t	Tensile strength [MPa]
G_f	Fracture energy [N/mm]

Step 2) The total strain ε^{tot} is defined as an interval between zero and ε_f , and the damage parameter d_t is calculated by using Equation (3.9). ε_f is obtained from Equation (3.13).

Step 3) Following the Hillerborg energy approach with a linear reduction in the stress (Jankowiak & Lodygowski, 2005), the post failure stress for every point in the interval is calculated by:

$$\sigma_t = (1 - d_t)f_t \quad (3.16)$$

Step 4) The elastic and cracking strains are computed by:

$$\varepsilon_0^{el} = \frac{\sigma_t}{E_0} \quad (3.17)$$

$$\varepsilon^{cr} = \varepsilon^{tot} - \varepsilon_0^{el} \quad (3.18)$$

Step 5) The tabular form of $\sigma_t - \varepsilon^{cr}$ is provided for the CDP in Abaqus (Figure 3.6.a).

Step 6) The tabular form of $d_t - \varepsilon^{cr}$ is provided for the sub-option in the CDP (Figure 3.6.b).

	Yield Stress	Cracking Strain
1	4.5	0
2	3.52	5E-05
3	2.89	0.0001
4	2.45	0.00015
5	2.12	0.0002
6	1.87	0.00025
7	1.67	0.0003
8	1.51	0.00035

a) Tabular $\sigma_t - \varepsilon^{cr}$ input

	Damage Parameter	Cracking Strain
1	0	0
2	0.22	5E-05
3	0.36	0.0001
4	0.46	0.00015
5	0.53	0.0002
6	0.58	0.00025
7	0.63	0.0003
8	0.66	0.00035
9	0.69	0.0004
10	0.72	0.00045
11	0.74	0.0005
12	0.76	0.00055
13	0.77	0.0006
14	0.79	0.00065
15	0.8	0.0007
16	0.81	0.00075
17	0.82	0.0008
18	0.83	0.00085
19	0.84	0.0009
20	0.89	0.0014
21	0.92	0.0019

b) Tabular $d_t - \varepsilon^{cr}$ input

Figure 3.6 – Tabular inputs for modelling tensile behavior by the CDP in Abaqus Property module

Following the above procedure, Microsoft Excel is used in this study to create the tabular inputs. Nevertheless, the procedure can also be programmed in Octave.

3.3 Non-local formulation of the damage model

The uniaxial tension test of the bar in Figure 3.3 demonstrated that the numerical results obtained with the local damage model suffered from sensitivity to the discretization. It was explained how the length of the damaged zone localized into one element and consequently became dependent on the mesh size. The Hillerborg energy approach was presented as a remedy. It was discussed that focusing on the required energy for opening a crack could reduce mesh sensitivity.

(Jirásek, 2004) proposes a different method for preventing the localization of damage. In this method, the damage parameter at a certain point in the model cannot depend solely on the strain at that point. It rather depends on the strain distribution in the neighborhood of the point under consideration. Therefore, the damage parameter is determined based on the weighted average of strain in the neighborhood of the point.

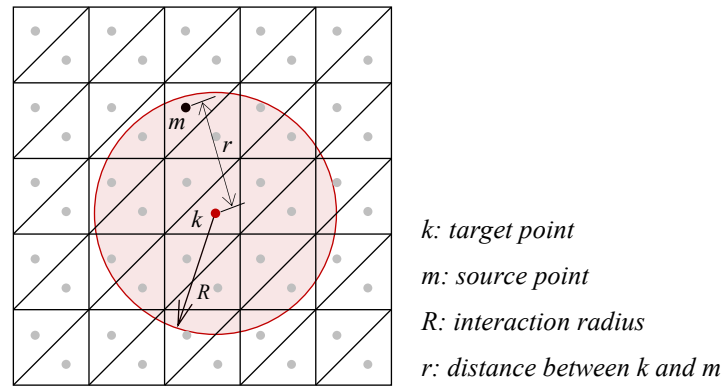


Figure 3.7 – Weighted averaging scheme

Figure 3.7 shows a discretized material domain. Suppose that one integration point is assigned to each finite element and the stress at a target point k is to be evaluated. A neighborhood with radius R is defined around the target point k (the red circle in Figure 3.7). This neighborhood and its radius are called the interaction zone and the interaction radius, respectively. The distance between the target point k and a point such as m inside the interaction zone is computed. This distance is shown by r in Figure 3.7. (Jirásek, 2004) determines the weight factor for the source point m as a function of r defined by:

$$\alpha_0(r) = \begin{cases} \left(1 - \frac{r^2}{R^2}\right)^2 & 0 \leq r \leq R \\ 0 & R \leq r \end{cases} \quad (3.19)$$

$\alpha_0(r)$ is computed for all integration points inside the interaction zone, and it will be averaged by Equation (3.20).

$$\alpha(k, m_i) = \frac{\alpha_0(\|k - m_i\|)}{\sum_{i=0}^{N_{IP}} \alpha_0(\|k - m_i\|)} \quad (3.20)$$

In the above equation, $\|k - m_i\|$ is the distance r . Assuming N_{IP} number of integration points inside the interaction zone, the denominator is the sum of the weight factors computed for each of them. $\alpha(k, m)$ is calculated for all points inside the interaction zone.

The weighted average strain at the target point k can be calculated by:

$$\bar{\varepsilon}(k) = \sum_{i=0}^{N_{IP}} \alpha(k, m_i) \cdot \varepsilon(m_i) \quad (3.21)$$

$\varepsilon(m_i)$ is the local strain at the source point m_i . Combining Equations (3.7) and (3.21), the “non-local damage parameter” at the target point k can be determined:

$$\bar{D} = d(\bar{\varepsilon}(k)) \quad (3.22)$$

Finally, the constitutive law is obtained by the substitution of \bar{D} for D in Equation (3.6).

$$\sigma = (1 - \bar{D})E\varepsilon \quad (3.23)$$

It is important to note that ε in Equation (3.23) is still the local strain. It is the damage parameter that is evaluated from the non-local strain, not the stress (Jirásek, 2004).

Implementation in Abaqus

A comparison between Equations (3.6) and (3.23) proves that the constitutive equation remains in principle unchanged. Therefore, the numerical implementation of the non-local damage model is relatively simple. All that is needed, is the computation of the weighted average strain and the evaluation of the damage parameter based on it (Jirásek, 2004).

Abaqus User Subroutines can be written as C, C++, or Fortran code to apply a particular procedure or an additional computation to the analysis of the model. UMAT is one of the available user subroutines that can be used to define the mechanical constitutive behavior of a material. It updates the stress at the end of the increment for which it is called. However, the use of UMAT and other user subroutines requires considerable expertise, and it should be done with great care (Abaqus documentation, 2020).

In this thesis, Abaqus user subroutines are not used. Instead, the non-local formulation of the damage model is programmed in Octave as a post-analysis procedure that processes the output of a general static analysis of the FEM model. Nevertheless, the developed algorithm can be applied to Abaqus user subroutine too. The developed procedure is described here.

The FEM model of the material specimen is created in Abaqus and a general static analysis is executed. The coordinates of the integration points in the cartesian system, as well as the volume, the strain, and the

stress for every integration point in the material domain are obtained from the general static analysis. These outputs can be exported from the Report Field Output window in Abaqus (Figure 3.8).

Visualization module: Report menu > Field output...

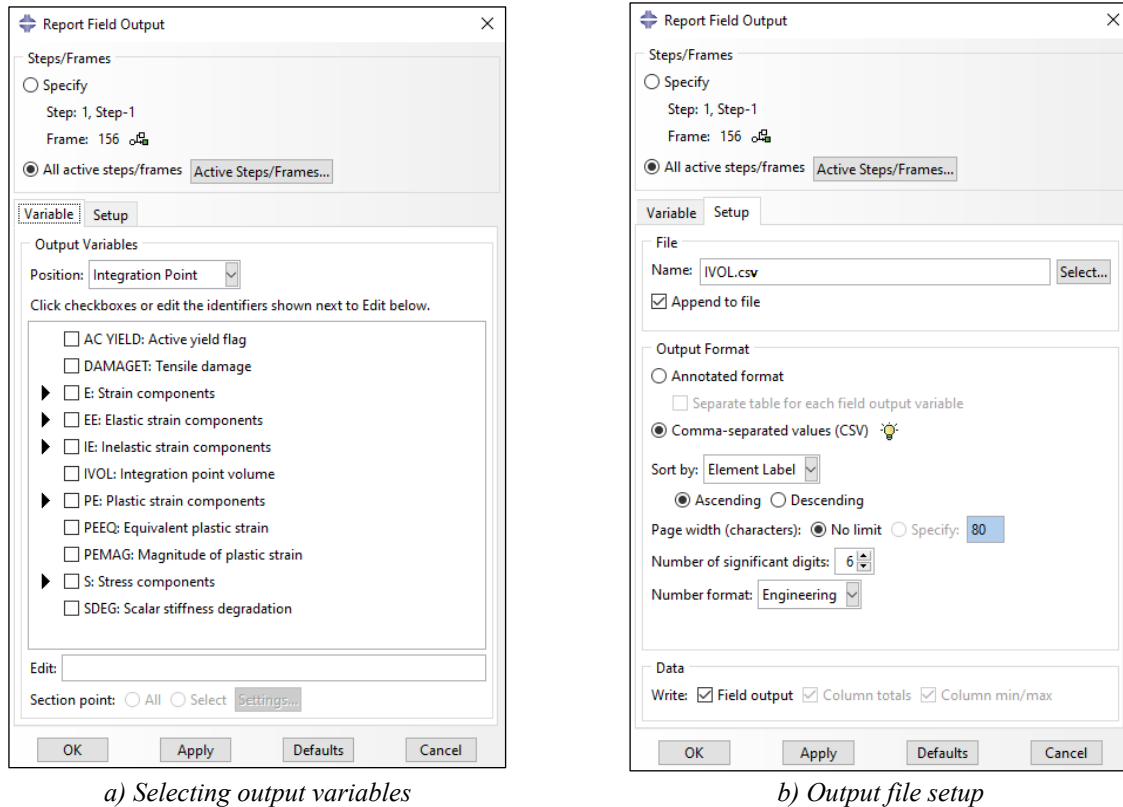


Figure 3.8 – Exporting the output from Report Field Output window in Abaqus Visualization module

Every field output is exported as an individual file in CSV format with a file name shown in Table 3.2. The user can choose the principal strain and stress in any direction. 22-direction is presented here as an example. Depending on the number of elements in the FEM model, it may take several minutes to export the output files.

Table 3.2 – Assigning name to the output files

Output file name	Description
IVOL.csv	Integration point volume and coordinates
E22.csv	Principle strain in 22 direction
S22.csv	Principle stress in 22 direction

The step-by-step procedure to compute the non-local strain and the damage parameter is as follows:

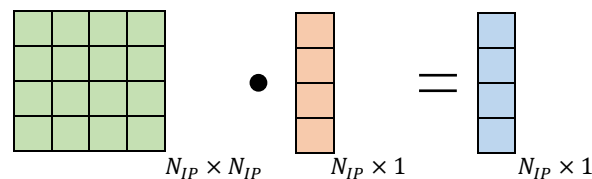
Step 1) The integration points are chosen one-by-one as the target point. The distance between the target point and all integration points, including the target point itself, is computed by Equations (3.24). Then,

the weight factor is obtained by Equations (3.19) and (3.20). Considering N_{IP} numbers of integration points in the material domain, the weight factors are stored in an $N_{IP} \times N_{IP}$ matrix.

$$r = \sqrt{(x_k - x_m)^2 + (y_k - y_m)^2 + (z_k - z_m)^2} \quad (3.24)$$

x , y and z are the cartesian coordinates of the points, subscript k and m corresponds to the target and source points, respectively.

Step 2) The non-local strain at every integration point is calculated by Equation (3.21). At this stage, the local strain is stored in a vector and the weight factors are kept in a matrix. Therefore, matrix multiplication is used as illustrated below.



$$[\alpha(k, m)] \cdot \{\epsilon(m)\} = \{\bar{\epsilon}(k)\}$$

Figure 3.9 – Computation of non-local strain by matrix multiplication

Step 3) The vector of non-local strain is given to Equation (3.9) as an input, and the nonlocal damage parameter is returned and stored in a vector. The stress at every integration point is calculated by Equation (3.16) using the nonlocal damage parameter.

Step 4) The homogenized stress and strain are computed, and they are exported in tab-delimited text files.

Every step in the above procedure has been programmed in Octave as a separate function, and they have been compiled in one script. The homogenization scheme in step 4 is discussed in section 3.5.

The computation of r in step 1 is the longest part of the entire procedure. Because the distance of every integration point to all other integration points should be calculated. This is necessary because the weight factor in Equation (3.19) is a function of the distance between the target and the source points. Additionally, the distance r should be calculated to determine whether an integration point falls in the interaction zone around the target point (Figure 3.7). Therefore, the number of times that Equation (3.24) should be called, is equal to the total number of integration points to the power of 2. For instance, in a material domain with 1 000 integration points, Equation (3.24) would be called 1 000 000 times! To reduce the computation time of step 1, the distance r should be calculated only between the points that are inside the interaction zone, not for the entire domain. This can be achieved by adopting a “cutting procedure” as illustrated in Figure 3.10.

For the target point under consideration, the cutting procedure determines two cutting planes in every cartesian direction of the material domain (Figure 3.10.a to c). The perpendicular distance between the

target point and every cutting plane is equal to the interaction radius R . The material domain is cut by these planes resulting in a reduced cubical domain (Figure 3.10.d). The size of the reduced domain is $2R \times 2R \times 2R$ and the target point k is at its centroid. The interaction zone is the inscribed sphere in this cube, and the distance r is calculated only for the integration points inside the reduced domain.

When the distance between the target point and the boundaries of the material domain is smaller than the interaction radius, the cutting plane will be outside the domain. To avoid generating such a cutting plane, the boundaries of the material domains are considered as the lower and upper limits for the coordinate of the cutting plane.

In Table 3.3, the computation time of the algorithm with the cutting procedure is compared with the same algorithm without the cutting procedure. It can be seen that employing the cutting procedure can reduce the computation time significantly.

Table 3.3 – Computation time with and without the cutting procedure

Model	Total no. of integration points	Computation time*	
		Without the cutting procedure	With the cutting procedure
1	2214	265 sec	53 sec
2	11,338	10,365 sec	4,464 sec

*CPU: Intel i7-7500U @ 3.5 GHz Dual core; RAM: 12 GB @ 1066 MHz

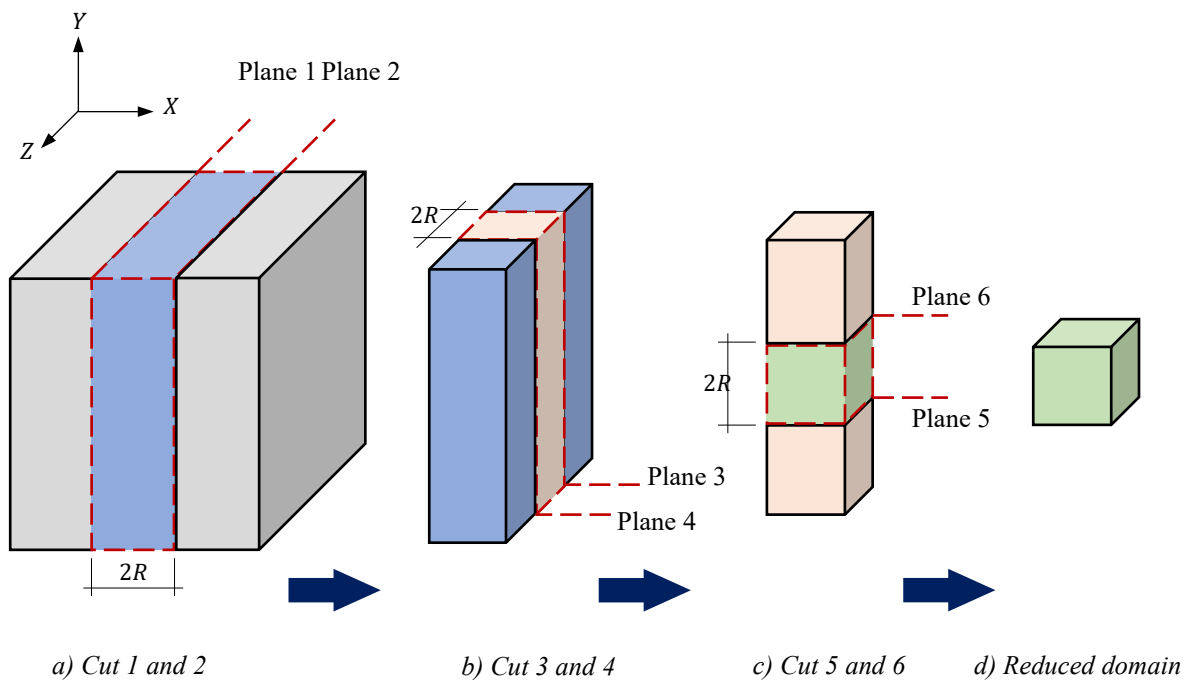


Figure 3.10 – The cutting procedure for reducing the domain size

3.4 Modeling the ITZ

The Interfacial Transition Zone in the micromodel of concrete were reviewed in section 2.2. In the present study, the ITZ is modeled as a cohesive layer between the mortar and the aggregate. The formulations of the constitutive law and the damage model are presented in this section.

The constitutive equation for the cohesive interface is expressed by the traction-separation relationship. In a 3D cohesive model, the nominal traction vector has three components: one normal traction t_n , and two tangential tractions t_s and t_t . Every traction component corresponds to the separation in the same plane denoted by δ_n , δ_s and δ_t . The traction-separation relationship has two distinct phases: (i) the linear elastic phase with full integrity of the surfaces in contact, (ii) the softening phase when the bond between the surfaces gradually loses integrity [(López, Carol, & Aguado, 2008), (Wang, Zhang, & Jivkov, 2016)].

The traction is related to the separation with the penalty stiffness shown by K_n , K_s and K_t for each component. Considering the cohesive model in Figure 3.11.a, the penalty stiffness is the initial stiffness that is used to hold the top and bottom elements together in the linear elastic range; for instance, at point 1, where separation is still smaller than the critical separation. The softening branch (post-failure behavior) may also be considered to be linear. Figure 3.11.a illustrates the traction-separation behavior of the material in single-mode I. Similarly, the traction-separation behavior in single-mode II or III is shown in Figure 3.11.b. The traction in mode III is in the transverse direction of mode II. For a 3D cohesive model with a mixed-mode failure, the constitutive relationship can be formulated in matrix form and expressed by Equation (3.25) (Camanho & Dávila, 2002).

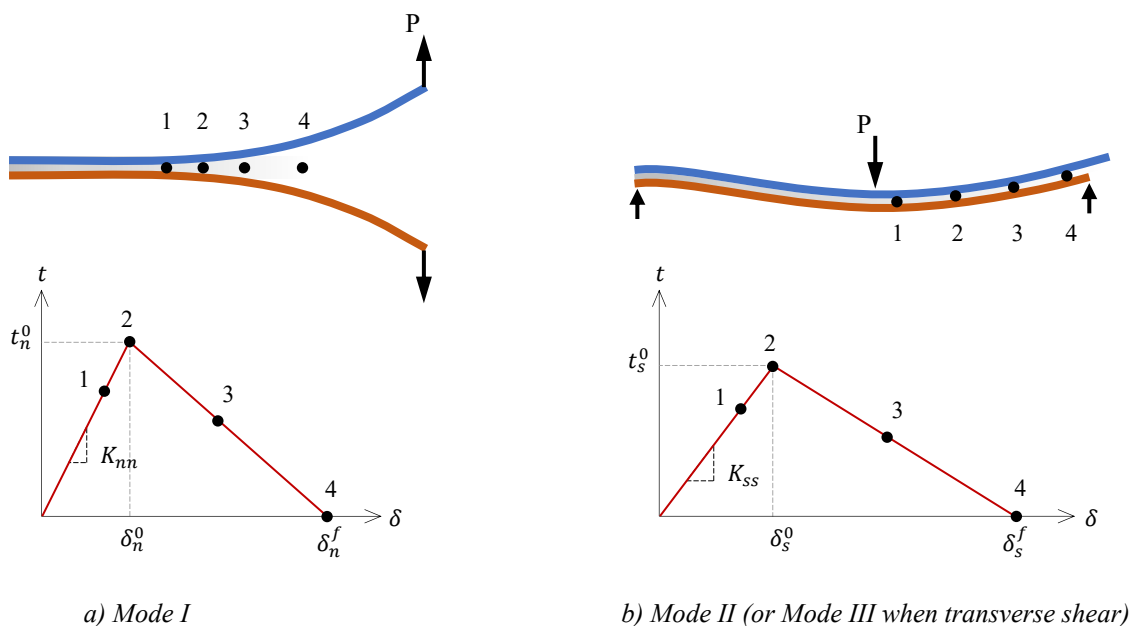


Figure 3.11 – Single-mode constitutive behavior for a cohesive interface by (Camanho & Dávila, 2002)

$$\{t\} = \begin{Bmatrix} t_n \\ t_s \\ t_t \end{Bmatrix} = \begin{bmatrix} K_{nn} & K_{ns} & K_{nt} \\ K_{sn} & K_{ss} & K_{st} \\ K_{tn} & K_{ts} & K_{tt} \end{bmatrix} \cdot \begin{Bmatrix} \delta_n \\ \delta_s \\ \delta_t \end{Bmatrix} \quad (3.25)$$

Damage in the cohesive element initiates when the traction becomes larger than the material strength. The initiation criteria can be formulated either by the linear Equation (3.26) as reported by (Camanho & Dávila, 2002), or by the quadratic Equation (3.27) as used by (Wang, Zhang, & Jivkov, 2016).

$$\max \left\{ \frac{t_n}{t_n^0}, \frac{t_s}{t_s^0}, \frac{t_t}{t_t^0} \right\} = 1 \quad (3.26)$$

$$\left\{ \frac{t_n}{t_n^0} \right\}^2 + \left\{ \frac{t_s}{t_s^0} \right\}^2 + \left\{ \frac{t_t}{t_t^0} \right\}^2 = 1 \quad (3.27)$$

t_n^0 , t_s^0 , and t_t^0 are the material strength in the corresponding plane. In this study, Equation (3.26) is considered for the damage initiation in the ITZ model.

(Camanho & Dávila, 2002) expands the Hillerborg energy approach (section 3.2) to the fracture in the cohesive element and shows that the area under the traction-separation diagram in every mode is equal to the fracture energy in that mode.

$$\int_0^{\delta_n^f} t_n \cdot d\delta_n = G_n^C \quad (\text{single-mode I}) \quad (3.28)$$

$$\int_0^{\delta_s^f} t_s \cdot d\delta_s = G_s^C \quad (\text{single-mode II}) \quad (3.29)$$

$$\int_0^{\delta_t^f} t_t \cdot d\delta_t = G_t^C \quad (\text{single-mode III}) \quad (3.30)$$

The maximum or fracture separation is then calculated by:

$$\delta_n^f = \frac{2G_n^C}{t_n^0} \quad (3.31)$$

$$\delta_s^f = \frac{2G_s^C}{t_s^0} \quad (3.32)$$

$$\delta_t^f = \frac{2G_t^C}{t_t^0} \quad (3.33)$$

(Camanho & Dávila, 2002) proposes Equation (3.34) for the damage evolution in the mixed-mode failure.

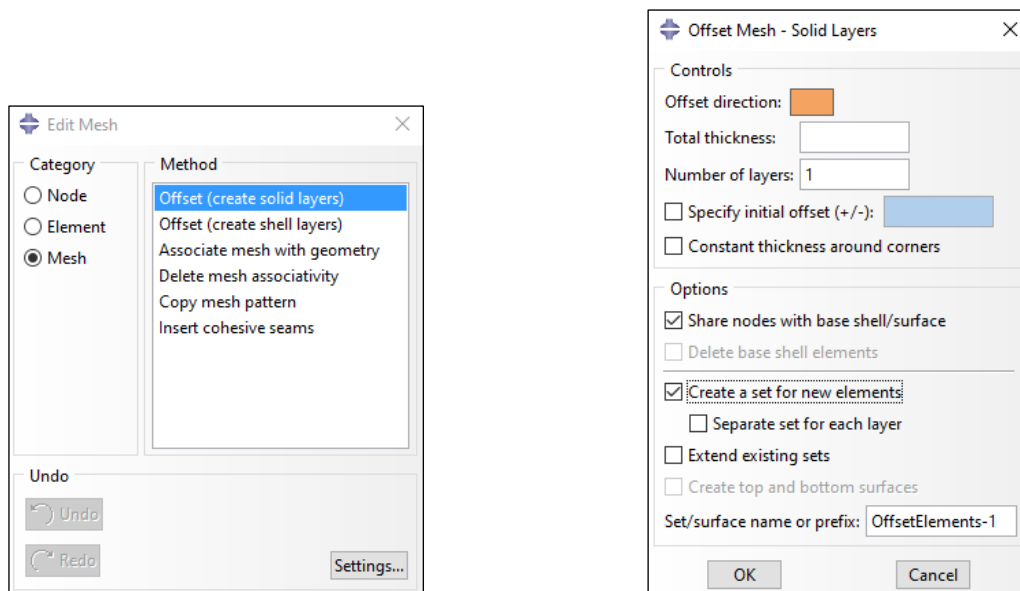
$$\left\{ \frac{G_n}{G_n^C} \right\}^2 + \left\{ \frac{G_s}{G_s^C} \right\}^2 + \left\{ \frac{G_t}{G_t^C} \right\}^2 = 1 \quad (3.34)$$

A comprehensive study on the mixed-mode failure based on the fracture energy can be found in (Benzeggagh & Kenane, 1996). The damage evolution can also be formulated with a linear or exponential function as described by (Wang, Zhang, & Jivkov, 2016). The energy-based evolution formulated by Equation (3.34) is used in this study.

Implementation in Abaqus

One of the standard methods for modeling the ITZ is to insert a cohesive element between the aggregate and the mortar matrix after the mesh has been generated for them. The inserted cohesive element has common nodes with the surrounding material, it is much thinner than them, or its thickness is considered to be zero [(Wang, Zhang, & Jivkov, 2016), (Kim & Abu Al-Rub, 2011), (López, Carol, & Aguado, 2008), (Caballero, López, & Carol, 2006)].

Abaqus mesh generator is capable of inserting a thin element between the materials. The Solid Offset Mesh tool in the Edit Mesh toolset can create an offset of an existing mesh (Figure 3.12). The generated offset is a layer of hexahedral or wedge elements that share nodes with the surrounding mesh, and it is embedded in them. The user can define the thickness of the layer, and it should be much thinner than the surrounding material. The tool can create an offset mesh only from 3D elements. Therefore, it cannot be used in 2D modeling. The cohesive element type should be assigned to the generated layer (Abaqus documentation, 2020).



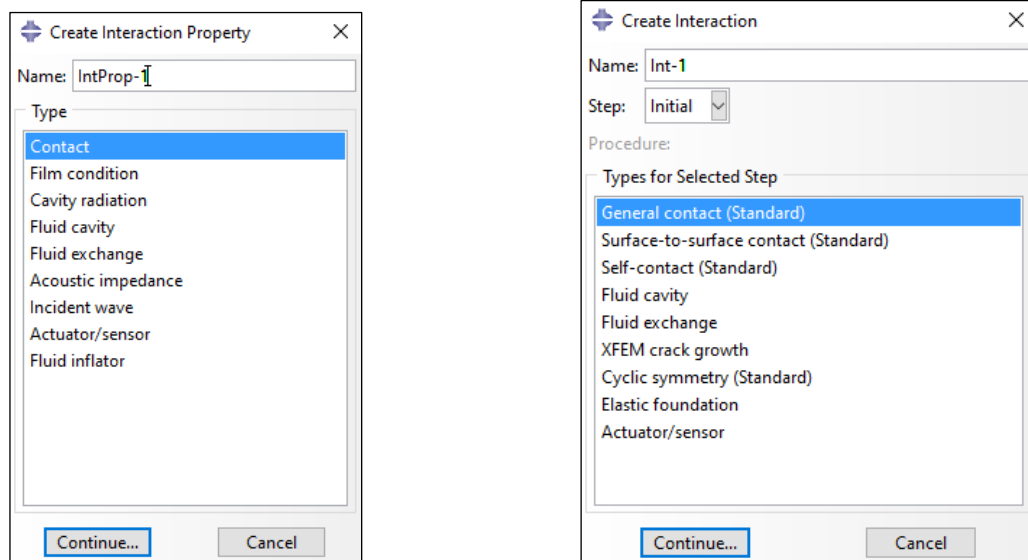
a) Step 1: Mesh module: Mesh menu > Edit...

b) Step 2: The solid offset mesh toolbox

Figure 3.12 – Generating an offset layer of mesh in Abaqus Mesh module

Besides generating the offset layer, Abaqus offers a second approach for modeling a layer with a negligible thickness between two solid materials. The Contact Cohesive Behavior (CCB) can be used to model a bonded interface, with or without the damage criteria. The mechanical properties and the damage criteria

are defined in the Create Interaction Property toolbox by the user. In this approach, the ITZ is modeled by assigning the General Contact to the surfaces of the aggregate and the mortar matrix that are in contact (Figure 3.13).



a) Step 1: Interaction menu > Property > Create...

b) Step 2: Interaction menu > Create...

Figure 3.13 – Modeling Contact Cohesive Behavior in Abaqus Interaction module

The author faced difficulties with creating an offset layer between the mortar and the aggregate. The close distance between the aggregate particles would lead to generating distorted mesh elements. In some cases, the nodes were so close that Abaqus would report zero volume for the corresponding elements. The random structure of the aggregate, and a relatively large number of particles, would turn the manual repair of the generated mesh into a tedious task.

In contrast to the offset layer, the second approach does not suffer from the zero-volume-element. The only difficulty with the CCB was observed when there was an overclosure or a gap between two surfaces in contact (Figure 3.14). This happens in particular when two surfaces are curved. The user can resolve these imperfections by using the Contact Initialization tool (Figure 3.15). Abaqus adjusts the surface nodes following the user settings in the contact initialization toolbox. By assigning the Slave Surface type to one of the surfaces in contact, the user can specify the preferred surface for node adjustment. The adjustment of the nodes is strain-free and it does not induce stress in the material (Abaqus documentation, 2020). The CCB with the strain-free adjustment is used in this study for creating the ITZ model.

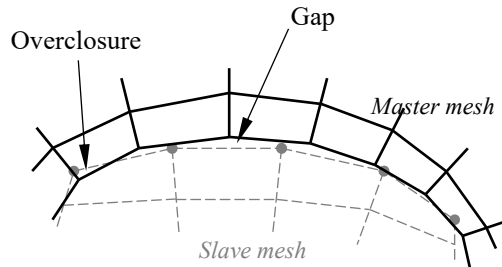
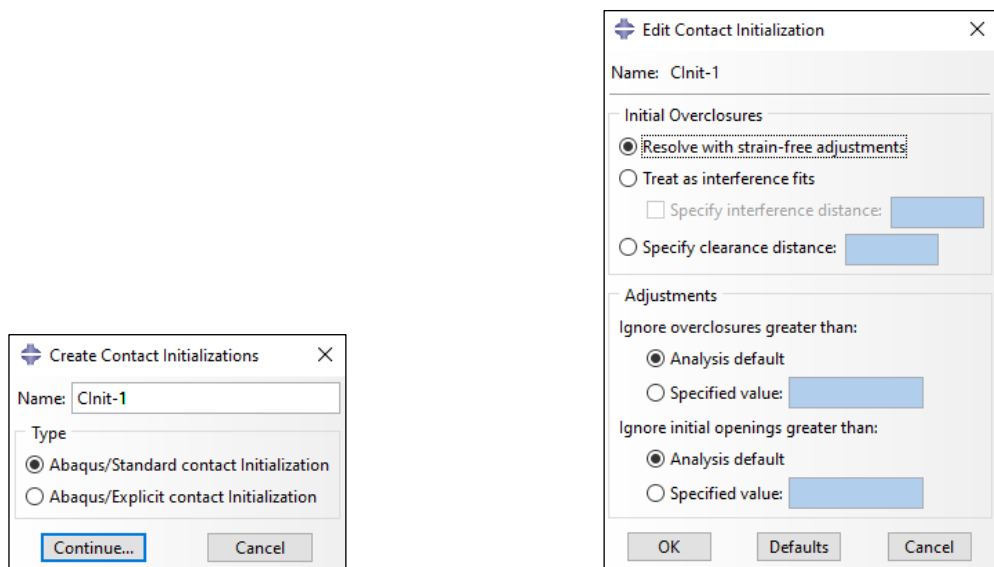


Figure 3.14 – Gap and overclosure between two surfaces in contact



a) Step 1: Interaction menu > Property > Create...

b) Step 2: Interaction menu > Create...

Figure 3.15 – The contact initialization tool in Abaqus Interaction module

3.5 Homogenization

The role of a homogenization scheme in the multiscale modeling was described in section 2.4.1. It was highlighted that the homogenized stress is the spatial average of the microscopic stress (Feyel, 2003). As illustrated in Figure 2.6, the homogenized stress is transmitted from the lower scale to the higher scale (from the RVE to the macromodel).

In this study, three variations of the spatial averaging for homogenization of the stress and strain are programmed in Octave. These three variations were presented in detail and discussed in section 2.4.1. A summary of the methods together with the algorithm used in the programming are provided here.

Averaging over the entire volume

This method is known as the standard averaging technique (Gitman, Askes, & Sluys, 2007). Stress and strain are averaged over the entire volume of the RVE and all constituents in the micromodel are included in the averaging. Considering N_{IP} number of integration points in the entire volume, the homogenized stress and strain are computed by:

$$\sigma_h = \frac{\sum_{i=0}^{N_{IP}} \sigma_i \cdot V_i}{\sum_{i=0}^{N_{IP}} V_i} \quad (3.35)$$

$$\varepsilon_h = \frac{\sum_{i=0}^{N_{IP}} \varepsilon_i \cdot V_i}{\sum_{i=0}^{N_{IP}} V_i} \quad (3.36)$$

This approach is referred to as the ‘‘Gitman averaging technique’’ in the present study.

Averaging over the undamaged volume

Stress and strain are averaged over the undamaged volume of the RVE and all constituents in the micromodel are included in the averaging (Belytschko, Loehnert, & Son, 2008). Considering K_{IP} number of integration points in the undamaged volume, the homogenized stress and strain are formulated by:

$$\sigma_h = \frac{\sum_{i=0}^{K_{IP}} \sigma_i \cdot V_i^{ud}}{\sum_{i=0}^{K_{IP}} V_i^{ud}} \quad (3.37)$$

$$\varepsilon_h = \frac{\sum_{i=0}^{K_{IP}} \varepsilon_i \cdot V_i^{ud}}{\sum_{i=0}^{K_{IP}} V_i^{ud}} \quad (3.38)$$

This approach is referred to as the ‘‘Belytschko averaging technique’’ in the present study.

Averaging over the damaged volume

Stress and strain are averaged over the damaged volume of the RVE and all constituents in the micromodel are included in the averaging (Nguyen V. P., Valls, Stroeven, & Sluys, 2010). Considering M_{IP} number of integration points in the model, the homogenized stress and strain are formulated by:

$$\sigma_h = \frac{\sum_{i=0}^{M_{IP}} \sigma_i \cdot V_i^d}{\sum_{i=0}^{M_{IP}} V_i^d} \quad (3.39)$$

$$\varepsilon_h = \frac{\sum_{i=0}^{M_{IP}} \varepsilon_i \cdot V_i^d}{\sum_{i=0}^{M_{IP}} V_i^d} \quad (3.40)$$

This approach is referred to as the “Nguyen averaging technique” in the present study.

The difference between the three averaging techniques is the volume over which the stress and strain are averaged. For easy programming in Octave, Equations (3.35) to (3.40) are replaced with the new Equations (3.41) and (3.42). In the new set of equations, the Volume Participation Factor α_v is defined as a two-condition function in terms of d_t , and it is computed by Equation (3.43).

$$\sigma_h = \frac{\sum_{i=0}^{N_{IP}} \sigma_i \cdot (\alpha_{v,i} \cdot V_i)}{\sum_{i=0}^{N_{IP}} (\alpha_{v,i} \cdot V_i)} \quad (3.41)$$

$$\varepsilon_h = \frac{\sum_{i=0}^{N_{IP}} \varepsilon_i \cdot (\alpha_{v,i} \cdot V_i)}{\sum_{i=0}^{N_{IP}} (\alpha_{v,i} \cdot V_i)} \quad (3.42)$$

$$\alpha_{v,i} = \begin{cases} \begin{matrix} \text{Condition 1} & \text{Condition 2} \\ \text{Gitman} & 1 \\ \text{Belytschko} & \begin{cases} 1 & d_{t,i} \leq d_t^{crit} \\ 0 & d_t^{crit} < d_{t,i} \end{cases} \\ \text{Nguyen} & \begin{cases} 0 & d_{t,i} \leq d_t^{crit} \\ 1 & d_t^{crit} < d_{t,i} \end{cases} \end{matrix} \end{cases} \quad (3.43)$$

The user can define the boundary between the damaged and undamaged volume by assigning a value to d_t^{crit} in Equation (3.43). This feature allows consideration of some minor damage in the undamaged volume. The theoretical value for d_t^{crit} is zero, which represents a volume without any damage, but this may not resemble the reality because minor cracks start to develop far below the failure stress [(Zaitsev & Wittman, 1981), (Sluys, 1992)]. In this study, d_t^{crit} is assumed to be 5%.

Homogenization is a post-analysis procedure. It requires the volume, the stress, and the strain of every integration point as inputs. Additionally, the damage degree of every integration point should also be provided as it is required in the computation of $\alpha_{v,i}$ by Equation (3.43).

After completion of the FEM analysis in Abaqus, the required variables are exported for every integration point as an individual file in CSV format with the file name shown in Table 3.4. These variables are obtained from the field output window similar to section 3.3. DMGT contains the damage parameter d_t for every integration point. The user can choose the principal strain and stress in any direction. 22-direction is presented here as an example. Depending on the number of elements in the FEM model, it may take several minutes to export the output files.

Table 3.4 – Assigning name to the output files

Output file name	Description
DMGT.csv	Tensile damage parameter
IVOL.csv	Integration point volume and coordinates
E22.csv	Principle strain in 22 direction
S22.csv	Principle stress in 22 direction

The step-by-step procedure to compute homogenized stress and strain is as follows:

Step 1) The damage parameter at every integration point is given to Equation (3.43) as an input, and the volume participation coefficient $\alpha_{v,i}$ is computed and stored in an $N_{IP} \times 3$ matrix. Each column in this matrix stores $\alpha_{v,i}$ for one of the averaging techniques.

$$[\alpha_{v,i}]_{N_{IP} \times 3} = \{i = 1, 2, \dots, N_{IP}: d_{t,i} \rightarrow \alpha_{v,i} \text{ for every ave. tech.}\} \quad (3.44)$$

Step 2) For every integration point, the product of the volume multiplied by $\alpha_{v,i}$ is computed and stored in a separate column of an $N_{IP} \times 3$ matrix. Every column in this matrix corresponds to one averaging technique. The sum of the elements in every column is calculated and stored as a floating number. This floating sum is the denominator in Equations (3.41) and (3.42).

$$[\alpha_{v,i} \cdot V_i]_{N_{IP} \times 3} = \{i = 1, 2, \dots, N_{IP}: V_i \rightarrow \alpha_{v,i} \cdot V_i \text{ for every ave. tech.}\} \quad (3.45)$$

$$\left[\sum \alpha_{v,i} \cdot V_i \right]_{3 \times 1} = \{j = 1, 2, 3: \sum [\alpha_{v,i} \cdot V_i] (\text{all rows}, j)\} \quad (3.46)$$

Step 3) The stress at every integration point is multiplied by the corresponding elements in the resulted matrix in Equation (3.45). The products are stored in an $N_{IP} \times 3$ matrix. Every column in this matrix corresponds to one averaging technique. The sum of the elements in every column is stored as a floating number. This floating sum is the numerator in Equations (3.41) and (3.42).

$$[\sigma_i \cdot \alpha_{v,i} \cdot V_i]_{N_{IP} \times 3} = \{i = 1, 2, \dots, N_{IP}: \sigma_i \rightarrow \sigma_i \cdot \alpha_{v,i} \cdot V_i \text{ for every ave. tech.}\} \quad (3.47)$$

$$\left[\sum \sigma_i \cdot \alpha_{v,i} \cdot V_i \right]_{3 \times 1} = \{j = 1, 2, 3: \sum [\sigma_i \cdot \alpha_{v,i} \cdot V_i] (\text{all rows}, j)\} \quad (3.48)$$

Step 4) For every averaging technique, the floating sum computed by Equation (3.48) is divided by the corresponding sum in Equation (3.46). The product is the homogenized stress, and it is exported in a tab-delimited text file.

For simplicity, the formulation in the above procedure was expressed only for stress. In the written program, steps 3 and 4 are executed for stress and strain simultaneously, and the program exports the homogenized stress and strain together. The above procedure is also illustrated in Figure 3.16.

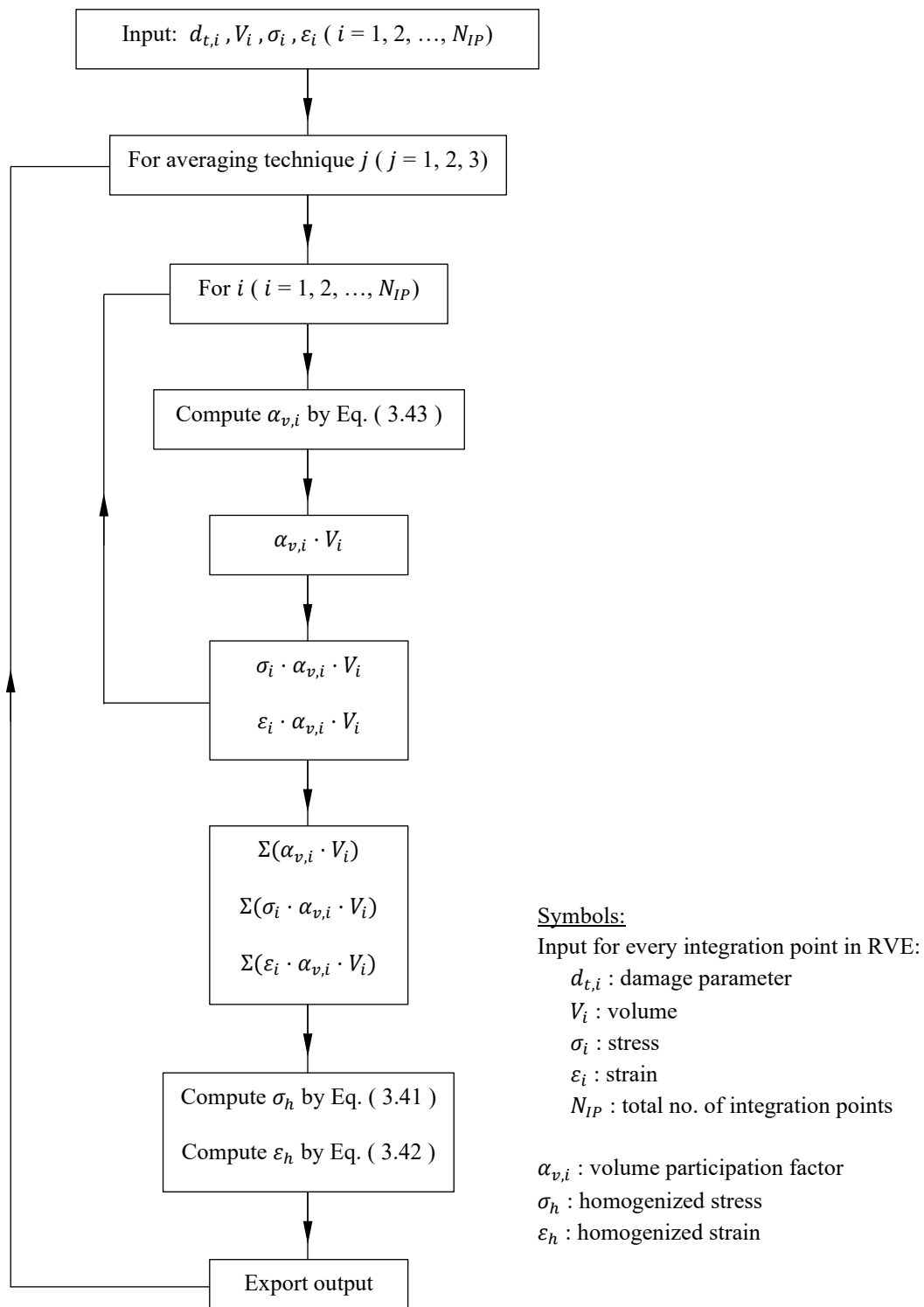


Figure 3.16 – The developed algorithm for homogenization

4 Numerical Examples

4.1 Introduction

A generic model for the post-failure behavior of concrete was developed and presented in chapter 3. It was described how gradual degradation of the material integrity was incorporated in the model by introducing the damage parameter into the constitutive equation. Formulations for the local and non-local damage models were presented and the implementation of them in Abaqus was explained. An algorithm was programmed in Octave to be used alongside Abaqus for computation of the non-local damage. Finally, three averaging techniques were scripted in Octave for homogenization of stress and strain.

In this chapter, the developed model is used in numerical examples to demonstrate its application and to investigate its capabilities and weaknesses.

The mechanical properties of the constituents are collected from the literature. The material properties remain unchanged in all the numerical examples unless otherwise specified. Table 4.2 provides the list of the parameters, the corresponding references, and the observed range in the cited literature for this study.

Following the procedure described on page 44 and 45, the stress-strain and the damage-strain diagrams are generated for the mortar. The curves are shown in Figure 4.1 and Figure 4.2. For better illustration of the curves, the upper bound of the total strain is limited to 0.007 in the figures. Tabular computation is also provided in Table 4.1. The highlighted columns in Table 4.1 are used as the input data for the CDP in Abaqus.

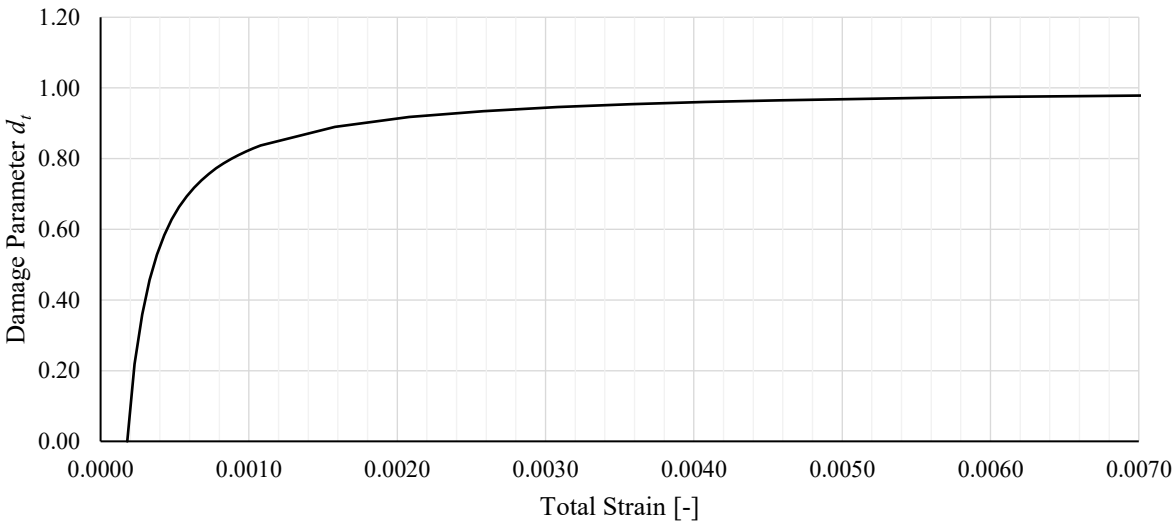


Figure 4.1 – The defined damage evolution in the mortar

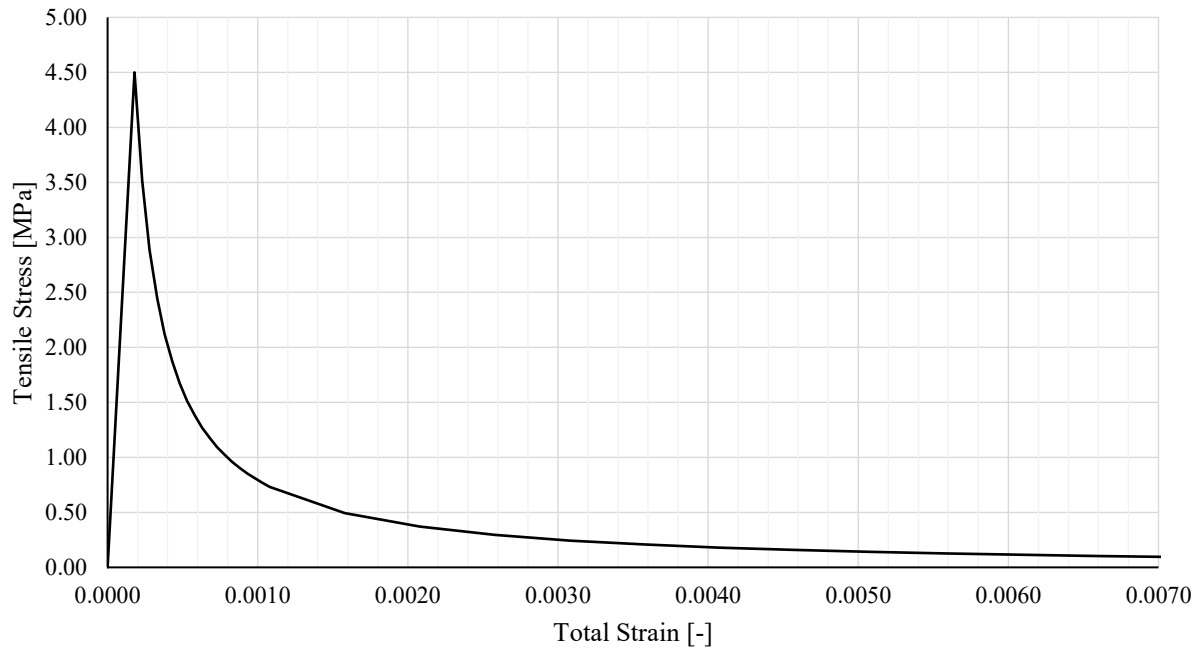


Figure 4.2 – The defined stress-strain behavior of the mortar under uniaxial tension

Table 4.1 – Computation of the inputs for modeling mortar damage with the CDP

ε^{tot}	d_t Eq. (3.9)	σ_t Eq. (3.16)	ε_0^{el} Eq. (3.17)	ε^{cr} Eq. (3.18)
0.00000	–	0.00		–
0.00018	0.00	4.50	0.000180	0.00000
0.00020	0.10	4.05	0.000162	0.000038
0.000225	0.20	3.60	0.000144	0.000081
0.00033	0.30	3.15	0.000126	0.0002
0.00030	0.40	2.70	0.000108	0.00019
0.00036	0.50	2.25	0.00009	0.00035
0.00045	0.60	1.80	0.000072	0.00038
0.00060	0.70	1.35	0.000054	0.00055
0.00088	0.80	0.90	0.000036	0.00084
0.00180	0.90	0.45	0.000018	0.00178
0.01300	0.99	0.045	0.00000186	0.01300
	CDP input	CDP input		CDP input

Table 4.2 – Material properties considered in the present study

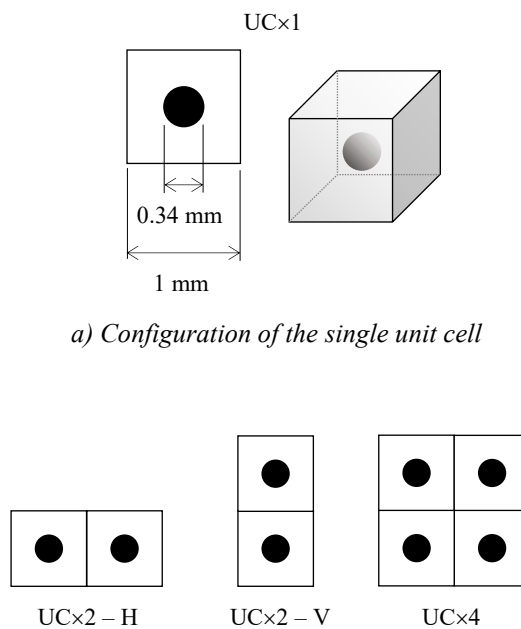
Constituent	Parameter			Reference	Range
Aggregate	ρ	2 600	kg/m ³	(Eckardt, 2009)	2 600 ~ 2 800
	E_0	30 000	MPa	(Gitman, Askes, & Sluys, 2007)	30 000 ~ 70 000
	ν	0.2			0.18 ~ 0.2
Mortar	ρ	2 000	kg/m ³	(Wang, Jivkov, Engelberg, & Li, 2018)	–
	E_0	25 000	MPa	(Gitman, Askes, & Sluys, 2007)	25000 ~ 35 000
	ν	0.2			0.18 ~ 0.2
	ψ	35	degree	(Wang, Jivkov, Engelberg, & Li, 2018)	31 ~ 35
	ϵ	0.1			–
	f_{bo}/f_{co}	1.16			–
	K_c	0.667			–
	f_t	4.5	MPa	(Eckardt, 2009)	4 ~ 4.9
	ϵ_t	0.00018		Computed by $\epsilon_t = E_0/f_t$	–
	G_f	0.3	MPa/mm	(Eckardt, 2009)	0.3 ~ 0.35
	β	1.7			–
	R	2	mm		–
	g_f	0.088	MPa/mm	Computed by Equation (3.13)	–
ϵ_f	0.04		Computed by $\epsilon_f = 2g_f/f_t$	–	
ITZ	thickness	0.25	mm	(Gitman, Askes, & Sluys, 2007)	0.1 ~ 1
	K_{nn}	100 000	MPa/mm	(Wang, Jivkov, Engelberg, & Li, 2018)	1000 ~ 100 000
	K_{ss}	100 000	MPa/mm		
	K_{tt}	100 000	MPa/mm		
	t_{nn}	2	MPa		
	t_{ss}	4	MPa		4 ~ 10
	t_{tt}	4	MPa		
	$G_{f,nn}$	0.01	N/mm		0.01 ~ 0.1
	$G_{f,ss}$	0.02	N/mm		0.02 ~ 0.3
	$G_{f,tt}$	0.02	N/mm		

4.2 Mesoscale unit cell under uniaxial tension

A single RVE composed of one or two particles is frequently used in the literature for a qualitative study of the damage model, the material inputs, and the overall formulations [(Nguyen, Stroeven, & Sluys, 2012), (Belytschko & Song, 2010), (Feyel, 2003)]. The simplicity of the model enables a clear demonstration of the material behavior, which helps to verify errors. For this purpose, a unit cell is used in this study to examine the developed model.

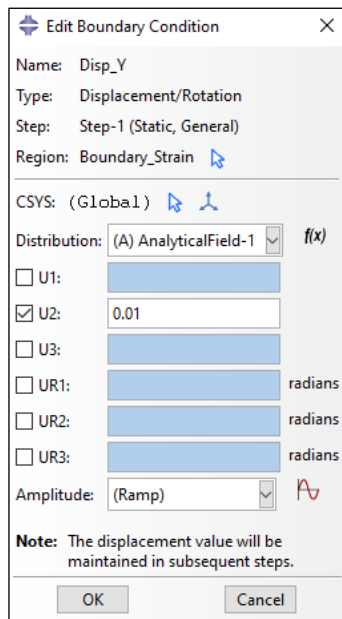
The “unit cell” is a cube with one particle at its centroid. The particle symbolizes the aggregate and the surrounding solid represents the mortar. The cube dimensions are $1 \times 1 \times 1$ mm, and the spherical particle has a diameter of 0.34 mm. The configuration of the unit cell is taken from (Belytschko & Song, 2010), and it is shown in Figure 4.3.a.

The uniaxial tension test of the unit cell is simulated in Abaqus. The test is strain-driven. A uniaxial strain is applied to the external surfaces of the unit cell. The “Boundary Condition” tool and the “Analytical Fields” function in Abaqus are used to define the applied strain (Figure 4.4). A mathematical function is defined in the Analytical Fields. The function computes the applied displacement by multiplying the input strain by the y-coordinate of the surface points. Abaqus begins the analysis with a zero strain. It gradually increases the strain at each step until the input strain is reached (Abaqus documentation, 2020).

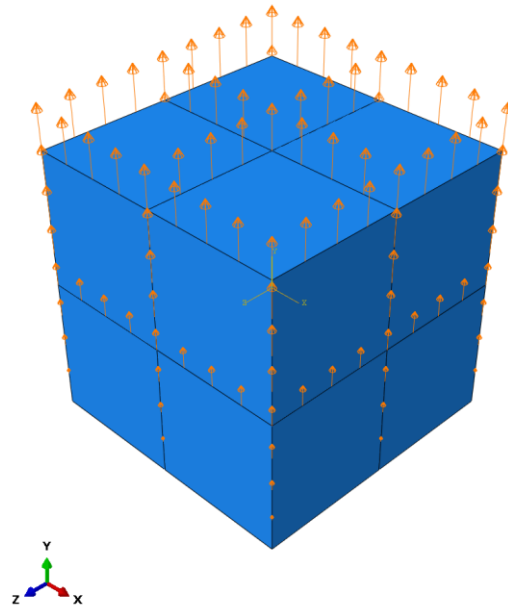


b) Three combinations of the unit cell (2D illustration)

Figure 4.3 – Illustration of the single and combined unit cell



a) Defining incremental strain



b) Applied strain to the unit cell

Figure 4.4 – Creating strain-driven uniaxial tension test of the unit cell in Abaqus Load module

The first assessment

In the first simulation, the single unit cell without the ITZ is considered (Figure 4.3.a). The Elimination of ITZ simplifies the model, and the model simplicity is beneficial for the evaluation of the analysis result. In the absence of ITZ, the bond between the particle and the mortar is considered to be completely rigid. The linear elastic behavior is assumed for the aggregate. The local damage model with the Hillerborg energy approach is considered for the nonlinear behavior of the mortar matrix (section 3.2). The model is discretized by 4-node linear tetrahedral elements. The largest mesh size is 0.1 mm. The FEM mesh consists of 11 300 elements approximately. The applied strain is equal to 0.01 (equal to $\varepsilon_f/4$). The standard averaging technique is used to homogenize the stress-strain at every increment.

Figure 4.5 compares the stress-strain diagram of one integration point in the mortar domain with the input curve. Two curves are in agreement except for the first part of the softening branch, where the integration point shows a slightly larger strain.

The homogenized stress-strain diagram of the unit cell is also provided in Figure 4.5. The curve shows larger stress than the input curve at the lower part of the softening branch. This is expected because the homogenized stress is the weighted average stress of the entire volume. The material points in the volume do not unload uniformly in the softening phase. For instance, the tensile stress is between 0.0 MPa and 1.5 MPa at 0.8% strain (Figure 4.6.c). The stress and damage distribution diagrams for two states of strain are provided in Figure 4.6.

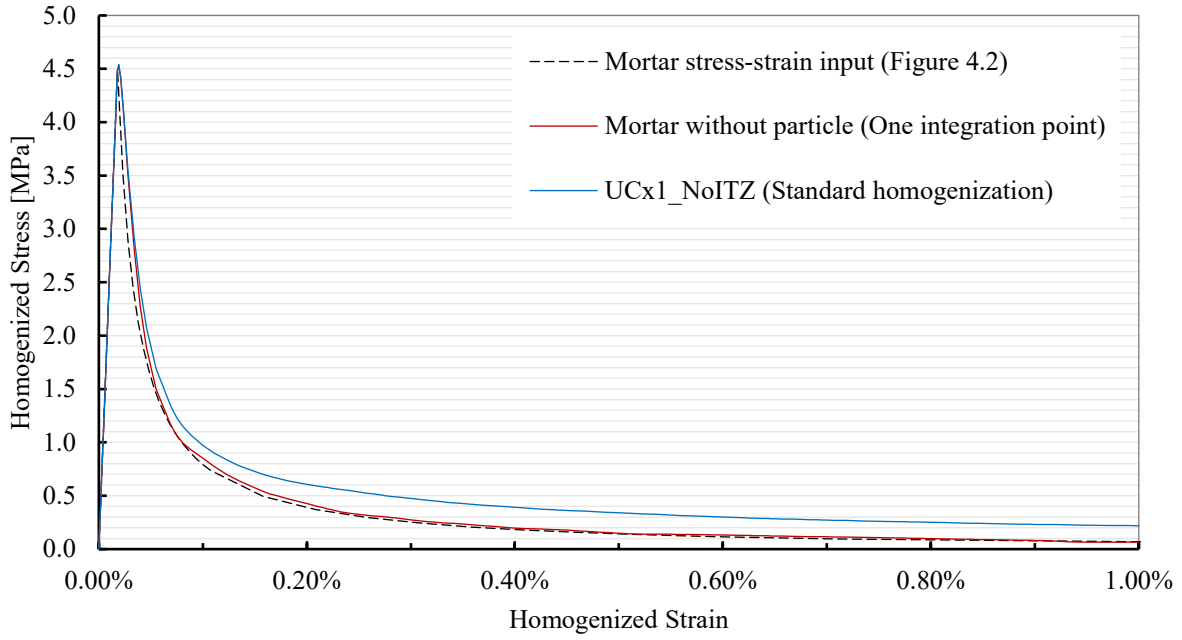


Figure 4.5 – Uniaxial tension test of single unit cell: output vs. input diagrams

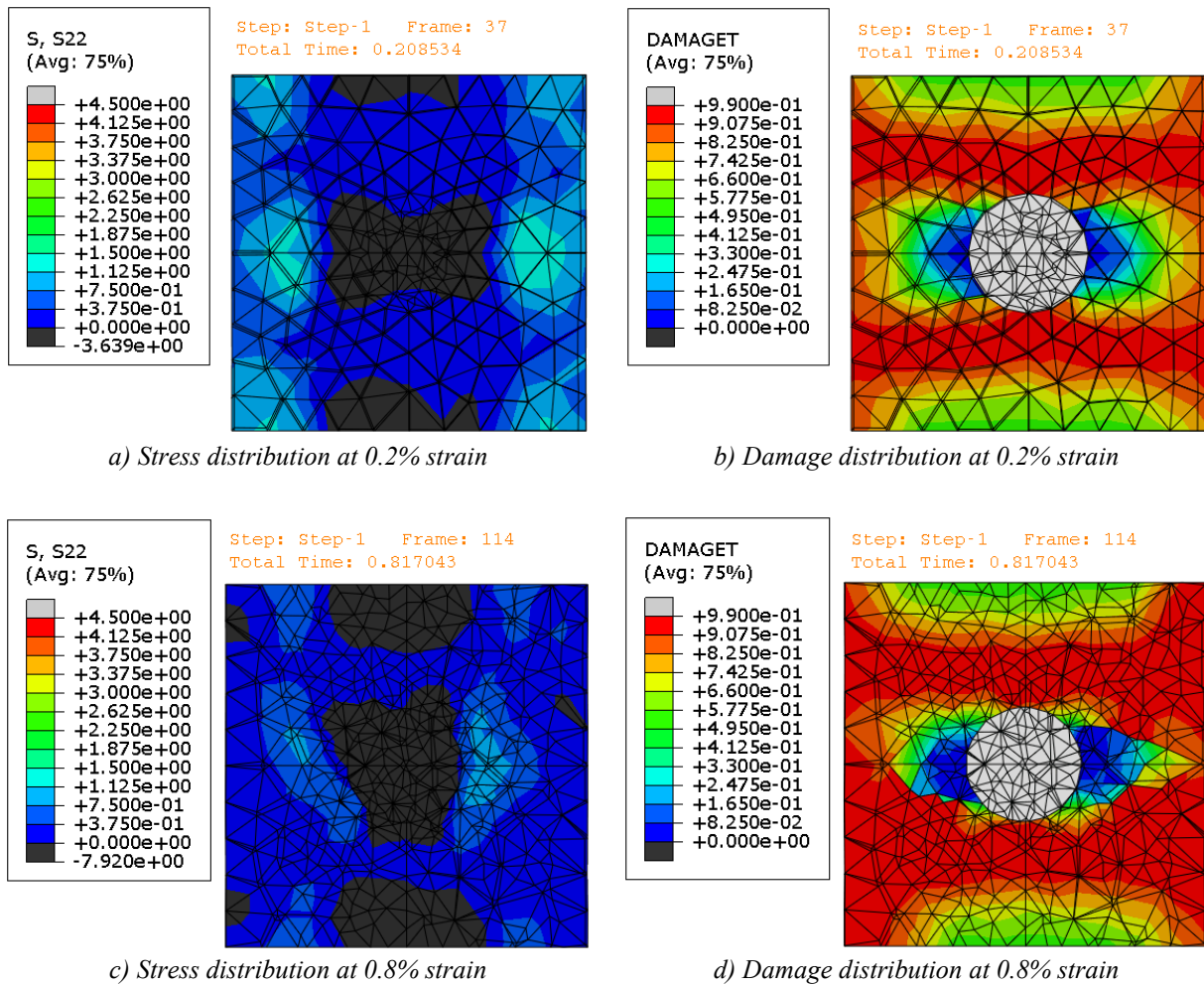


Figure 4.6 – Uniaxial tension test of single unit cell: stress and damage distribution at mid-section

Size effect

The uniaxial tension test is repeated with three combinations of the single unit cell. The goal is to investigate the influence of the model size on the result. The first two models are composed of two numbers of the unit cell coupled horizontally and vertically. The third model is formed by combining four numbers of the unit cell (Figure 4.3.b). The assumptions in the simulation of the single unit cells are kept unchanged, except for the applied strain. The applied strain is lowered to 0.001 to reduce computation time.

Figure 4.7 shows the stress-strain diagram of the combined unit cells. The difference between the curves is negligible. Therefore, the model size does not affect the material behavior in the uniaxial tension.

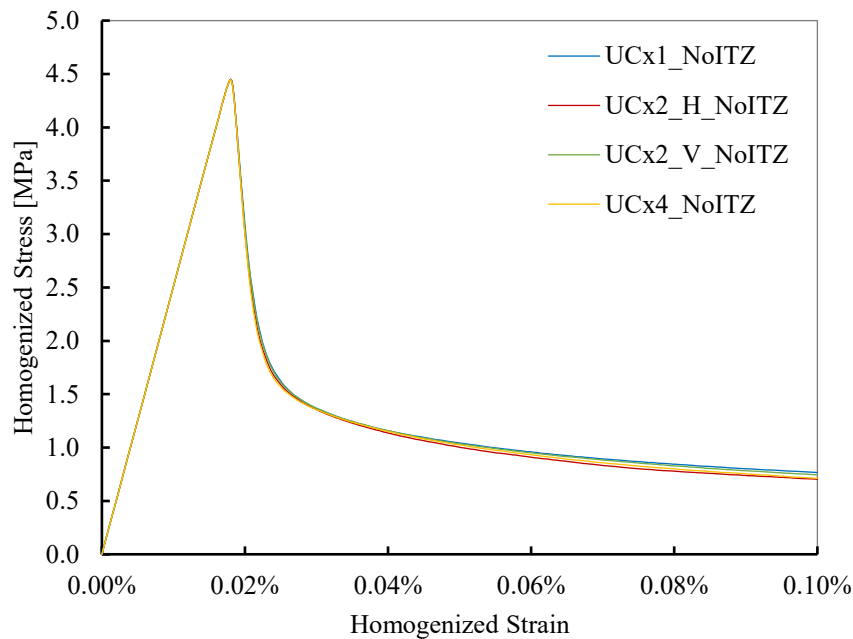


Figure 4.7 – Uniaxial tension test of combined unit cells: size effect

The impact of nonlinear ITZ

It is known that the ITZ reduces the tensile strength of concrete and results in lower peak stress in the stress-strain diagram [(Wang, Jivkov, Engelberg, & Li, 2018), (Huang, Yang, Ren, Liu, & Zhang, 2015), (Wang, Zhang, & Jivkov, 2016)]. To demonstrate the impact of the ITZ on material behavior, the nonlinear ITZ is added to the four models in Figure 4.3, and the simulation is repeated. The CCB with the strain-free adjustment is used for modeling the ITZ. The tensile behavior of ITZ is described with the traction separation law, and the damage evolution is energy-based (section 3.4). The assumptions for the aggregate and the mortar matrix remain unchanged.

The stress-strain diagram of every model is compared with the diagram of the same model without the ITZ (Figure 4.8 to Figure 4.11). The diagrams show lower peak stress for all four models with the nonlinear ITZ. However, the lower part of the softening branch exhibits an increase in the stress after adding the ITZ to the models. Four major material properties obtained from the curves are listed in Table 4.3.

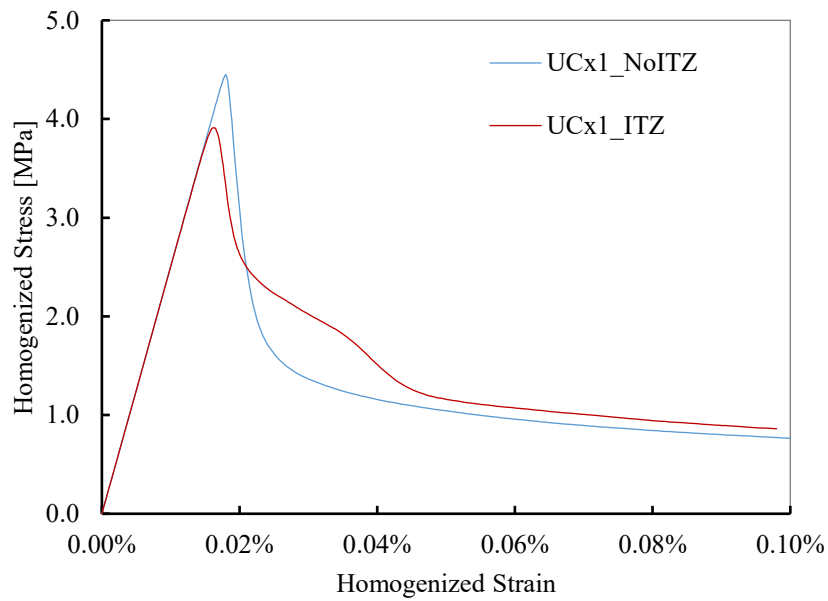


Figure 4.8 – Uniaxial tension test of single unit cell: with and without ITZ

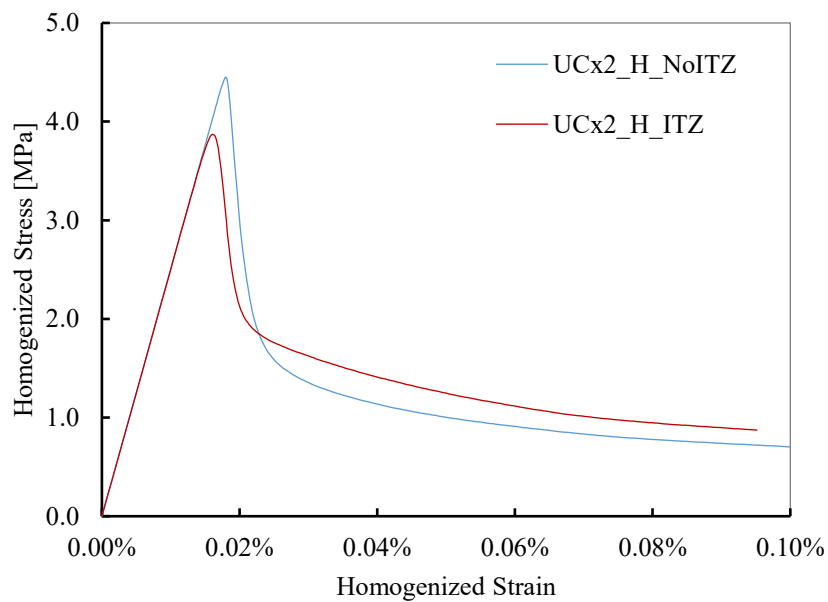


Figure 4.9 – Uniaxial tension test of horizontally coupled unit cells: with and without ITZ

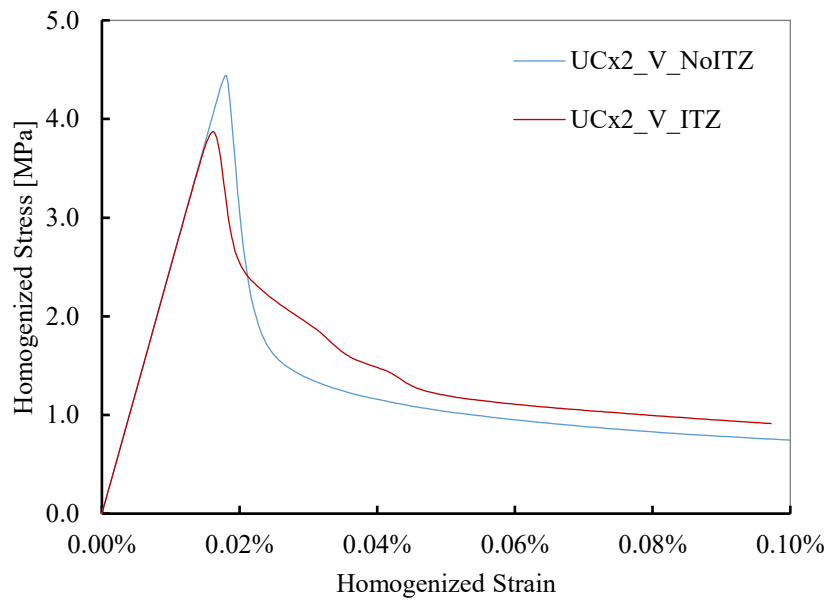


Figure 4.10 – Uniaxial tension test of vertically coupled unit cells: with and without ITZ

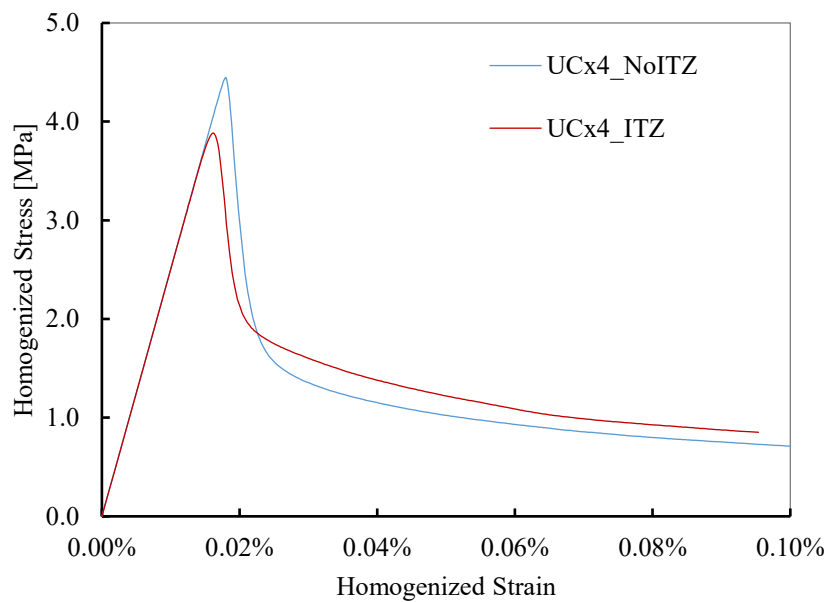


Figure 4.11 – Uniaxial tension test of 4 combined unit cells: with and without ITZ

Table 4.3 – Mechanical properties obtained from stress-strain diagrams

Model	a) Homogenized f_t			b) Homogenized ε_t		
	without ITZ [MPa]	with ITZ [MPa]	change after adding ITZ	without ITZ [-]	with ITZ [-]	change after adding ITZ
UCx1	4.45	3.91	-13.7%	0.00018	0.00016	-10.5%
UCx2_H	4.45	3.87	-15.0%	0.00018	0.00016	-12.4%
UCx2_V	4.44	3.87	-14.7%	0.00018	0.00016	-11.8%
UCx4	4.45	3.88	-14.5%	0.00018	0.00016	-11.6%
average	4.45	3.89	-14.5%	0.00018	0.00016	-11.6%
Model	c) Homogenized E_0			d) Area under the curve		
	without ITZ [MPa]	with ITZ [MPa]	change after adding ITZ	without ITZ	with ITZ	change after adding ITZ
UCx1	24710	24001	-3.0%	0.00134	0.00146	8.6%
UCx2_H	24734	24185	-2.3%	0.00130	0.00136	4.8%
UCx2_V	24631	24005	-2.6%	0.00133	0.00145	8.7%
UCx4	24698	24069	-2.6%	0.00131	0.00135	3.0%
average	24693	24065	-2.6%	0.00132	0.00141	6.3%

It was explained in section 3.2 that the fracture energy does not significantly change with the model size. The area under the stress-strain curve is associated with the fracture energy. A comparison between the models without the ITZ in Table 4.3(d) shows that the area does not notably deviate from the average area under the curve. A similar remark can be made when comparing the models with the ITZ. Therefore, the simulation acknowledges that the model size does not affect the fracture energy. (Eckardt, 2009) obtained a similar outcome when studying the size effect.

Comparison between the averaging techniques

An algorithm was developed in section 3.5 for three averaging techniques, namely Gitman (standard), Belytschko, and Nguyen (Figure 3.16). In this section, the stress-strain relationship of every model is homogenized using the three methods. A comparison between the homogenized diagrams is made to study how the averaging technique influences the result. The parameter d_t^{crit} in Equation (3.43) is set to 0.05 for this comparison, which means 5% damage is allowed in the undamaged domain. 5% damage counts for the microcracks that form in concrete before the peak stress [(Zaitsev & Wittman, 1981), (Sluys, 1992)]. The parameter d_t^{crit} does not influence the Gitman method.

Figure 4.12 to Figure 4.15 show the homogenized diagrams for the models without the ITZ, and Figure 4.16 to Figure 4.19 present the diagrams for the same models with the ITZ.

The first remark can be made about the Belytschko technique. The softening branch of the stress-strain curve vanishes in this method. The criterion for averaging is the cause of the vanished softening branch. The damaged volume is constantly excluded from the domain. Therefore, the remained integration points in the domain are still in the elastic branch, and they have not passed the peak stress. The stress-strain is

averaged over the remained points. Consequently, the homogenized stress-strain does not exhibit any branch for the damaged volume.

In contrast to the Belytschko technique, the Nguyen method excludes the undamaged volume from the material domain. Inevitably, stress-strain is constantly averaged over the damaged volume. In the simulation with the models without the ITZ, nonlinearity is governed by the mortar alone. Therefore, the homogenized curve coincides in most parts with the input curve for the mortar.

In models with the ITZ, nonlinearity is initiated by the ITZ, and it is controlled by the ITZ until the mortar fails. The Nguyen method captures this phenomenon well. The beginning part of the softening branch in Nguyen's curve (Figure 4.16 to Figure 4.19) shows the combined behavior of the mortar and ITZ in the nonlinear regime. There is a sudden change in the path of the softening branch in all curves, which resembles a sharp snap-back. The author is currently unable to provide any explanation for this phenomenon, and it requires further study in the future.

Belytschko and Nguyen averaging techniques were introduced in (Belytschko & Song, 2010) and (Nguyen V. P., Valls, Stroeven, & Sluys, 2010), respectively. Both articles provide numerical examples for the proposed methods, and the homogenized curves in the articles are not in agreement with the obtained diagrams in this study. This requires further investigation in the future.

The Gitman technique does not exclude any part of the material domain in the averaging procedure. As observed in Figure 4.6, the material points in the domain do not fail uniformly. Hence, there are elastic regions with a lower stress-strain magnitude as the softening starts. These regions are included in the averaging procedure. Therefore, the Gitman method results in a homogenized curve that falls below the input curve, as seen in Figure 4.12 to Figure 4.19.

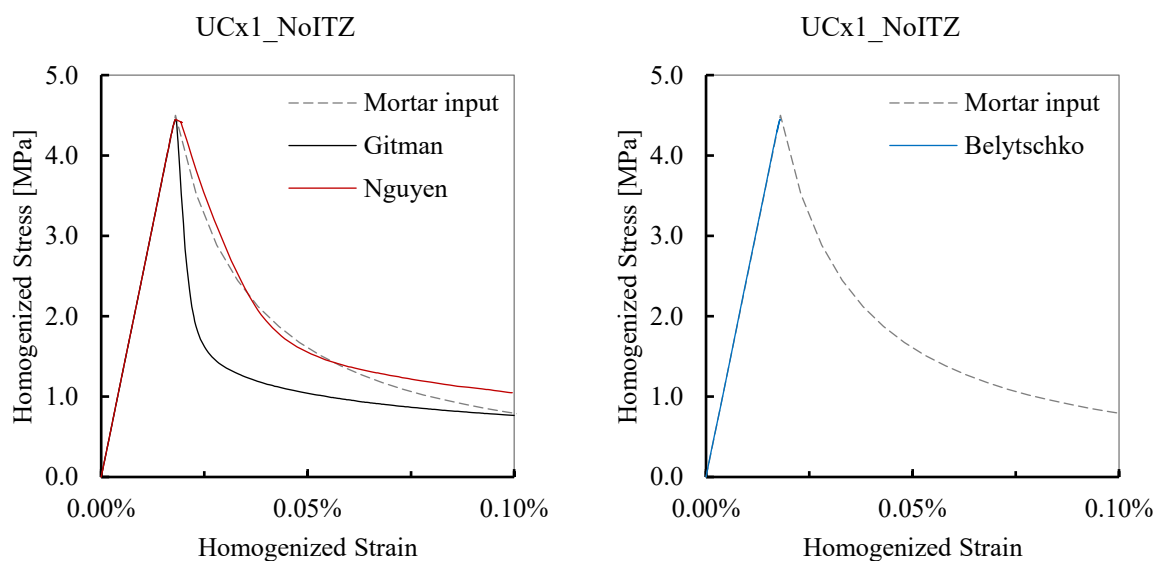


Figure 4.12 – Comparison between averaging techniques: single unit cell without ITZ

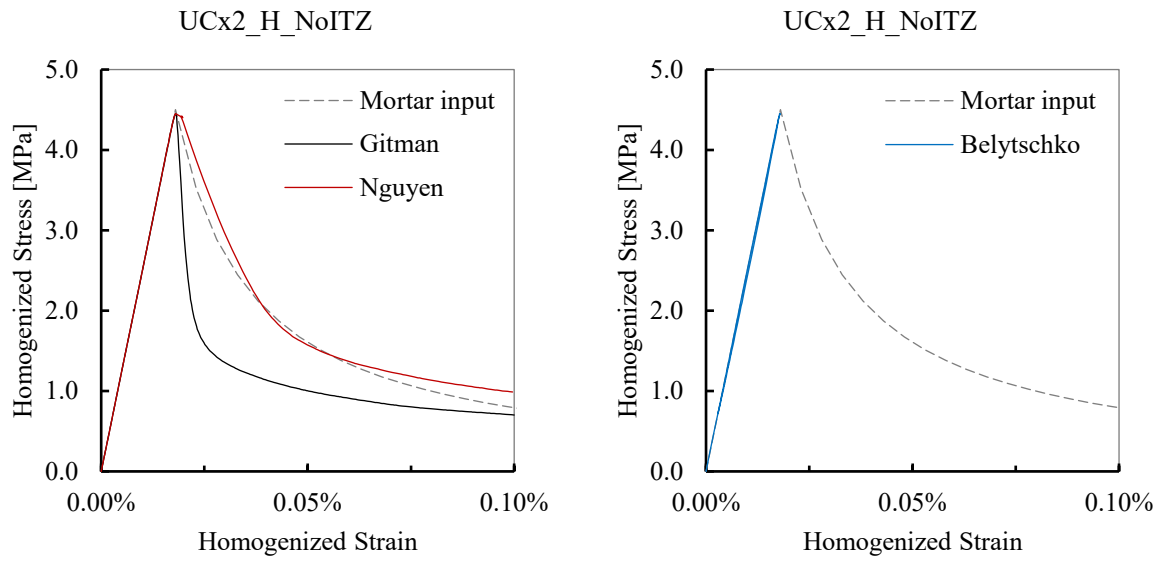


Figure 4.13 – Comparison between averaging techniques: horizontally coupled unit cells without ITZ

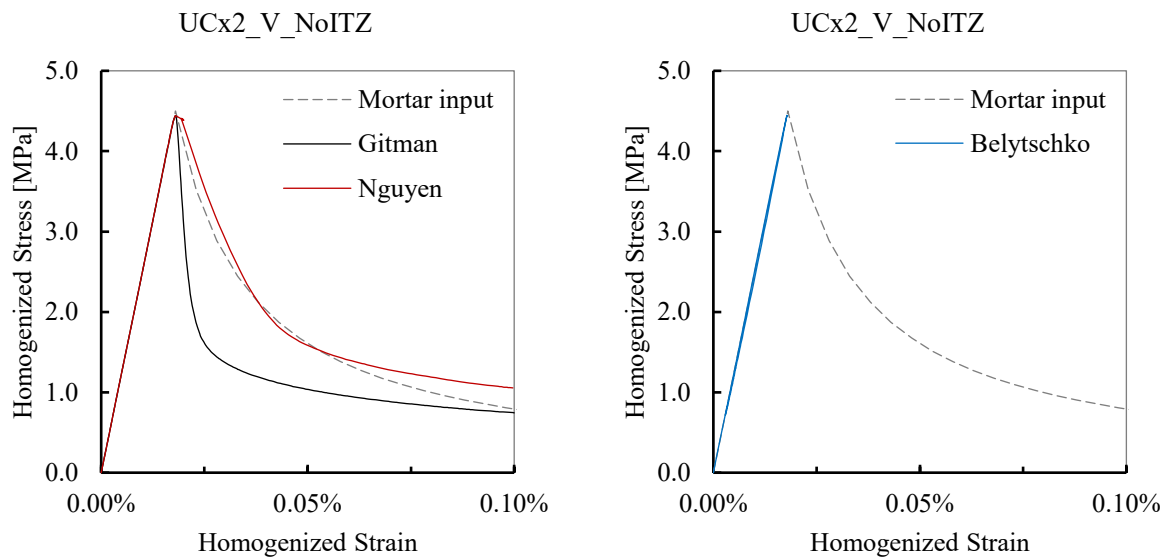


Figure 4.14 – Comparison between averaging techniques: vertically coupled unit cells without ITZ

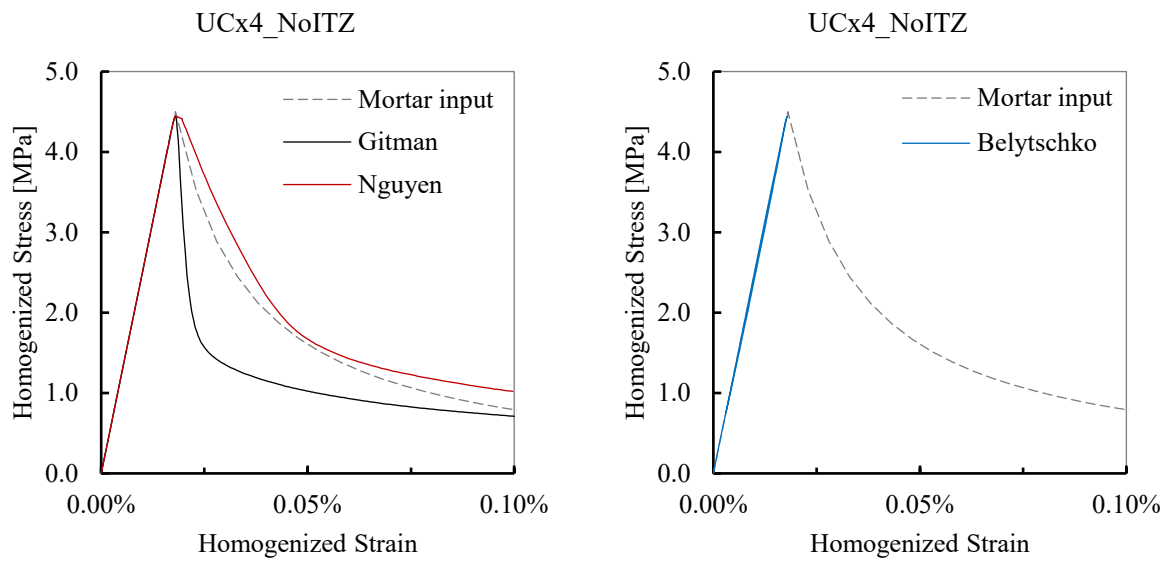


Figure 4.15 – Comparison between averaging techniques: 4 combined unit cells without ITZ

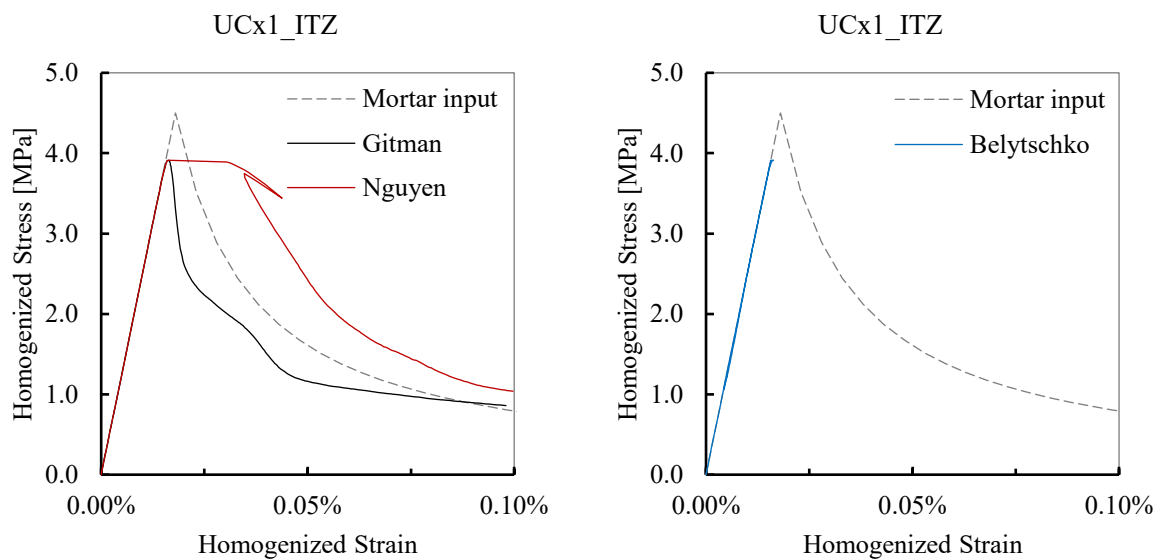


Figure 4.16 – Comparison between averaging techniques: single unit cell with ITZ

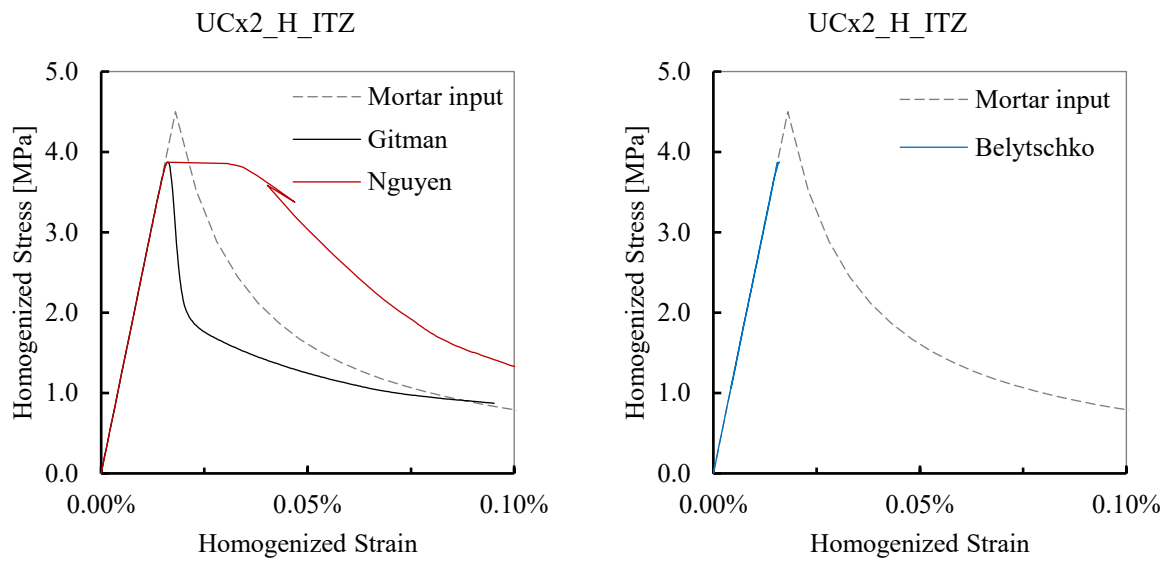


Figure 4.17 – Comparison between averaging techniques: horizontally coupled unit cells without ITZ

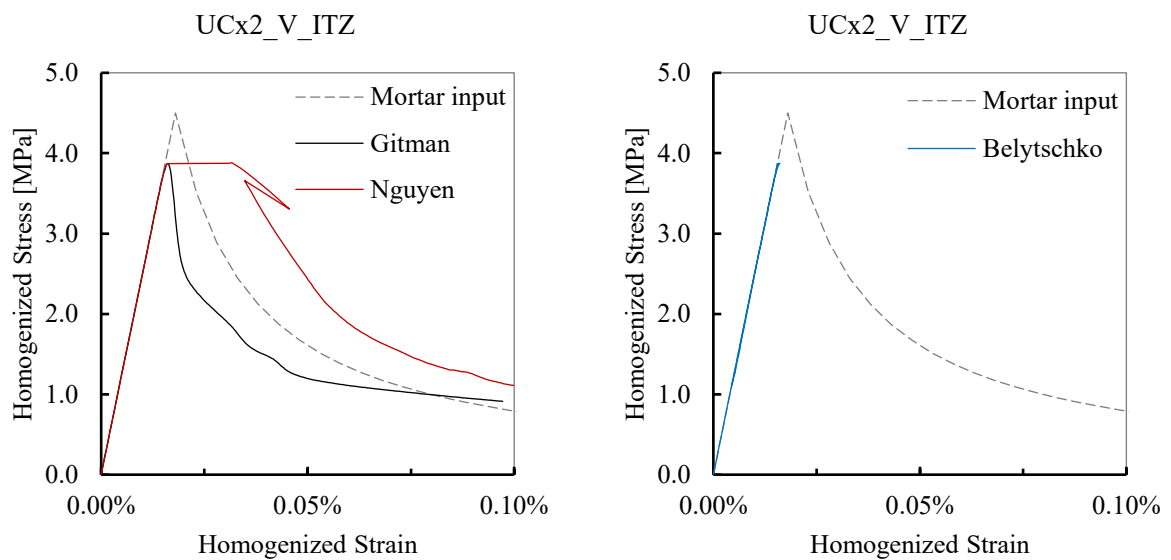


Figure 4.18 – Comparison between averaging techniques: vertically coupled unit cells without ITZ

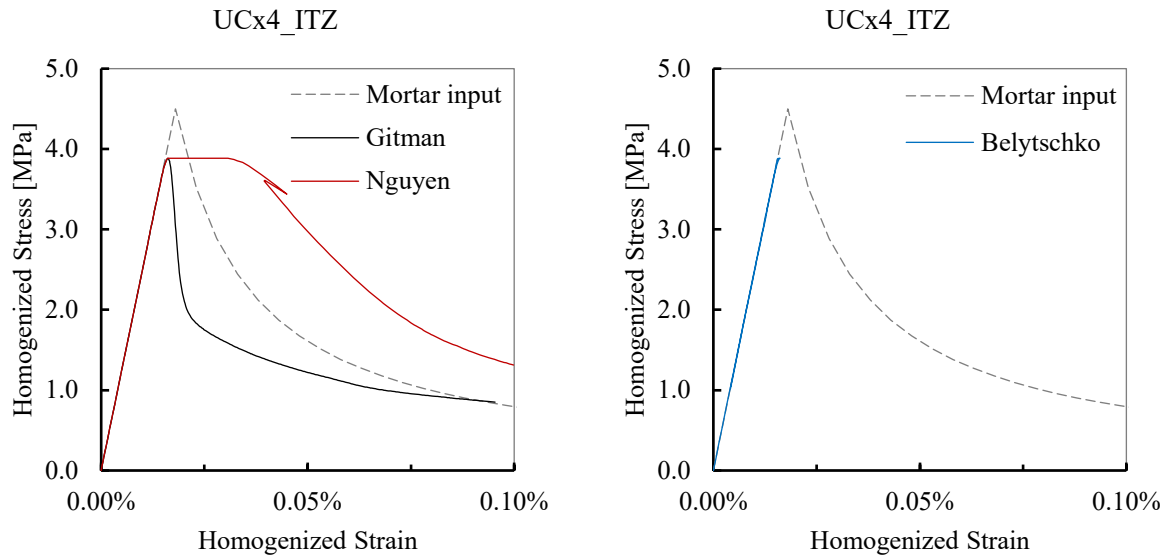


Figure 4.19 – Comparison between averaging techniques: 4 combined unit cells without ITZ

Mesh sensitivity in the local damage model

As specified in section 3.2, the Hillerborg energy approach is used in this study as a remedy for mesh sensitivity in the local damage model. The uniaxial tension test of the single unit cell without the ITZ is repeated in this section with various discretization. The goal is to demonstrate how well the energy-based formulation can decrease mesh sensitivity. The elimination of nonlinear ITZ in this simulation helps to reduce the computation time.

In the initial simulation, the largest mesh size was 0.1 mm, with approximately 11 300 tetrahedral elements in the FEM model. For a coarse mesh, the largest mesh size is changed to 0.2 mm, which results in 2 200 elements. For a fine mesh, the largest size is limited to 0.05 mm, which creates 58 800 number of elements (Table 4.4). The standard averaging technique is used for homogenization.

Table 4.4 – Variation in mesh size

Mesh	Max. size [mm]	No. of elements	Analysis time* [sec]
Coarse	0.20	2 200	41
Initial	0.10	11 300	253
Fine	0.05	58 800	2 831

*CPU: Intel i7-7500U @ 3.5 GHz Dual core; RAM: 12 GB @ 1066 MHz

Figure 4.20 shows the homogenized stress-strain diagrams of the models. The peak stress and the upper part of the softening branch do not vary with the mesh size. In contrast, the simulations with the local

damage in (Jirásek, 2004) exhibit a significant drop in the peak stress when reducing the mesh size. Therefore, an acceptable reduction in mesh sensitivity has been achieved.

The lower parts of the three curves deviate from each other. Nevertheless, only the coarse mesh exhibits a notable deviation. The difference between the fine and the initial mesh is negligible. In summary, the model reveals minor sensitivity to the mesh size.

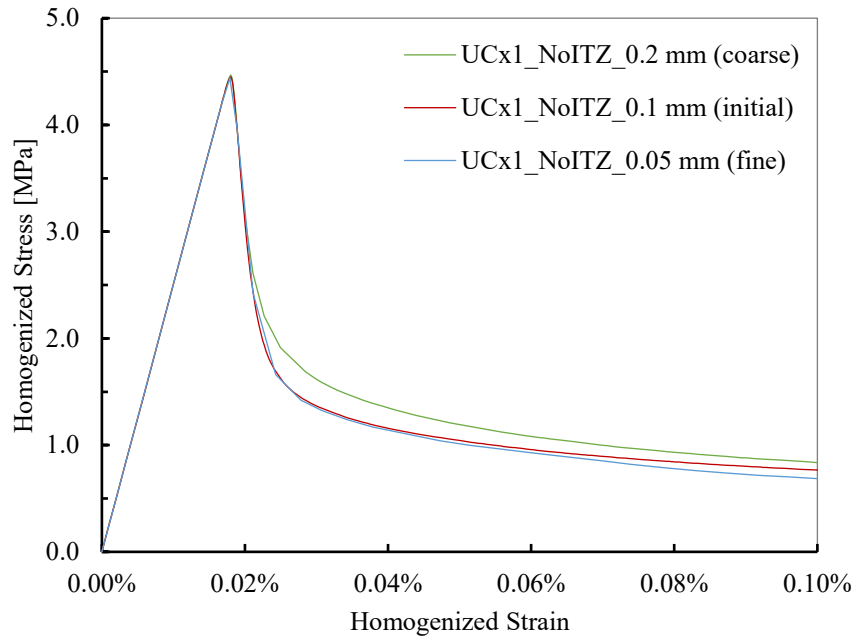


Figure 4.20 – Uniaxial tension test of single unit cell: reduced mesh sensitivity in local damage model

Non-local damage versus local damage

An algorithm for computation of the non-local damage was programmed in Octave as explained in section 3.3. The uniaxial tension test of the single unit cell without the ITZ is repeated in this section with the non-local formulation of the damage model. The main purpose is to demonstrate the performance of the developed program and to evaluate the result. The homogenized stress-strain diagram is also compared with the diagram that obtained earlier with the local formulation.

For the general static FEM analysis, the model is discretized by 4-node linear tetrahedral elements. The largest mesh size is 0.1 mm. The FEM mesh consists of 11 300 elements approximately. The applied strain is equal to 0.001. The interaction radius R is assumed to be 0.2 mm. The standard averaging technique is used to homogenize the stress-strain at every increment.

For a comparison with the local damage model, the single unit cell with the initial mesh size is chosen (Table 4.4). Therefore, the mesh size is identical in both simulations. Figure 4.21 illustrates the homogenized stress-strain diagram of the single unit cell with the non-local versus the local formulation of the damage.

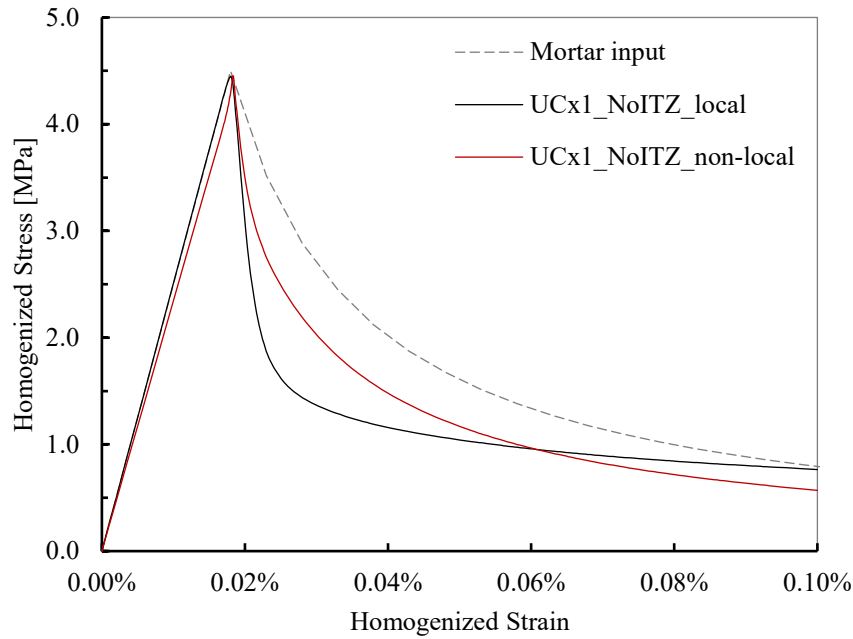


Figure 4.21 – Uniaxial tension test of single unit cell: local vs. non-local damage model

Figure 4.21 demonstrates that the homogenized diagram obtained from the model with the non-local formulation has a much better agreement with the mortar input curve. This can be justified by the weighted averaging scheme in the non-local formulation. On the one hand, the strain of any material point is constantly replaced with the average strain of the neighborhood (section 3.3). This prevents the localization of strain and results in a more uniform strain-distribution in the material domain. On the other hand, the input curve represents an ideal material with excessively uniform strain-distribution. Therefore, simulation with the non-local damage results in a curve that is comparable to the input curve.

Table 4.5 shows that the change in the mechanical properties is negligible when the formulation of the damage model is changed from local to non-local. Particularly, the fracture energy is expected to remain constant regardless of the damage formulation (definition of fracture energy in section 3.2). This can validate the developed algorithm for the non-local computation of the damage model.

Table 4.5 – Mechanical properties obtained from stress-strain diagram

Damage formulation	f_t [MPa]	ε_t [-]	E_0 [MPa]	g_f
Local	4.48	0.00018	25238	0.00145
Non-local	4.45	0.00018	24369	0.00142

4.3 Mesoscale cubic specimen under uniaxial tension

In this section, the simulation of the uniaxial tension test is extended to the mesoscale model of concrete. The main goal is to evaluate the outcome of the developed procedures when applied to a model with a more complicated structure than the unit cell. The cubic specimens of concrete are modeled in Abaqus that vary in the size and the volume fraction of aggregate. The configuration of the specimens is taken from (Gitman, Askes, & Sluys, 2007).

Two model sizes are considered. For each model size, specimens with three different volume fractions of aggregate are created. Therefore, there is a total of six specimens. As listed in Table 4.6, the chosen name for every specimen reflects the size of the cube and the volume fraction of aggregate. The prefix T stands for tension. The suffix A1 refers to the set of aggregate diameters used in the grading. However, only one set of diameters is used for all models in this study (Table 4.7).

Table 4.6 – Variation of the cubic specimens in the simulation

Cube	Aggregate Volume Fraction		
[mm]	30%	45%	60%
15 × 15 × 15	T15_30_A1	T15_45_A1	T15_60_A1
20 × 20 × 20	T20_30_A1	T20_45_A1	T20_60_A1

Generating a random distribution of particles

For generating a random distribution of the particles, the Aggregate Packing Generator (APG) developed by (Al-Rumaihi, 2019) is used. The APG uses take-and-place method based on the procedure published in (Unger & Eckardt, 2011). The Fuller grading curve as per Equation (2.4) is adopted for computing the volume ratio of particles. The take-and-place method and the main features of the Eckardt procedure were described in section 2.3.1.

For importing the generated particles into Abaqus, an input file must be scripted in Python. The scripted input file defines the structure of the generated particles by listing the coordinates of the centroid and the radius of all particles. Abaqus reads the script and generates the 3D model of the particles. For scripting in Python, the Mote3D toolbox developed by (Richter, 2017) is used. Mote3D can generate the required Python script for a given set of particles. Although Mote3D itself is capable of generating randomly distributed particles, only the output generator of the program is used in this study.

The APG and Mote3D are both downloadable¹ open source codes, and they were written in MATLAB and Octave, respectively. In this study, both codes are run by GNU Octave, version 4.2.0. They both run

¹ APG: <https://de.mathworks.com/matlabcentral/fileexchange/73188-aggregate-packing-generator>
Mote3D: https://github.com/Mote3D/Mote3D_toolbox

efficiently, and they can generate the model in almost no time. Some minor modifications are made in both codes before using them as follows:

For exporting the structure of the generated particles by the APG, additional lines are added to the executing code. The output files are two text files in the readable format for Mote3D. One file contains the coordinates of the centroid and the other holds the radius of the particles.

The particle generator is disabled in Mote3D. The particle radius, generated by the APG, is imported by the text file into Mote3D. Specific lines are also added for using the generated coordinates by the APG as an input.

In this study, the aggregate has a spherical shape with diameter from 2.5 mm to 5.0 mm (Table 4.7). The shape and size of the aggregate are taken from (Gitman, Askes, & Sluys, 2007). The generated particles by the APG is shown in Figure 4.22. The number of particles in each diameter class is listed in Table 4.8.

Table 4.7 – Aggregate set and diameters

Aggregate set	Diameter [mm]	
	Class 1	Class 2
A1	$2.5 \leq \phi < 3.5$	$3.5 \leq \phi < 5.0$

Table 4.8 – Generated particles for cubic specimens

Specimen	No. of Particles		
	Diameter [mm]		total
	$2.5 \leq \phi < 3.5$	$3.5 \leq \phi < 5.0$	
T15_30_A1	11 (73%)	4 (27%)	15
T15_45_A1	14 (74%)	5 (26%)	19
T15_60_A1	17 (71%)	7 (29%)	24
T20_30_A1	24 (71%)	10 (29%)	34
T20_45_A1	33 (70%)	14 (30%)	47
T20_60_A1	45 (73%)	17 (27%)	62

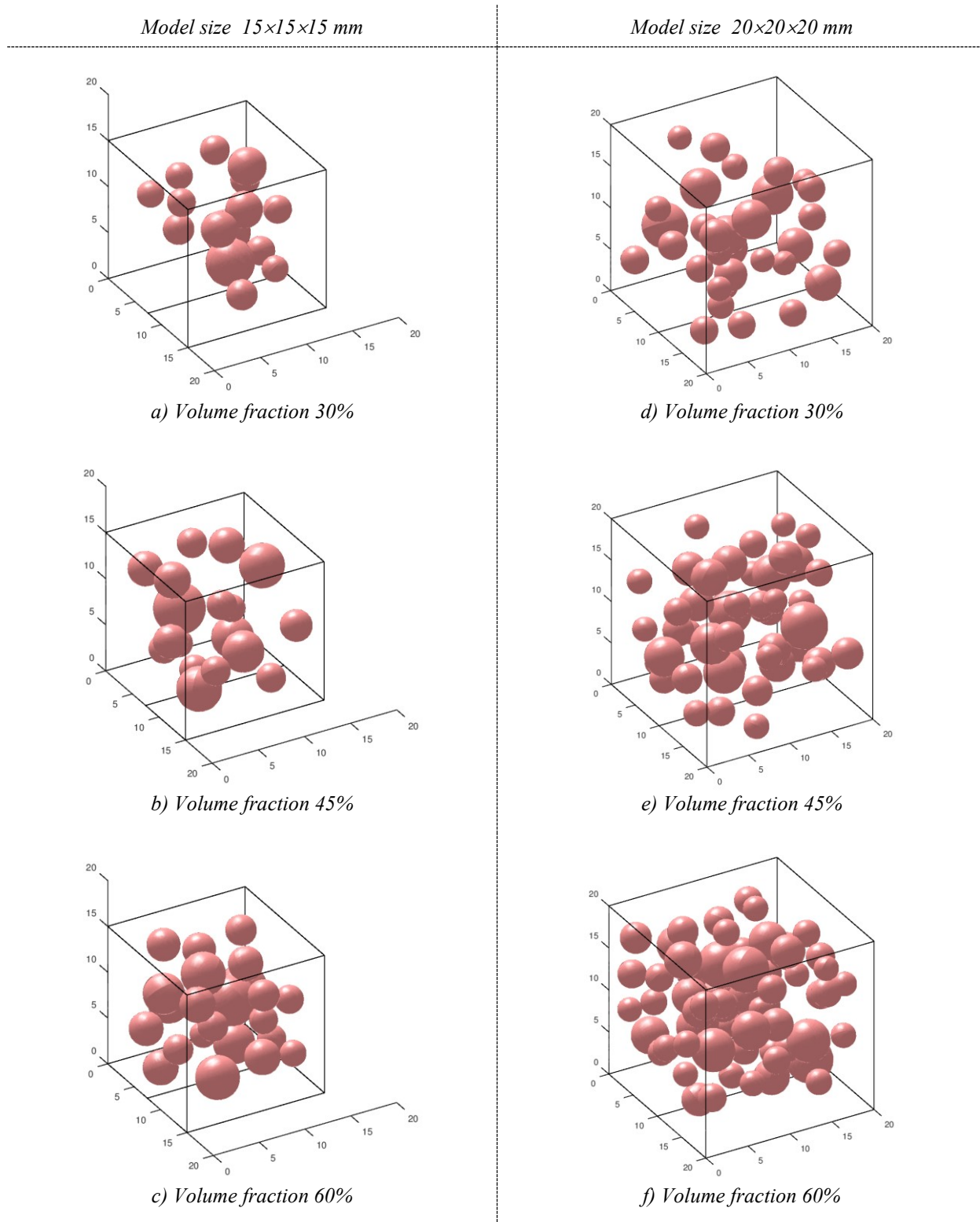


Figure 4.22 – Generated particles by APG

The mesoscale model

The mesoscale model of the concrete specimen in this study has three phases: aggregate, mortar matrix, and the ITZ. The linear elastic behavior is assumed for the aggregate. The local damage model with the Hillerborg energy approach is considered for the nonlinear behavior of the mortar matrix (section 3.2). The CCB with the strain-free adjustment is used for modeling the ITZ. The tensile behavior of ITZ is described

by the traction-separation law, and the damage evolution is energy-based (section 3.4). The material properties are presented in Table 4.2.

The models are discretized by 4-node linear tetrahedral elements. The largest mesh size is 1.0 mm. The number of elements in the FEM mesh is listed in Table 4.9. The applied strain is limited to 0.001 to reduce computation time. The standard averaging technique is used to homogenize the stress-strain relationship at every increment.

Table 4.9 – No. of elements in cubic specimen

Specimen	Max. mesh size [mm]	No. of elements	Analysis time* [min]
T15_30_A1	1.0	47 000	45
T15_45_A1		43 000	45
T15_60_A1		42 500	53
T20_30_A1		88 800	120
T20_45_A1		108 700	180
T20_60_A1		120 200	240

*CPU: Intel i7-7500U @ 3.5 GHz Dual core; RAM: 12 GB @ 1066 MHz

Assessment of the result

The stress-strain diagrams are grouped in Figure 4.23 according to the model size. The difference between the curves of the volume fractions 30% and 45% is negligible. The drop in the peak stress becomes notable only when the volume fraction is raised to 60%. Table 4.10 shows the mechanical properties of the specimens obtained from the homogenized stress-strain diagrams. The area under the curve is presented as the fracture energy. The result shows that the fracture energy increases as the volume fraction of aggregate becomes larger. This is in agreement with the conclusion in (Tasdemir & Karihaloo, 2001).

(Tasdemir & Karihaloo, 2001) provides a comprehensive study on the effect of the aggregate volume fraction on the mechanical properties of concrete. The simulations are performed with a series of mesoscale models. The volume fraction of aggregate varies from 0.0 to 0.60, while the other parameters, including the aggregate size, are kept constant. The article concludes that as the aggregate volume fraction increases, the fracture energy increases too.

The stress-strain diagrams are grouped in Figure 4.24 according to the volume fraction. Notably, the curves are sensitive to the size of the model. This is in contrast to the outcome of the simulations with the unit cell in Figure 4.7. Nevertheless, (Gitman, Askes, & Sluys, 2007) obtained a similar outcome: the peak stress almost always reduces as the size increases (Figure 4.25).

The damage-distribution diagram of all specimens at 0.1% strain is illustrated in Figure 4.26. The diagrams show the middle section of the specimens.

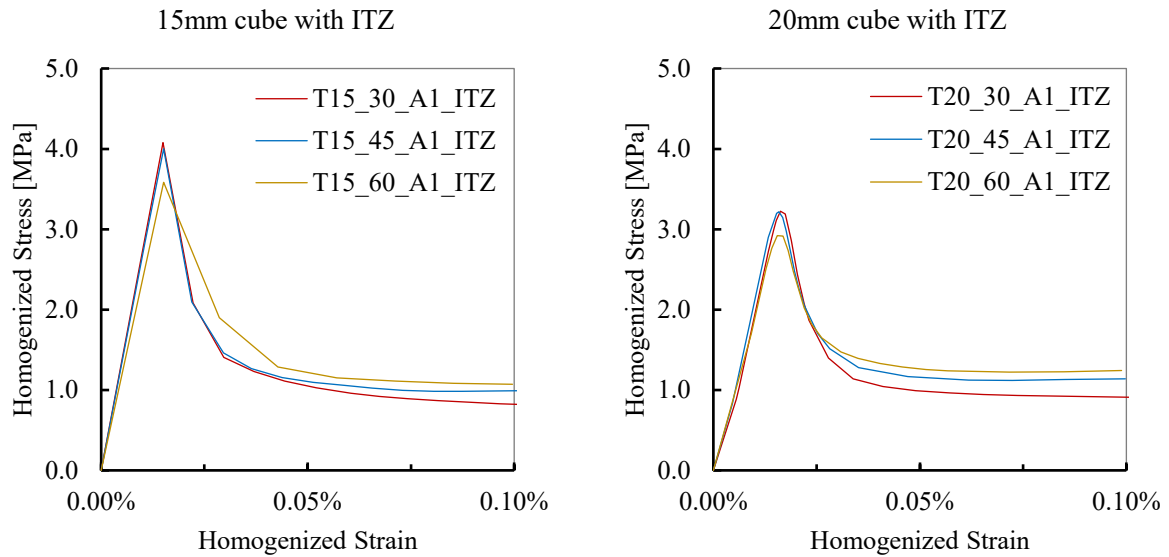


Figure 4.23 – Comparison between different volume fractions for every model size

Table 4.10 – Mechanical properties obtained from stress-strain diagram

Specimen	f_t [MPa]	ε_t [-]	E_0 [MPa]	g_f
T15_30_A1_ITZ	4.08	0.00015	27178	0.00139
T15_45_A1_ITZ	4.00	0.00015	26523	0.00143
T15_60_A1_ITZ	3.58	0.00015	23727	0.00151
T20_30_A1_ITZ	3.22	0.00016	19841	0.00125
T20_45_A1_ITZ	3.22	0.00016	20249	0.00137
T20_60_A1_ITZ	2.92	0.00015	18880	0.00140

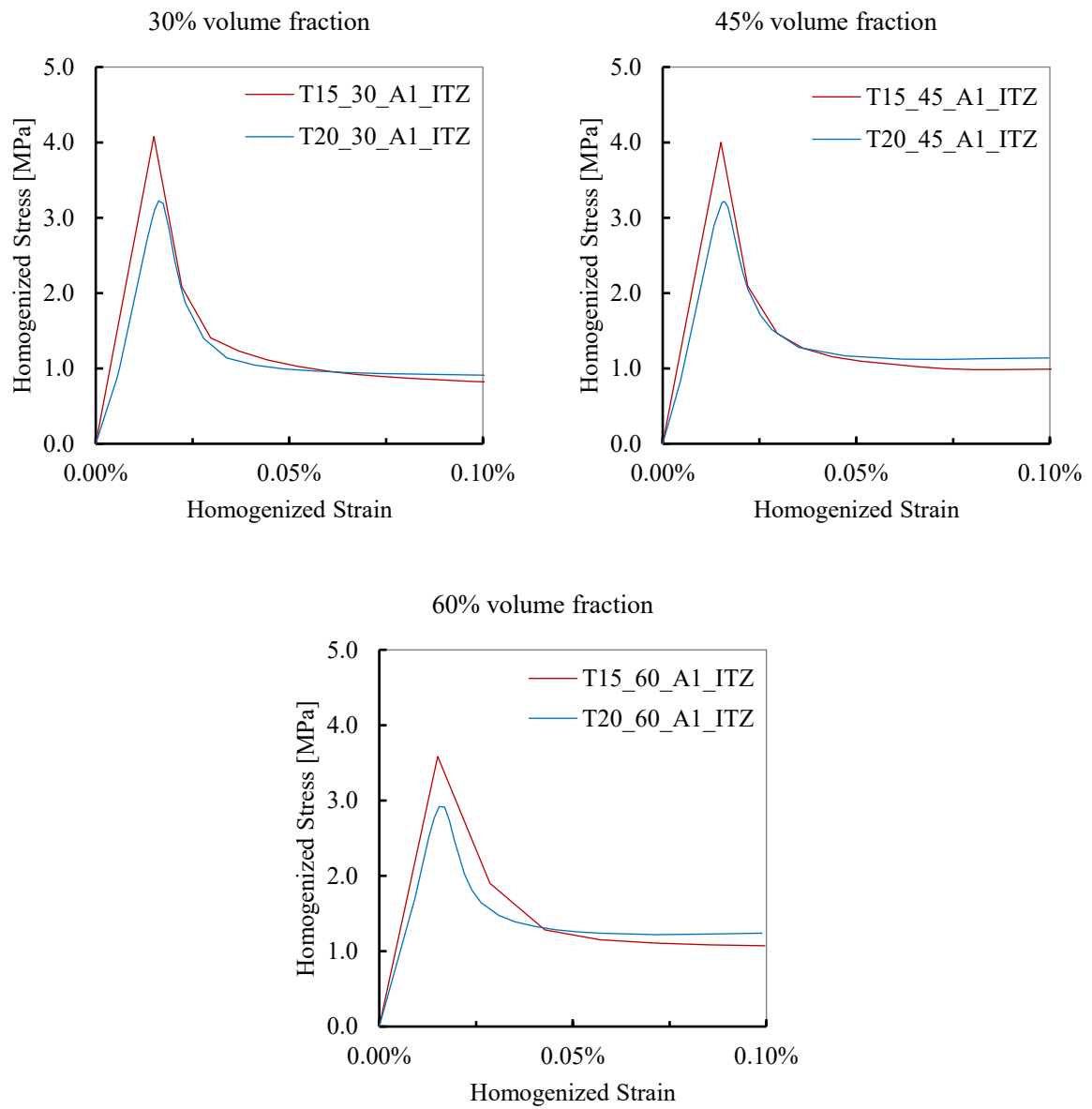


Figure 4.24 – Comparison between different model sizes for every volume fraction

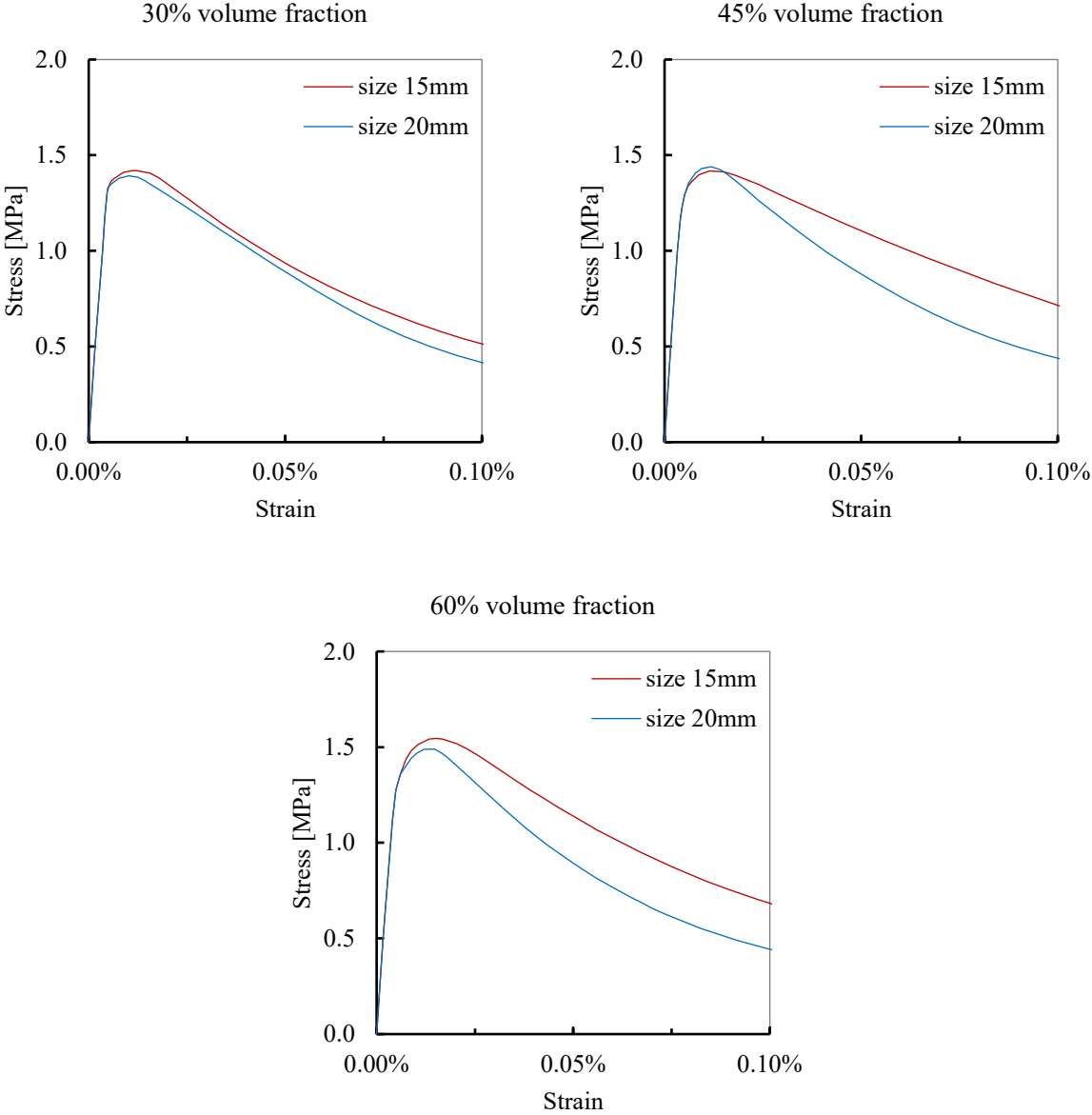


Figure 4.25 – Simulation outcomes in (Gitman, Askes, & Sluys, 2007)

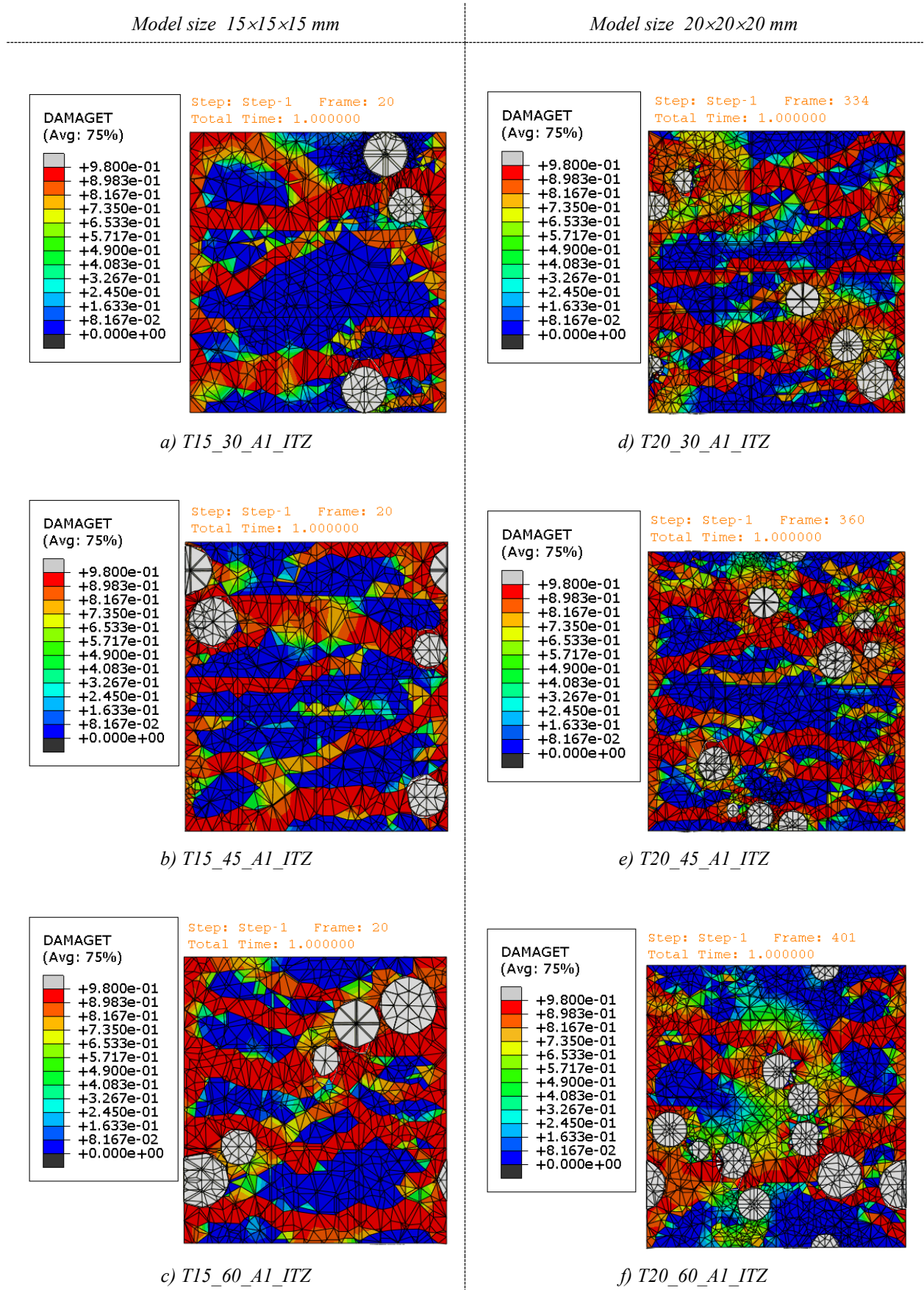


Figure 4.26 – Damage-distribution at 0.1% strain for every specimen (mid-section)

Investigation into the observed size sensitivity

To examine whether sensitivity to the size model is caused by the nonlinear ITZ, the simulation with the specimen is repeated without the ITZ. The two specimens with 30% volume fraction are chosen for this purpose. In the absence of ITZ, the bond between the particles and the mortar is considered to be completely rigid. The rest of the assumptions remain unchanged.

Figure 4.27 compares the homogenized stress-strain diagrams of the two model sizes. The curves are in good agreement. The simulation result clarifies that the observed size sensitivity is caused by the nonlinear ITZ.

The nonlinear ITZ did not exhibit sensitivity to the model size when used in the simulations with the unit cell in section 4.2. The main difference between the unit cell and the specimen is in the number of aggregate particles. Therefore, the nonlinear ITZ is sensitive to the number of aggregate particles. Further investigation is required to reveal an explanation for the observed sensitivity.

Improvement in the modeling techniques and the damage formulation for the ITZ should be the subject of future studies.

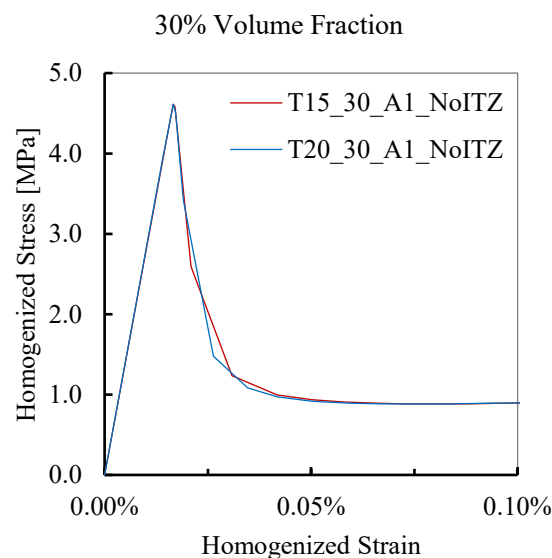


Figure 4.27 – Comparison between two model sizes without nonlinear ITZ

4.4 Mesoscale unit cell under cyclic tension

The behavior of concrete in tension under a cyclic load is described by the unloading-reloading path. (Yankelevsky, 1989) proposes a model for the complex behavior of concrete under cyclic load. The model is described by a series of focal points. The points are placed along the tangent line to the elastic branch of the stress-strain curve. The focal points are solely dependent on the tensile strength, and each of them is computed as a different proportion of the tensile strength. Figure 4.28 shows the simplified version of the model.

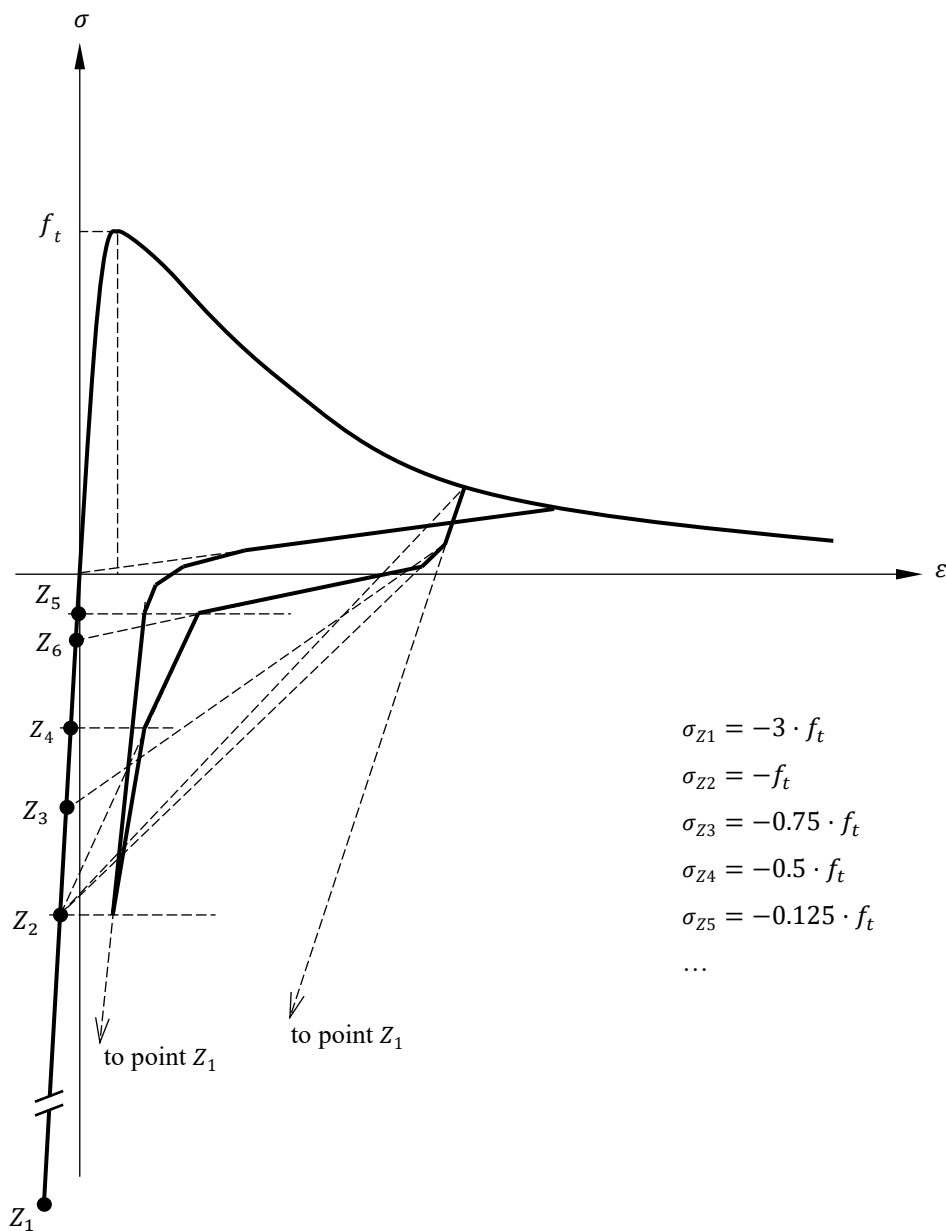


Figure 4.28 – Focal point model by (Yankelevsky, 1989)

Figure 3.5 shows the unloading path for a point on the softening branch, namely point 3. It was explained in section 3.2 that for any point on the softening branch, the slope of the unloading path is equal to the reduced Young's modulus. The reduced Young's modulus is a function of the damage parameter, and it is calculated by Equation (3.14). Therefore, the damage parameter computed by Equation (3.9) is the determining parameter for describing the unloading-reloading path in the present study.

The cyclic tension test of a single unit cell (Figure 4.3.a) is simulated in Abaqus. The test is displacement-driven. A uniaxial cyclic displacement is applied to the top surface of the unit cell. The “Boundary Condition” tool and the “Amplitude” function in Abaqus are used to define the applied strain (Figure 4.29). The cyclic displacement is defined in the Amplitude window in tabular form.

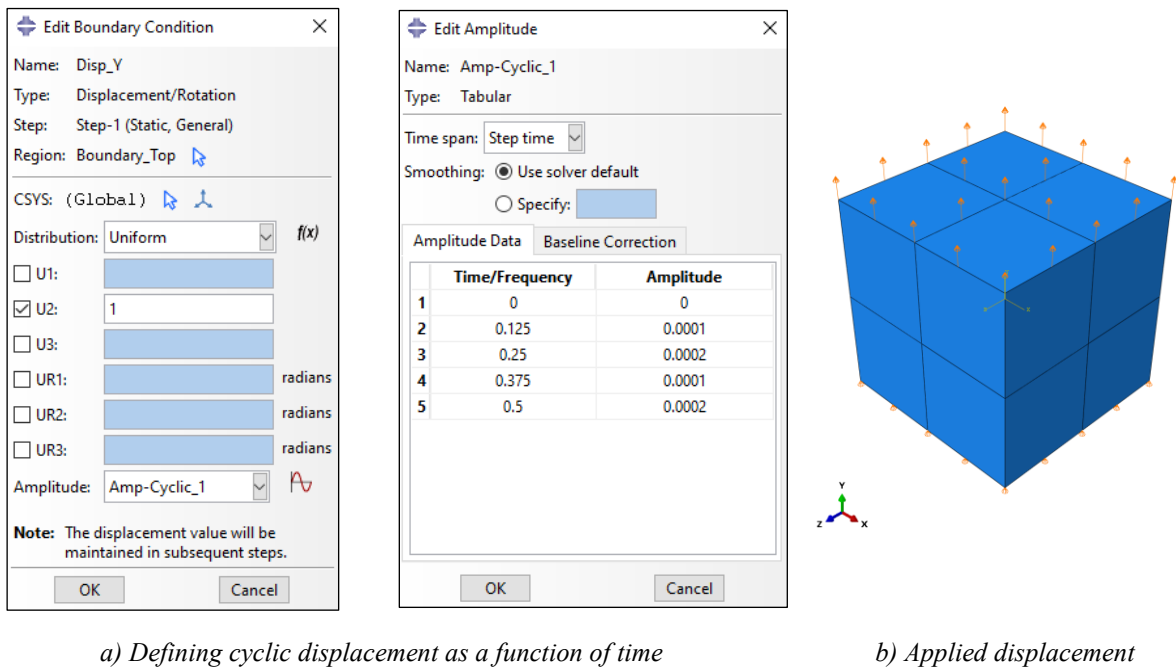


Figure 4.29 – Creating displacement-driven cyclic load in Abaqus Load module

The nonlinear ITZ is eliminated in the unit cell. In the absence of the ITZ, the bond between the particle and the mortar is considered to be completely rigid. The linear elastic behavior is assumed for the aggregate. The local damage model with the Hillerborg energy approach is considered for the nonlinear behavior of the mortar matrix (section 3.2). The model is discretized by 4-node linear tetrahedral elements. The largest mesh size is 0.1 mm.

In the first experiment, the load is a triangular impulse with an amplitude of 0.0002 mm (inducing 0.02% strain), and a period of 0.5 unit of time (Figure 4.30.a). The stress-strain diagram of one integration point in the mortar matrix is shown in Figure 4.30.b. The unloading curve crosses the zero-stress level as the load drops to zero. (Yankelevsky, 1989) explains that after reaching a certain level of negative stress, the

unloading curve in tension becomes a loading curve in compression. To avoid compressive stress in the unloading phase, Yankelevsky limits the lower bound level of stress to 5% of the tensile strength.

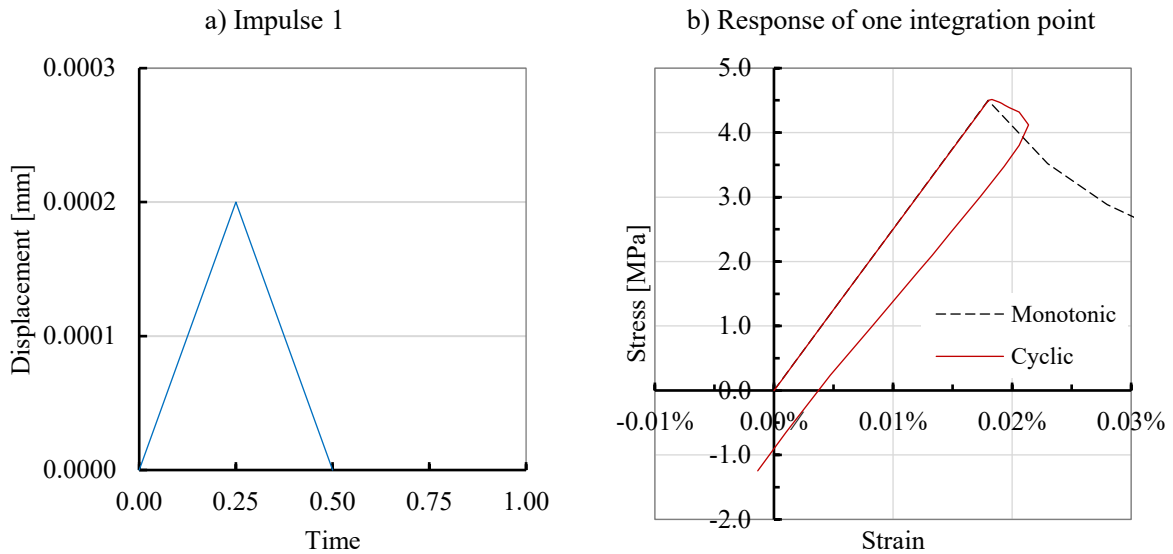


Figure 4.30 – First simulation of cyclic tension with a single unit cell without ITZ

Similar to the Yankelevsky experiment, the impulsive load is modified such that the unloading branch in the stress-strain curve does not cross the zero line. By try-and-error, the lower bound of 0.0001 mm (inducing 0.01% strain) is found. For re-loading the model, a half-impulse is added to the load (Figure 4.31.a). The response of the same integration point is provided in Figure 4.31.b. The stress-strain diagram shows that after 1.0 MPa increase in the stress level, the material point starts to unload at the stress level of 2.0 MPa. The response of the material in Figure 4.31.b is not in agreement with the behavior of concrete under cyclic load as described by Yankelevsky.

(Dere & Koroglu, 2017) used a rather unique periodic load to simulate the cyclic test of concrete in Abaqus. A similar load is generated as shown in Figure 4.32.a. The total duration of the load is 1 unit of time. Its maximum amplitude is just below 0.003 mm (inducing 0.3% strain). The analysis is run until 0.1% strain is achieved. The homogenized stress-strain diagram of the unit cell is presented in Figure 4.32.b. The standard averaging technique is used to obtain the homogenized stress-strain curve. The curve in Figure 4.32.b demonstrates that the simulation has captured the unloading-reloading behavior of the material. This is similar to the outcome of the experiment in (Dere & Koroglu, 2017).

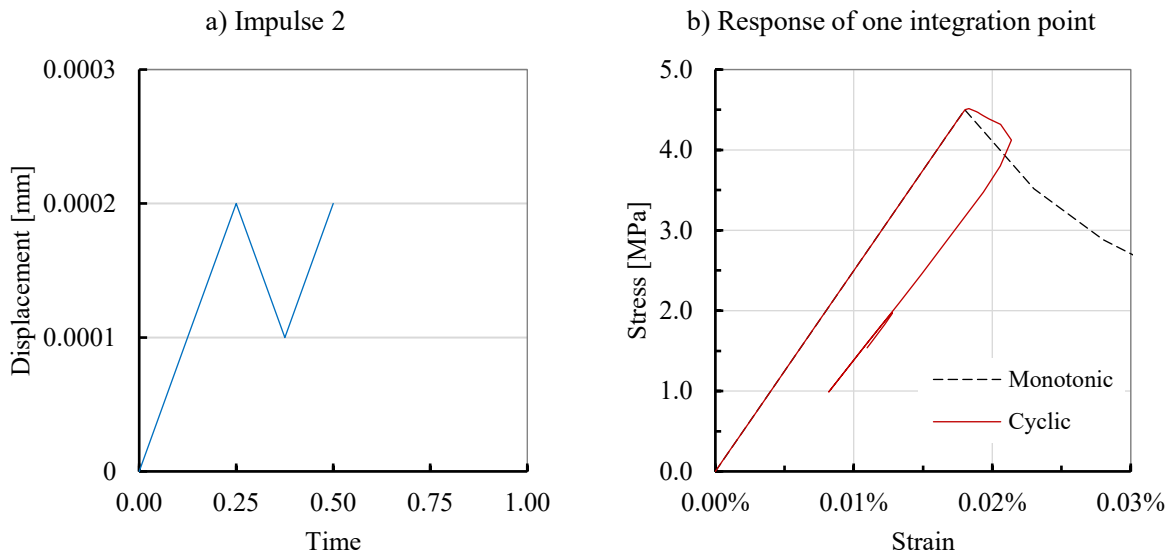


Figure 4.31 – Second simulation of cyclic tension with a single unit cell without ITZ

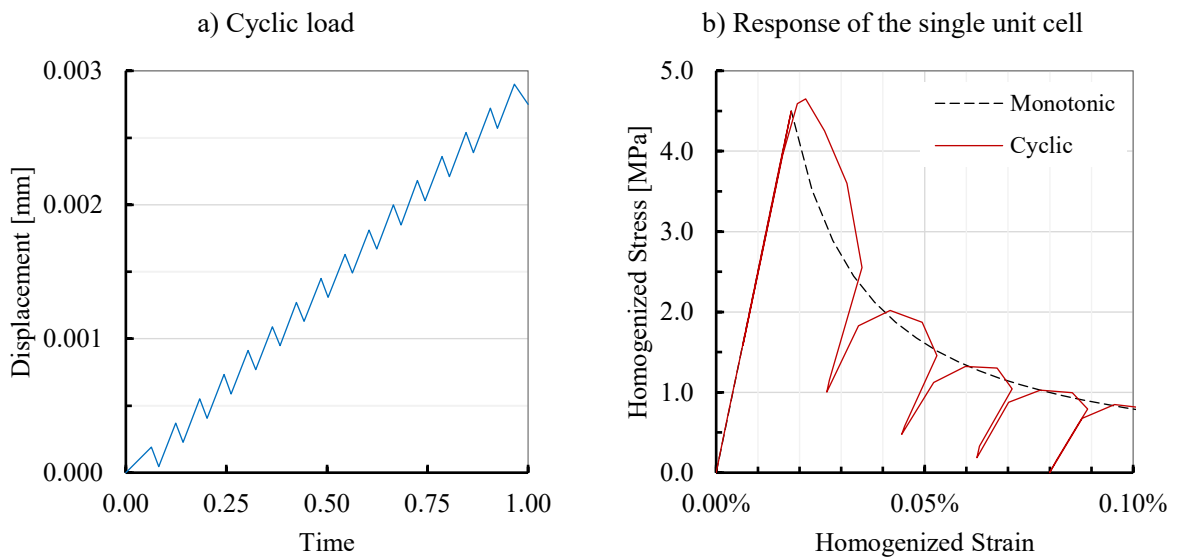


Figure 4.32 – Third simulation of cyclic tension with a single unit cell without ITZ

5 Conclusions

The overall focus of this thesis was on hierarchical multiscale models of composite materials in particular concrete. For this purpose, four main objectives were to be achieved.

As the initial step, a comprehensive literature review was conducted. The observation scales were explained and the common length scales in the literature were introduced. A comparison between these length scales for the number of inclusions and the RVE size were provided. The recent improvement in the particle generating methods was presented. The multiscale modeling of composite materials was introduced by exploring the classical categorization of the methods. Three recently developed multiscale models from the literature were introduced to demonstrate the application of multiscale modeling and its contribution to the composite design.

A generic model for concrete in tension was developed. A heterogeneous mesoscale model composed of aggregate, mortar matrix, and the ITZ was defined. The nonlinear ITZ was described with the traction-separation energy-based formulation and modeled with the contact cohesive behavior in Abaqus. The nonlinearity of the mortar was described by the isotropic damage model enhanced by the Hillerborg energy approach to minimize mesh sensitivity. The implementation of the model in Abaqus was explained. Non-local formulation of the damage model was programmed in Octave to be used alongside Abaqus. The classical homogenization scheme together with two recent modified versions of it were reviewed. An algorithm was programmed in Octave to compute the homogenized constitutive relationship according to the three schemes.

Numerical examples provided to demonstrate the application of the developed model. The qualitative study of the developed model with the help of the single unit cell was conducted. The model could exhibit the post-failure softening of concrete under uniaxial tension. The simulation was repeated with the combined unit cells to study the size effect. The result verified that the model was not sensitive to the size. Adding the nonlinear ITZ to the mesoscale model could demonstrate a reduction in the homogenized peak stress. In a comparative study, the standard averaging technique produced a more realistic result than two other modified schemes. Implementation of the Hillerborg energy approach in the local damage could reduce sensitivity to the mesh size considerably. The developed algorithm for the non-local damage performed successfully in the computation of the material response to the uniaxial tension. The non-local damage resulted in a stress-strain relationship with a smaller deviation from the input curve when compared to the local damage.

The extension of the developed model to a more complicated microstructure of concrete was demonstrated by modeling the mesoscale cubic specimens of concrete. The aggregate particles were successfully generated with the help of two open-source codes following the take-and-place method. However, the

simulation of the uniaxial tension test showed the sensitivity of the result to the model size. Investigation revealed that the size sensitivity was caused by the nonlinear ITZ. This is not in line with the simulation output of the unit cell with the nonlinear ITZ. Further study is required to be conducted to resolve the issue.

Simulation of the cyclic tension tests of the unit cell was carried out. The obtained unloading-reloading path in the simulation with an impulsive load failed to resemble the cyclic behavior of concrete found in the literature. However, the simulation with the periodic cyclic load could demonstrate the cyclic response of the material. The failure of the simulation with the impulsive load should be investigated in future studies.

In summary, it can be concluded that the multi-phase representation of concrete heterogeneity by the developed mesoscale model and the implementation of the both local and non-local damage in Abaqus allow for a realistic simulation of the post-failure behavior of concrete in uniaxial tension.

References

Abaqus documentation. (2020). SIMULIA.

Al-Rumaithi, A. (2019, November). *File Exchange*. Retrieved from MathWorks: <https://de.mathworks.com/matlabcentral/fileexchange/73188-aggregate-packing-generator>

Babuska, I. (1973). The finite element method with Lagrangian multipliers. *Numerische Mathematik*, 20, 179-192.

Bazant, Z. P., Tabbara, M. R., Kazemi, M. T., & Cabot, G. R. (1990). Random Particle Model for Fracture of Aggregate or Fiber Composites. *Engineering Mechanics*.

Bazant, Z., & Oh, B. (1983). Crack band theory for fracture of concrete. *Materials and Structures*, 16, 155-177.

Bazant, Z., & Pijaudier-Cabot, G. (1987). Non-local damage theory. *Journal of Engineering Mechanics*, 113(10), 1512-1533.

Bellis, M. (2019, March 6). *ThoughtCo*. Retrieved from The History of Concrete and Cement: <https://www.thoughtco.com/history-of-concrete-and-cement-1991653>

Belytschko, T., & Song, J. (2010). Coarse-graining of multiscale crack propagation. *International Journal for Numerical Methods in Engineering*, 81, 537-563.

Belytschko, T., Loehnert, S., & Son, J. (2008). Multiscale aggregating discontinuities: A method for circumventing loss of material stability. *International Journal for Numerical Methods in Engineering*, 73, 869-894.

Benzeggagh, M. L., & Kenane, M. (1996). Measurement of mixed-mode delamination fracture toughness of unidirectional glass-epoxy composites with mixed-mode bending apparatus. *Composite Science and Technology*, 56, 439-449.

Bernard, O., Ulm, F.-J., & Lemarchand, E. (2004). A multiscale micromechanics-hydration model for the early-age elastic properties of cement-based materials. *Cement and Concrete Research*, 33, 1293-1309.

Bishnoi, S., & Scrivener, K. (2009). μ ic: A new platform for modelling the hydration of cements. *Cement and Concrete Research*, 39, 266-274.

Caballero, A., López, C., & Carol, I. (2006). 3D meso-structural analysis of concrete specimens under uniaxial tension. *Computer Methods in Applied Mechanics and Engineering*, 195, 7182-7195.

- Camanho, P. P., & Dávila, C. G. (2002). *Mixed-mode decohesion finite elements for the simulation of delamination in composite material*. NASA.
- Constantinides, G., & Ulm, F.-J. (2004). The effect of two types of C-S-H on the elasticity of cement-based materials: Results from nanoindentation and micromechanical modeling. *Cement and Concrete Research*, *34*, 67-80.
- Contrafatto, L., Cuomo, M., & Gazzo, S. (2016). A concrete homogenisation technique at meso-scale level accounting for damaging behaviour of cement paste and aggregates. *Computers & Structures*, *173*, 1-18.
- Cundall, P. (1971). A computer model for simulating progressive large scale movements in blocky rock systems. *Proc. Symp. Int. Soc. Rock Mech, Nancy*.
- Cusatis, G., Bazant, Z. P., & Cedolin, L. (2006). Confinement-shear lattice CSL model for fracture propagation in concrete. *Computer Methods in Applied Mechanics and Engineering*, *195*, 7154–7171.
- de Boer, A., van Zuijlen, A., & Bijl, H. (2007). Review of coupling methods for non-matching meshes. *Computer Methods in Applied Mechanics and Engineering*, *196*(8), 1515-1525.
- Dere, Y., & Koroglu, M. (2017). Nonlinear FE modeling of reinforced concrete. *International Journal of Structural and Civil Engineering Research*, *6*(1), 71-74.
- Drugan, W., & Willis, J. (1996). A micromechanics-based nonlocal constitutive equation and estimates of representative volume element size for elastic composites. *Journal of the Mechanics and Physics of Solids*, *44*(4), 497-524.
- Eckardt, S. (2009). Adaptive heterogeneous multiscale models for the nonlinear simulation of concrete. *PhD Dissertation*. Germany: Bauhaus-Universität Weimar.
- Emery, V. L. (2009). Mud-Brick. *UCLA Encyclopedia of Egyptology*.
- Evesque, P. (2000). Fluctuations, Correlation and Representative Elementary Volume (REV) in Granular Materials. *Poudres & Grains*, *11*, 6-17.
- Feyel, F. (2003). A multilevel finite element method (FE²) to describe the response of highly non-linear structures using generalized continua. *Computer Methods in Applied Mechanics and Engineering*, *192*(28-30), 3233-3244.
- Gitman, I., Askes, H., & Sluys, L. (2007). Representative volume: Existence and size determination. *Engineering Fracture Mechanics*, *74*, 2518-2534.

- Göbel, L. (2018). Experimental and semi-analytical multiscale approaches for the characterization of the elastic and viscoelastic behavior of polymer-modified cement-based materials. *PhD Dissertation*. Germany: Bauhaus-Universität Weimar.
- Grassl, P., & Jirásek, M. (2010). Meso-scale approach to modelling the fracture process zone of concrete subjected to uniaxial tension. *International Journal of Solids and Structures*, 47, 957–968.
- Guo, L., Carpinteri, A., Roncella, R., Spagnoli, A., Sun, W., & Vantadori, S. (2009). Fatigue damage of high performance concrete through a 2D mesoscopic lattice model. *Computational Materials Science*, 44(4), 1098-1106.
- Häfner, S. (2007). Grid-based procedures for the mechanical analysis of heterogeneous solids. *PhD Dissertation*. Germany: Bauhaus-Universität Weimar.
- Häfner, S., Eckardt, S., Luther, T., & Könke, C. (2006). Mesoscale modeling of concrete: Geometry and numerics. *Computers and Structures*, 84, 450-461.
- Hain, M., & Wriggers, P. (2008). Numerical homogenization of hardened cement paste. *Computational Mechanics*, 42, 197-212.
- Hashin, Z. (1983). Analysis of Composite Materials - A Survey. *Journal of Applied Mechanics*, 50, 481-505.
- Herring, B. (2002, September). The secrets of roman concrete. *Constructor*.
- Hill, R. (1963). Elastic properties of reinforced solids: Some theoretical principles. *Journal of the Mechanics and Physics of Solids*, 11(5), 357-372.
- Hillerborg, A., Modéer, M., & Peterson, P.-E. (1976). Analysis of crack formation and crack growth in concrete by means of fracture mechanics and finite elements. *Cement and Concrete Research*, 6, 773-782.
- Hirai, I., Wang, B., & Pilkey, W. (1984). An Efficient Zooming Method for Finite Element Analysis. *International Journal for Numerical Methods in Engineering*, 20, 1671-1683.
- Huang, Y., Yang, Z., Ren, W., Liu, G., & Zhang, C. (2015). 3D meso-scale fracture modelling and validation of concrete based on in-situ X-ray Computed Tomography images using damage plasticity model. *International Journal of Solids and Structures*, 340-352.
- Jankowiak, T., & Lodygowski, T. (2005). Identification of parameters of concrete damage plasticity constitutive model. *Foundation of Civil and Environmental Engineering*, 6, 53-69.
- Jirásek, M. (2004). Non-local damage mechanics with applicaiton to concrete. *Failure, Degradation and Instabilities*, 683-707.

- Jirásek, M., & Zimmermann, T. (1998). Analysis of rotating crack model. *Journal of Engineering Mechanics*, 124(8), 842-851.
- Kachanov, L. (1986). *Introduction to continuum damage mechanics*. Netherlands: Martinus Nijhoff Publishers.
- Kaplan, M. (1961). Crack Propagation and the Fracture of Concrete. *International Concrete Abstracts Portal*, 58(11), 591-610.
- Kim, S.-M., & Abu Al-Rub, R. K. (2011). Meso-scale computational modeling of the plastic-damage response of cementitious composites. *Cement and Concrete Research*, 41, 339-358.
- Leite, J., Slowik, V., & Mihashi, H. (2004). Computer simulation of fracture processes of concrete using mesolevel models of lattice structures. *Cement and Concrete Research*, 34, 1025-1033.
- López, C. M., Carol, I., & Aguado, A. (2008). Meso-structural study of concrete fracture using interface elements. I: numerical model and tensile behavior. *Materials and Structures*, 583-599.
- Mercer, B., Mandadapu, K., & Papadopoulos, P. (2015). Novel Formulations of Microscopic Boundary-Value Problems in Continuous Multiscale Finite Element Methods. *Computer Methods in Applied Mechanics and Engineering*, 286, 286-292.
- Michel, J., Moulinec, H., & Suquet, P. (1999). Effective properties of composite materials with periodic microstructure: a computational approach. *Computer methods in applied mechanics and engineering*, 172, 109-143.
- Nguyen, V. P., Stroeven, M., & Sluys, L. J. (2012). Multiscale failure modelling of concrete: micromechanical modelling, discontinuous homogenization and parallel computations. *Computer Methods in Applied Mechanics and Engineering*, 201-204, 139-156.
- Nguyen, V. P., Valls, O. L., Stroeven, M., & Sluys, L. J. (2010). On the existence of representative volumes for softening quasi-brittle materials - a failure zone averaging scheme. *Computer Methods in Applied Mechanics and Engineering*, 199(45-48), 3028-3038.
- Nguyen, V. P., Valls, O. L., Stroeven, M., & Sluys, L. J. (2011). Homogenization-based multiscale crack modelling: from micro diffusive damage to macro cracks. *Computer Methods in Applied mechanics and Engineering*, 200(9-12), 1220-1236.
- Ostoj-Starzewski, M. (2002). Microstructural Randomness Versus Representative Volume Element in Thermomechanics. *Journal of Applied Mechanics*, 69(1), 25-35.
- Patowary, K. (2019, 6). *François Coignet's Reinforced Concrete House*. Retrieved from AmayingPlanet: <https://www.amusingplanet.com/2019/06/francois-coignets-reinforced-concrete.html>

- Richter, H. (2017). Mote3D: an open-source toolbox for modelling periodic random particulate microstructures. *Modelling and Simulation in Materials Science and Engineering*, 25(3).
- Roylance, D. (2001a). Fatigue. Department of Materials Science and Engineering, Massachusetts Institute of Technology, Cambridge.
- Roylance, D. (2001b). Introduction to fracture mechanics. Department of Materials Science and Engineering, Massachusetts Institute of Technology, Cambridge.
- Ruan, X., Li, Y., Jin, Z., Pan, Z., & Yin, Z. (2019). Modeling method of concrete material at mesoscale with refined aggregate shapes based on image recognition. *Construction and Building Materials*, 204, 562-575.
- Sanahuja, J., Dormieux, L., & Chanvillard, G. (2007). Modelling elasticity of a hydrating cement paste. *Cement and Concrete Research*, 37, 1427-1439.
- Schutter, G. D., & Taerwe, L. (1993). Random particle model for concrete based on Delaunay triangulation. *Materials and Structures*, 26, 67-63.
- Sluys, L. (1992). Wave Propagation, Localisation and Dispersion in Softening Solids. *PhD Dissertation*. The Netherlands: Delft University of Technology.
- Sun, X., Guo, X., Guo, L., Wu, B., & Wang, Y. (2020). Multiscale Analysis of Concrete Damage and Crack Propagation Under High Cycle Loading. *International Journal of Computational Methods*, 17(01), 1844007.
- Tasdemir, M., & Karihaloo, B. (2001). Effect of type and volume fraction of aggregate on the fracture properties of concrete. *Fracture Mechanics of Concrete Structures*, 123-129.
- Unger, J. F., & Eckardt, S. (2011). Multiscale modeling of concrete. *Computational Methods in Engineering*, 18, 341-393.
- Van Mier, J., & Van Vliet, M. (2003). Influence of microstructure of concrete on size/scale effects in tensile fracture. *Engineering Fracture Mechanics*, 70, 2281-2306.
- Verhoosel, C., Remmers, J., M.A., G., & de Borst, R. (2010). Computational homogenization for adhesive and cohesive failure in quasi-brittle solids. *International Journal for Numerical Methods in Engineering*, 83, 1155-1179.
- Wang, J., Jivkov, A., Engelberg, D., & Li, Q. (2018). Meso-scale modelling of mechanical behaviour and damage evolution in normal strength concrete. *Procedia Structural Integrity*, 13, 560-565.
- Wang, W., Wang, J., & Kim, M. S. (2001). An algebraic condition for the separation of two ellipsoids. *Computer Aided Geometric Design*, 18, 531-539.

- Wang, X., Zhang, M., & Jivkov, A. (2016). Computational technology for analysis of 3D meso-structure effects on damage and failure of concrete. *International Journal of Solids and Structures*, 80, 310-333.
- Wriggers, P., & Moftah, S. (2006). Mesoscale models for concrete: Homogenisation and damage behaviour. *Finite Elements in Analysis and Design*, 42, 623-636.
- Yankelevsky, D. (1989). Uniaxial behavior of concrete in cyclic tension. *Journal of Structural Engineering*.
- Zaitsev, Y. B., & Wittman, F. H. (1981). Simulation of crack propagation and failure of concrete. *Materials and Structures*, 14, 357-365.
- Zhang, M. (2013). Multiscale Lattice Boltzmann-Finite Element Modelling of Transport Properties in Cement-based Materials. *PhD Dissertation*. The Netherlands: Delft University of Technology.